

Architectures of DNA block copolymers

DISSERTATION

zur Erlangung des Grades

"Doktor der Naturwissenschaften"

am Fachbereich Chemie, Pharmazie und Geowissenschaften
der Johannes Gutenberg-Universität Mainz

vorgelegt von

Master-Chem. **Ke Ding**

geb. in 03.01.1978

aus Jiangxi (V. R. China)

Mainz, 2006

Tag der mündlichen Prüfung: 14. 11. 2006

ABSTRACT

The aim of this work is to understand the surface morphology of amphiphilic deoxyribonucleic acid (DNA) block copolymers, which is an interesting topic in DNA nanotechnology. The specific base pairing in DNA sequences makes DNA programmable, which enables the transition from 1- dimensional structure to 2- or 3- dimensional structures of DNA block copolymers. The atomic force microscopy (AFM) has been applied for investigating the different architectures formed on different substrates in liquid and/or in air.

In-situ AFM studies illustrated that both DNA-*b*-polypropylene oxide (PPO) and DNA-*b*-polystyrene (PS) exhibit as single molecules or dimers of them below the critical micelle concentration (CMC) and globular micelles above the CMC. The micelles of DNA-*b*-PPO are flattened on mica surface with a height of 4-6 nm by AFM measurements due to the adsorption of the DNA with mica through the positive ions in buffer solutions, which was proved by dynamic light scattering (DLS) and fluorescence correlation spectroscopy (FCS) to have a diameter around 11 nm in solution.

In-situ experiments in liquid have been extended to study the micelles on different substrate, the micelles in higher salt concentration, the micelles with chemical modification around the shell, and the micelles hybridized with short and long complementary sequenced templates. On hydrophobic highly oriented pyrolytic graphite (HOPG) surface, height of DNA-*b*-PPO micelles increased to 11 nm by AFM due to a sublayer formation which serves as a substrate for subsequently settled micelles. Increasing the salt concentration in buffer led to a significant decrease of the micelle diameter on mica by AFM study as well as by diffusion NMR experiments. Chemical modification on the surface of the micelles in solution did not change the shape and size of the micelles. In order to achieve the transition from globular micelles to rod like structure, DNA-*b*-PPOs were hybridized with longer ss-template. The length of the rod like structure is able to be controlled by modifying the base sequences

in the repeating DNA-*b*-PPOs as well as in the template. The rods tend to form pairs of them due to the hydrophobic interaction between the PPO blocks. In addition, the flexibility of the template and the PPOs in the repeat units were changed by modifying base sequences in both DNA template and DNA block copolymers. Less possibility to form pairs of rods owing to the spatial hindrance was illustrated by adjusting the position of the polymers.

AFM studies in air were done on drop casted films as well as gold-templated matrix. Globular micelles were observed on drop casted DNA-*b*-PPO and DNA-*b*-PS films. In addition, cylindrical micelles have been detected as fibers on both DNA-*b*-PPO and DNA-*b*-PS films. The fibers were influenced by temperature, incubation time, humidity, and so on. Adding the DNA block copolymer as target onto the gold-templated matrix layer by layer has been investigated by AFM and surface plasmon resonance spectroscopy (SPR) with consistent and reproducible results.

INDEX

ABSTRACT	1
INDEX	3
MOTIVATION	4
1 METHODS	15
1.1 ATOMIC FORCE MICROSCOPY	15
1.1.1 Instrumentation	15
1.1.2 Imaging modes	17
1.1.3 Imaging in liquid	19
1.1.4 Image interpretation	21
1.1.5 Sample preparation	22
1.2 LIGHT SCATTERING	25
1.2.1 Sample Preparation	27
1.3 FLUORESCENCE CORRELATION SPECTROSCOPY	27
1.3.1 Sample preparation	29
1.4 SURFACE PLASMON RESONANCE SPECTROSCOPY	31
1.4.1 Sample preparation	36
2 SYNTHESIS OF DNA BLOCK COPOLYMERS	37
2.1 DNA- <i>b</i> -PPO	37
2.2 DNA- <i>b</i> -PS	38
3 RESULTS AND DISCUSSIONS	40
3.1 IN-SITU AFM STUDIES IN SOLUTION	40
3.1.1 The critical micelle concentration	40
3.1.2 Below the critical micelle concentration	41
3.1.3 Above the critical micelle concentration	45
3.1.4 <i>ss</i> -DNA- <i>b</i> -PS	59
3.1.5 Long templated molecules	60
3.1.6 Concentration	75
3.1.7 Equilibrium time	77
3.1.8 Sublayer	78
3.1.9 Phase contrast	79
3.1.10 Summary of the dimensions of structures by AFM	81
3.2 AFM STUDIES IN AIR ON DROP CASTED FILMS	82
3.2.1 Micelles	82
3.2.2 Dendritic structures	84
3.2.3 Diffusion limited aggregation	86
3.2.4 Structural growth	87
3.2.5 Environmental parameters	88
3.2.6 Fibers formed with <i>ss</i> -DNA- <i>b</i> -PPO	90
3.3 AFM STUDIES IN AIR ON AU-TEMPLATED FILMS	91
SUMMARY AND CONCLUSIONS	95
BIBLIOGRAPHY	98
LIST OF PULICATIONS	101
ACKNOWLEDGEMENTS	ERROR! BOOKMARK NOT DEFINED.
ABBREVIATIONS	102

MOTIVATION

DNA (deoxyribonucleic acid) is a molecule that contains the genetic information for life. It has the ability to associate with and recognize other DNA molecules by means of specific base pairing relationships (Figure 0.1): an adenine (A) on one strand will pair preferentially with a thymine (T) on the other strand; likewise, guanine (G) will pair with cytosine (C). This complementary relationship has been known for about 45 years as the chemical basis for heredity ¹.

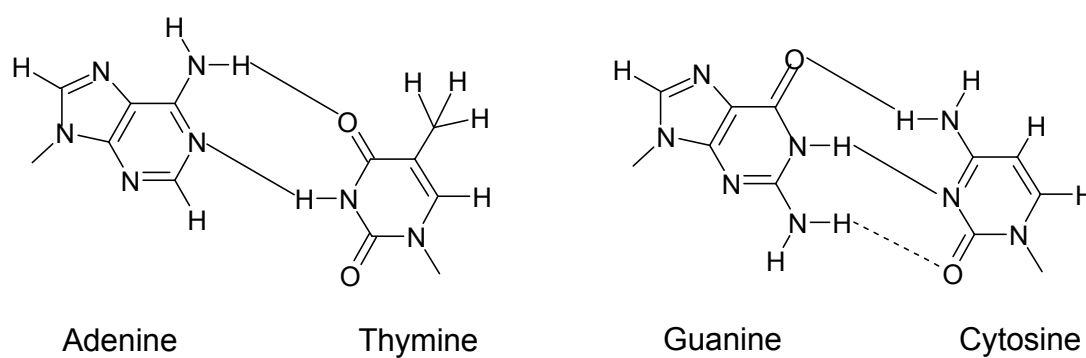


Figure 0.1. Structures of adenine (A), thymine (T), guanine (G), and cytosine (C) that are the four bases within DNA double helix. A forms 2 hydrogen bonds with T and G forms 3 hydrogen bonds with C.

DNA molecules can be ss-DNA or ds-DNA (Figure 0.2). Each strand of DNA is made of a sugar phosphate backbone plus sequences of four bases (A, T, G, and C) (Figure 0.3). Each DNA strand terminates in one end with a phosphate group (called the 5' end because of the position of phosphate group on the 5' carbon of the sugar ring) and the other end with a sugar molecule whose 3' carbon has a hydroxyl group (called the 3' end). DNA strands are able to be modified at both the 5' and 3' ends by conjugating the chemicals such as amine or thiol groups, biotin, fluorescent dyes, etc. onto the ends.

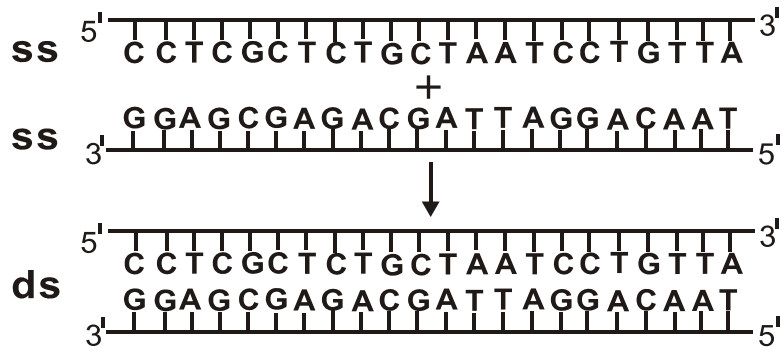


Figure 0.2. A double stranded (ds) DNA is formed through hybridization of two single stranded (ss) DNA that have complementary base sequences.

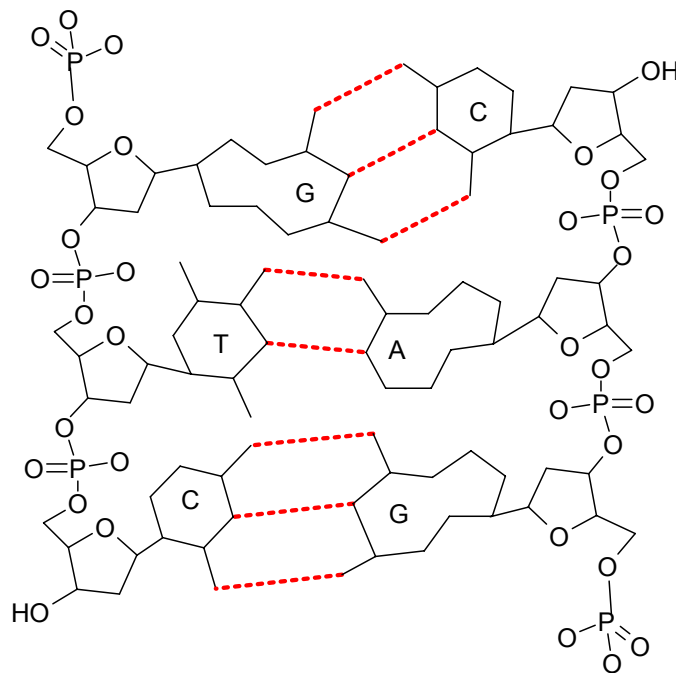


Figure 0.3. Part of ds-DNA molecule consisting of sugar phosphate backbone and pairs of bases.

The persistence length is approximate 50 nm for ds-DNA and a few nanometers for ss-DNA in water. The width of the double helix is about 2 nm and each base pair has a length of 0.34 nm^2 (Figure 0.4). Chemically, DNA is nontoxic, stable, and water soluble. The most common technique to obtain DNA is PCR (polymerase chain reaction).

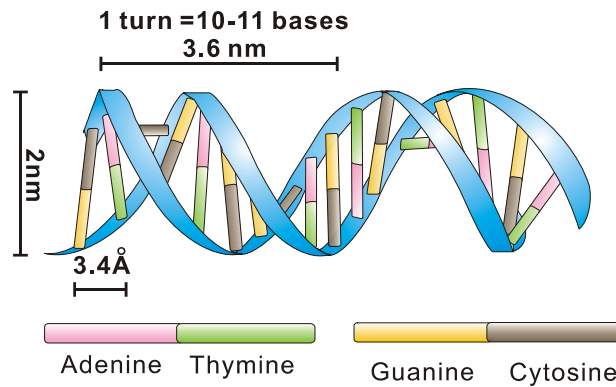


Figure 0.4. ds-DNA helix consisting of two helices of ss-DNA (blue) made of sugar phosphate backbone and pairs of bases adenine (A), guanine (G), cytosine (C), and thymine (T).

DNA Nanotechnology is about making, measuring, and manipulating DNA molecules that are in nanometer scale. N. C. Seeman founded the field of DNA nanotechnology in 1982. This field has been developed rapidly after the structure of DNA was determined in 1953 by Watson and Crick ¹. The specific base pairing in DNA sequences makes DNA programmable. This property is useful in novel materials design and construction ²⁻⁵. Using DNA to construct 2-dimensional and 3-dimensional nanostructures ⁶⁻⁸ has strongly increased over the last several years. DNA has been employed as the skeleton of these nanostructures and has served as an interconnect or template to form DNA-hybrid-nanostructures with other materials ⁹⁻¹². DNA has led to applications from new nucleic acid detection strategies ¹³ to nanoelectronic and nanomechanical structures and devices ^{12,14,15}.

Seeman, Mao, and their coworkers are the pioneers for DNA nanotechnology. A variety of geometric objects and periodic frameworks have been constructed successfully ^{6-8,16}. Figure 0.5 shows one example of their latest result on self-assembly of DNA nanotubes from one ss-DNA. They used two identical, 52-nucleotide long strands consisting of four segments: 10, 16, 16, and 10 bases long, respectively. Each segment is self-complementary and two strands will associate with each other to form a 2-dimensional complex at native condition. Further association with each other will result in two-dimensional sheets that eventually fold into nanotubes.

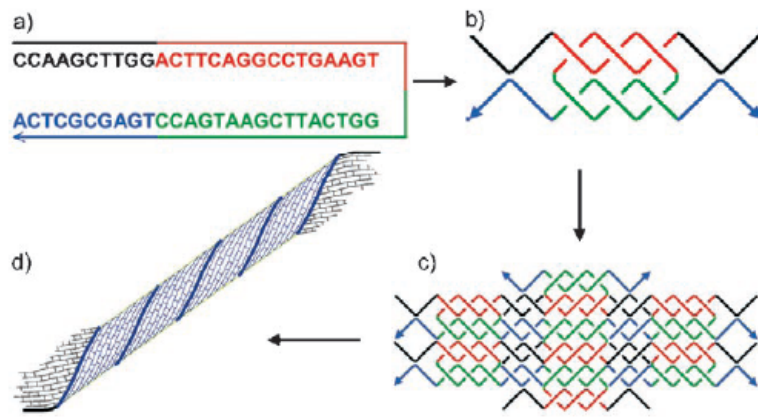


Figure 0.5. Schematic representation of a DNA nanotube. **(a)** ss-DNA containing four segments. The arrow indicated the 3' end. As temperature decreases, the DNA strands first form a two-stranded complex **(b)**, these further associate with each other to form 2-dimensional sheets **(c)**, and eventually fold into nanotubes **(d)**.

The assembled DNA samples were characterized by AFM. Long DNA nanotubes were visualized (Figure 0.6). They are up to 60 μm long and around 6 nm high. The width varies between 30-70 nm. Such DNA nanotubes can serve as templates for nanofabrications, as scaffolds to organize nano-objects, and as a model system for studying the assembly mechanism of other 1-dimensional nanostructures.

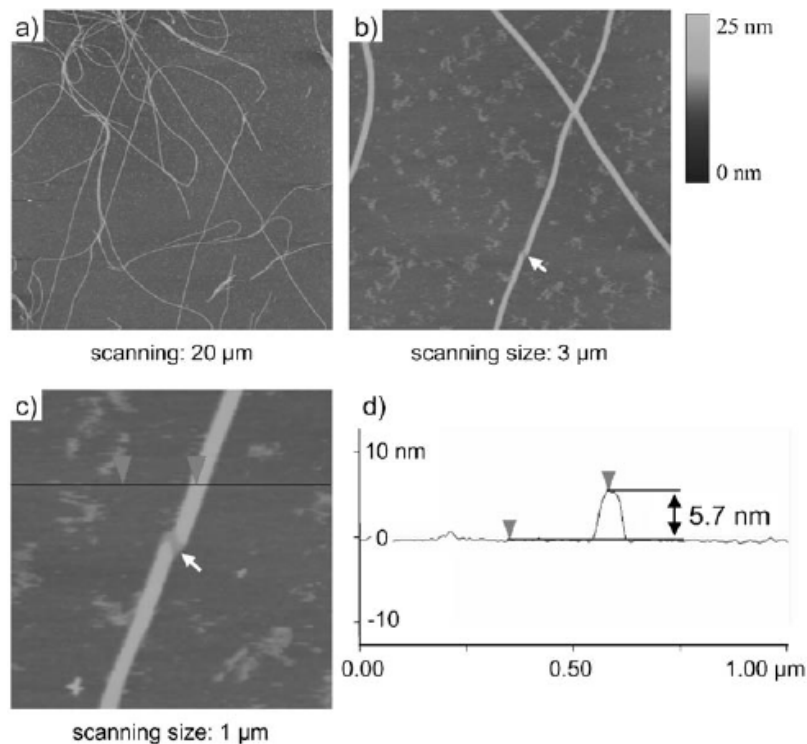


Figure 0.6. (a)-(c): AFM images of DNA nanotubes in buffer. White arrows indicate defects where DNA nanotubes are not completely closed. **(d)** A cross-section profile of the DNA nanotube in **(c)** taken along the black line.

Very recently, Rothemund³ published the folding of long, single-stranded DNA molecules into nanoscale arbitrary 2-dimensional shapes and patterns (Figure 0.7). Their design for a desired shape is made from a 7-kilobase single-stranded scaffold and over 200 short oligonucleotides which hold the scaffold in place. The method here has high yield and is relatively inexpensive. The structures were easy to require and can be used as scaffold origami to create more complex structures. An application would be the attachment of proteins to achieve protein assemblies, whereas molecular electronic or plasmonic circuits might be created by attaching nanowires, carbon nanotubes or gold nanoparticles.

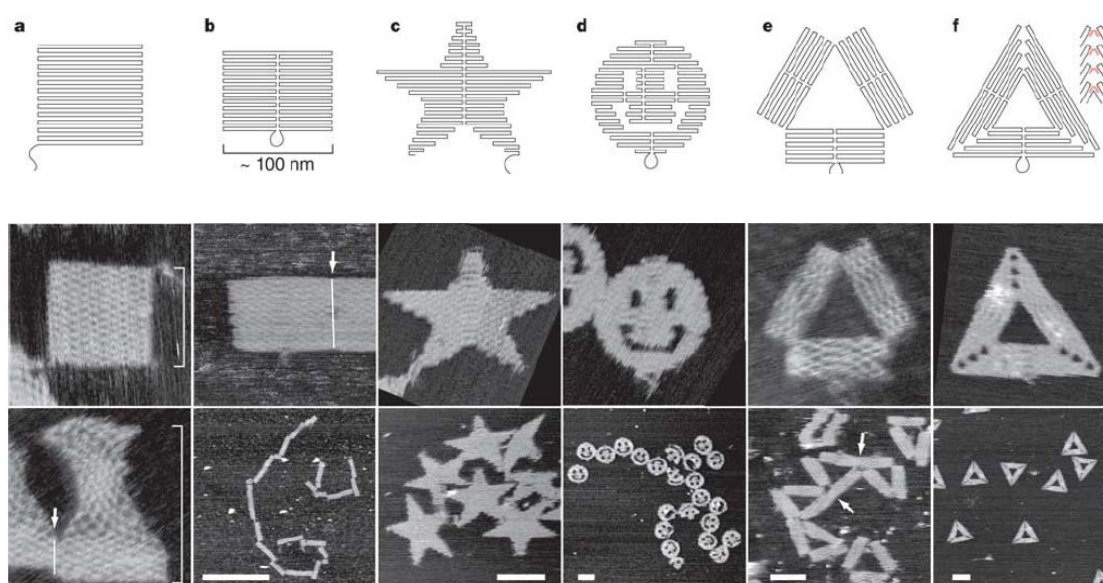


Figure 0.7. (a)- (f): Folding paths of different shapes. **Bottom:** AFM images of the square, rectangle, star, disk, and triangle domains. White lines and arrows indicate blunt-end stacking. White brackets in **a** mark the height of an unstretched square and that of a square stretched vertically. All images without scale bars are the same size, 165 X 165 nm². Scale bars in **b** is 1 μ m and in **c-f** 100 nm.

Since the study on the molecular level in biological system has led to new materials design, interests have been shifted to using biomolecules constructing novel materials. DNA-nanoparticle conjugates become promising

for applications in nanotechnology and biotechnology^{9,10,17,18}. DNA has been used in nanotechnology including DNA-conjugated Au nanocrystals¹⁰, hybrid DNA-protein nanocomplexes¹⁹, DNA-templated Ag wire¹⁴, DNA-mediated supramolecular structures^{20,21}, and DNA-block copolymer conjugates²²⁻²⁴. Mirkin's group produced linear DNA block copolymer consisting of an ODN and a PS fragment²⁵. In this case, coupling of the PS block was carried out on the solid support using standard phosphoramidite chemistry. Micelles with a diameter 8 – 30 nm on mica surface under AFM investigation in air formed in aqueous solution from this amphiphilic block copolymer (Figure 0.8). They have used the micelles in a DNA detection system in combination with DNA-coated gold nanoparticles. The assembled aggregates that consist of micelles and DNA-coated gold can be reversibly disassembled by heating them above the melting temperature of the duplex strand interconnects. In addition, the micelles of amphiphilic DNA block copolymer have been applied as three dimensional scaffolds for DNA-templated organic reactions²⁶.

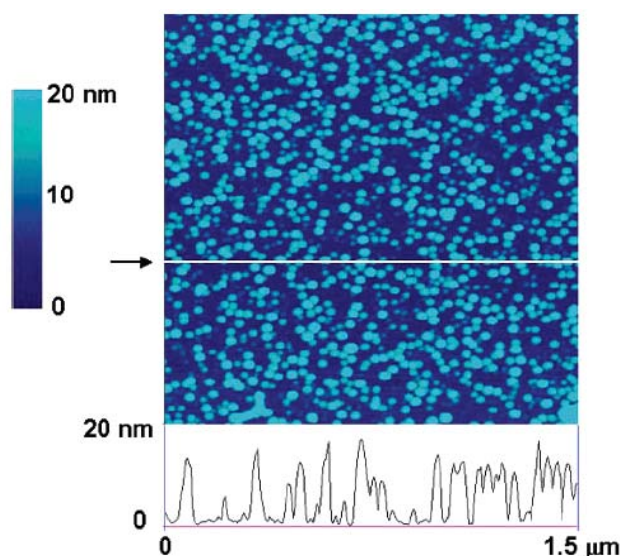


Figure 0.8. AFM image in air showing micelles from PS-DNA amphiphiles.

Since the DNA block copolymers consist of two blocks: DNA block and polymer block, they can be modified by varying the properties of each block. For example, DNA can be ss-DNA or ds-DNA; fully complementary or partly complementary, which leads to different stiffness and flexibility. The length of the DNA block can be changed by varying the number of bases as well. The

molecular weight (M_w) of the polymer block can be different. Different polymers can be applied in order to achieve different properties. For example, PS or polypropylene oxide (PPO) can be used to achieve amphiphilic block copolymer. However, polyethylene oxide (PEO) will lead to a block copolymer with both blocks hydrophilic.

My study was focused on the structure of amphiphilic DNA block copolymers in solutions and on surfaces. This work was partially supported by DFG-Sonderforschungsbereich 625 "From Single Molecules to Nanostructured Materials". The amphiphilic DNA block copolymers were synthesized in the group of A. Herrmann by F. E. Alemdaroglu at MPIP Mainz. The aim is to study the possibility to generate different architectures from DNA block copolymers in solutions and on surfaces. In water solution, amphiphilic block copolymers may form single molecules, dimers, or self-assembled lamellas (Figure 0.9) below the CMC.

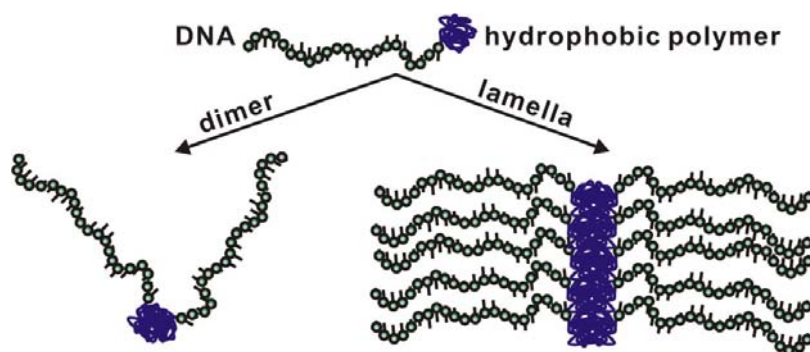


Figure 0.9. The hypothesized model for single molecule, dimer, and 2-dimensional lamella structures from amphiphilic ss-DNA block copolymer.

When the concentration of these amphiphilic molecules is increased to \geq CMC value, globular micelles may form with ss-DNA in the corona in water (Figure 0.10). Upon hybridization with complementary sequenced ODNs will lead to a formation of ds-DNA block copolymer micelles. The ss-micelles could be used as 3-dimensional scaffolds for DNA templated organic reactions. Reaction may proceed at the rim of the corona (Figure 0.10) when equimolar amounts complementary ODNs were equipped with reactants at the 5' end.

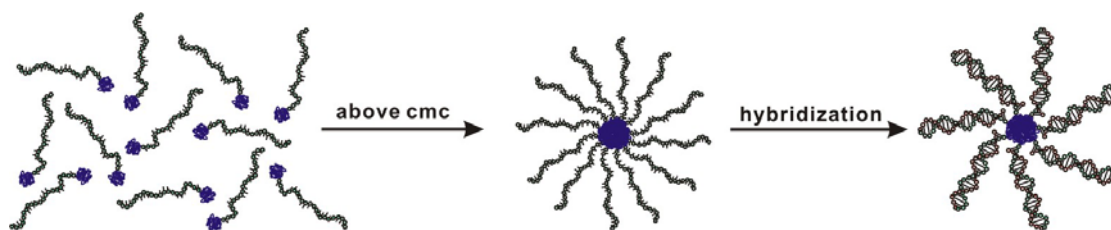


Figure 0.10. Schematic illustration of the globular micelle formation from amorphous amphiphilic ss-DNA block copolymer above CMC. Further hybridization with complementary sequenced ODNs results in ds-DNA block copolymer micelle.

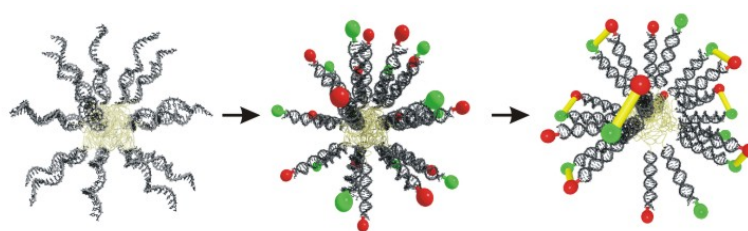


Figure 0.11. Schematic illustration of micelle templated synthesis. The micelles consist of a hydrophobic core and a shell of DNA. Single stranded micelles can be hybridized with ODNs that are equipped with reactants (green and red balls). The subsequent chemical reaction proceeds at the surface of the micelle.

The globular micelles may be hybridized with long ss-DNA template molecules that consist of complementary sequence. Figure 0.12 shows three possible structures upon this molecular recognition event. The micelle is partially hybridized by controlling not only the ratio between long template and the DNA block copolymer but also the number and position of the complementary sequences between them (a in Figure 0.12). When the ratio of template to DNA block copolymer becomes 1:1, fully hybridized globular micelles may form with rest ss-DNA molecules on micelle surface (b in Figure 0.12). Furthermore, the micelles may change from globular to rod like structures by adjusting the base sequences on template and the ratio between template and block copolymer so that the template is fully hybridized with repeating block copolymers (c in Figure 0.12).

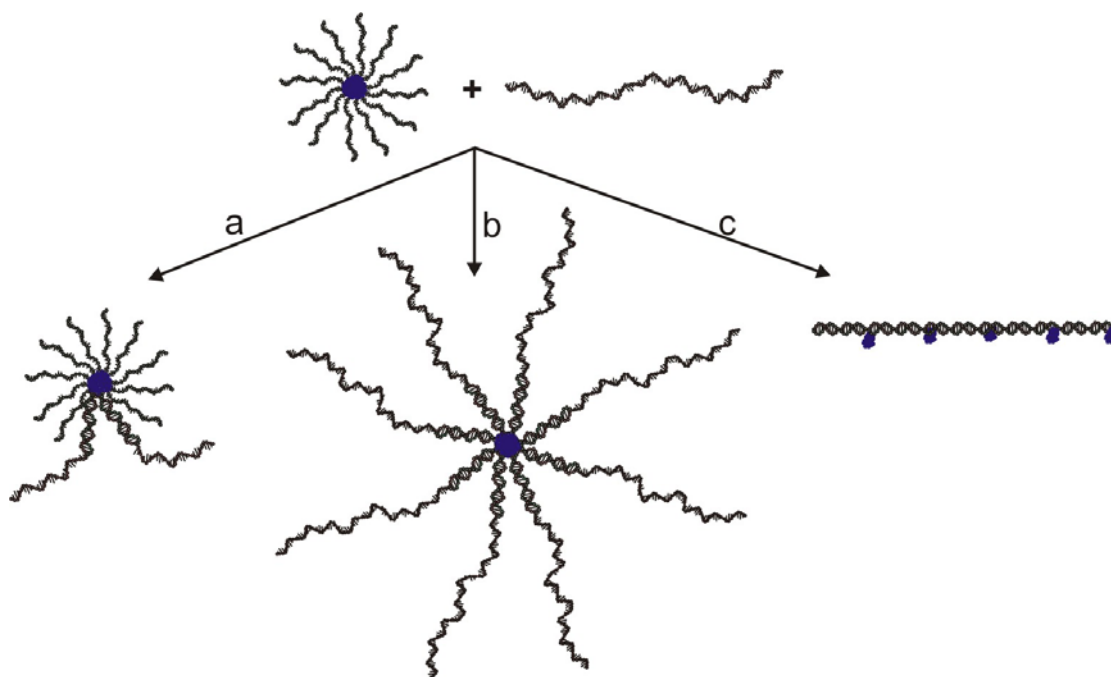


Figure 0.12. The hypothesized model illustrating that micelle is hybridized partially (a) or fully (b, c) with long ss-DNA template.

By placing the polymers in certain positions, different kind of assembly would be possible. For example, when the polymers are placed in the same direction by keeping their positions one after 22 bases which is about 2 helix turn, pairs of rods may form upon the hydrophobic interaction (Figure 0.13). On the other hand, the PPOs could also be placed in the way that neighboring PPOs are always at 180° by keeping them one after 1.5 helix turn. We assume that 2-dimensional lamellar would be formed based on the hydrophobic interaction between polymers (Figure 0.14).

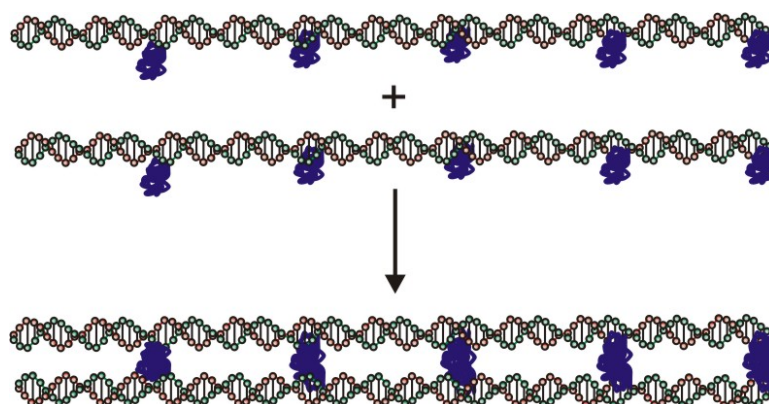


Figure 0.13. The hypothesized model of a pair of rods formation.

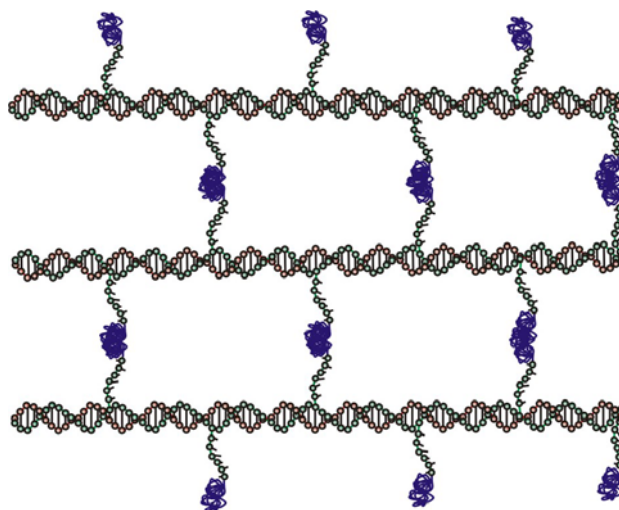


Figure 0.14. *The hypothesized model of a 2-dimensional lamellar structure.*

AFM is a proper method for study the surface structures in biological and polymer systems²⁷⁻³². An atomic force microscope uses a sharp probe which scans across the sample to achieve a 3-dimensional image of the surface and to provide a topographic map of the sample. We have used AFM to investigate DNA block copolymers structures because it gives the advantage when imaging biological specimens and delicate materials in their natural, fluid environments. The atomic force microscope operates on surfaces, which is very helpful for us to find out the surface structures of DNA block copolymers. The resolution of the AFM in nanometer scale allows imaging of single molecules. Owing to the simple operation principle, atomic force microscope requires rather easier sample preparation than that for electron microscope. Moreover, atomic force microscope can be operated in different environments including air, liquid and vacuum, which allows in-situ observation of biological system in their natural medium.

In this thesis I am going to present different surface structures of amphiphilic DNA-*b*-PPO and DNA-*b*-PS by AFM. Different architectures including single molecules, dimers, globular micelles, cylindrical micelles, dendritic patterns, and rod like structures have been observed on different surfaces (mica, graphite, or silicon). In-situ AFM studies under liquid conditions illustrate that the structures are dependent on the hybridization conditions on DNA, the substrate properties, the salt concentration in buffer solution, the chemical

modification at the end of DNA strands, the binding position between DNA and polymer, the equilibrium time, and the concentration. Whereas the measurements in air conditions show that the structures are dependent on molecular weight in polymer block, temperature, humidity, and substrate. In addition to AFM, DLS and FCS investigations have been done to confirm the AFM results by polymer analysis group of Prof. Dr. Gerhard Wegner in MPIP Mainz and by Dr. Michael Börsch in University of Stuttgart, respectively.

Chapter 1 introduces the fundamentals together with sample preparations of AFM, DLS, FCS, and SPR. *Chapter 2* introduces the synthesis process of DNA block copolymers. *Chapter 3* will emphasize on the in-situ AFM studies on DNA block copolymers and discussion on the observed structures. At the end of this chapter, AFM studies in air on DNA block copolymers will also be presented.

1 METHODS

1.1 Atomic Force Microscopy

AFM and scanning tunneling microscopy (STM) are the two mostly used scanning probe microscopy (SPM). SPM is a family of microscopes where a sharp probe is employed for profiling surfaces with high resolution. STM was developed by Binnig, Rohrer, Gerber, and Weibel at IBM in Zurich, Switzerland in 1982. Binnig and Rohrer received the Nobel Prize for the invention of STM together with Ruska for scanning electron microscopy (SEM) invention in Physics in 1986. The AFM, also called scanning force microscopy, was invented in 1986 by Binnig, Quate, and Gerber in collaboration between IBM and Stanford University³³. It overcame the limitation of STM in imaging thin samples on electrically conductive materials. In addition to the high resolution, atomic force microscope offers the possibility to characterize surface mechanical properties and surface forces of the samples on the nanometer scale.

1.1.1 Instrumentation

Atomic force microscopes can be operated in vacuum, air or liquids including water. This opened the range of applications especially for biological samples being imaged in physiological solution. The AFM was first applied to polymer samples in 1988³⁴. The essential instrumental components in an atomic force microscope are: A sharp tip mounted on a cantilever spring, a cantilever deflection sensor, an electronic feedback system, a data display and a mechanical scanning system. The sample is fixed on a piezoelectric scanner. Then the sample is scanned by the tip along the x-y plane (Figure 1.1).

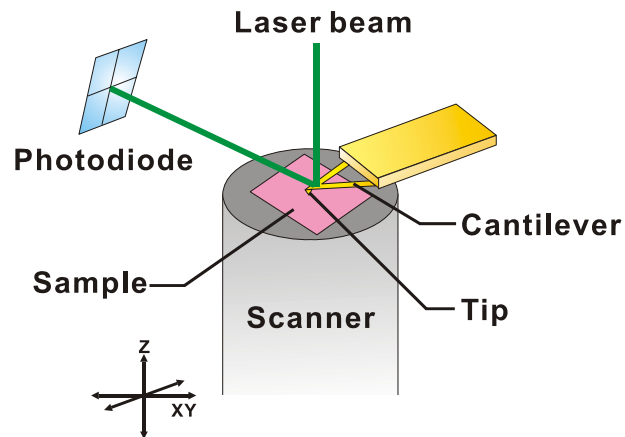


Figure 1.1. Set-up of an AFM. The cantilever is fixed to a support. The tip is attached to the end of the cantilever towards sample. The sample surface is scanned by the tip during the movement of the piezoelectric scanner in x and y directions. The laser beam is focused onto the back side of the cantilever and reflected on a photodiode. The cantilever deflections are monitored during the scanning process for obtaining the surface topography.

Scanners in AFM are made from piezoelectric material, which expands and contracts proportionally to an applied voltage. Whether they expand or contract depends upon the polarity of the applied voltage. The scanner is constructed by combining independently operated piezo electrodes for x, y, and z into a single tube, forming a scanner that manipulate samples and tips with extreme precision in 3 dimensions.

The cantilever is integrated with a sharp tip on the end and they are made of silicon nitride, silicon oxide or silicon with standard techniques used in semiconductor industry³⁵⁻³⁷. The tip properties are essential for the image quality. Tips with small radius of curvature at the end are able to obtain good lateral resolution and to reduce the total force. One important property of the cantilever is its resonance frequency ν_0 . It should be high enough in order to get a low coupling of external vibrations to the cantilever. External vibrations, such as movements of the building or table, are in the range of 1-100 Hz. Coupling is less effective when the resonance frequency is far from the exciting frequency. Hence, the higher the resonance frequency, the less sensitive the cantilever is to external vibrations. In addition, the higher the resonance frequency, the faster the cantilever can respond when imaging³⁸.

The resonance frequency of a cantilever with a rectangular cross section is given by equation (1. 1) where d is the thickness and L the length of the cantilever. E is the Youngs modulus and ρ the density of the material.

$$v_0 = 0.164 \times \frac{d}{L^2} \times \sqrt{\frac{E}{\rho}} \quad (1. 1)$$

Another important property is its spring constant K . In contact mode (will be introduced in the following section) most cantilevers have a spring constant <1 N/m in order to obtain small forces because the stiffness of the cantilever needs to be less than the effective spring constant (1-10 N/m) holding atoms together. The spring constant for a cantilever is given by equation (1. 2) where w is the width of the cantilever.

$$K = \frac{Ewd^3}{4L^3} \quad (1. 2)$$

The cantilever is deflected by forces applied between the tip and the sample. There are several methods for measuring the cantilever deflection. Beam deflection is the widely used technique. An optical detection system, consisting of a laser beam which is focused onto the back of the cantilever towards a split photodiode, monitors the cantilever deflection. In this way the cantilever deflection is detected by the split photodiode detector and converted into an electronic signal. The feedback loop is used to control the scanning mode and to direct the piezoelectric scanner movements.

1.1.2 Imaging modes

Usually images are taken in two scanning modes: contact mode or tapping mode.

Contact mode

The tip is actually in contact with the sample. The cantilever deflection is a measure of the force exerted between the tip and the sample. The surface structure can be imaged at constant height or at constant force. In the

constant height mode the vertical distance between the base of the cantilever and the sample is kept fixed by the electronic feedback. The motion of the cantilever generates the topographic image. The most widely used mode is that at constant force. In this case the normal force between tip and sample (i.e. cantilever deflection) is maintained constant by a feedback loop. This is achieved by regulating the height of the scanner. Typical spring constants for contact mode are in the range of 0.01-0.2 N/m with resonance frequencies of 5-50 kHz. Usually it takes 30-60 sec to record an image.

Tapping mode

The cantilever vibrates at (or close to) its resonance frequency over the sample. The vibration amplitude is sensitive to the distance between tip and sample: If the tip starts to get into contact with the surface, its vibration amplitude is reduced. Therefore, the amplitude of the vibration, which is typically 20-200 nm in tapping mode, is the parameter that the system regulates on. The height of the sample is positioned according to a given value of the amplitude, which must be lower than the free vibration amplitude. The resonance frequencies and the spring constants are in the order of 300 kHz and 40 N/m, respectively. Typically it takes about 10 min to record an image.

Most of my work has been done in tapping mode due to the advantages of tapping mode:

- There are no lateral forces i.e. frictional forces or shear forces which can damage the sample or the tip. Therefore, softer samples can be examined in tapping mode than in contact mode.
- The contact time between tip and sample is reduced. With a usual resonance frequency of 300 kHz and assuming that the tip is only 10% of each period in actual contact a typical contact time is 0.3 μ s. This time is often too short to change the sample surface.

Height and phase images can be recorded under tapping mode imaging. A height image records the topography of the surface structure of sample. The vertical position of the scanner at each (x, y) data point in order to maintain a constant “setpoint” amplitude is stored by the computer to form the topographic image of the sample surface. A phase image displays the difference in phase angle of the input drive signal with respect to the phase of the oscillating cantilever. As the tip engages the sample surface, the phase angle of the oscillating cantilever changes with respect to the phase angle of the input drive signal. This angle changes e. g. if regions of different elasticity are encountered on the sample surface. Phase image often provides significantly more contrast than the topographic image and has been shown to be sensitive to material surface properties, such as stiffness, viscoelasticity, and chemical composition. In general, changes in phase angle during scanning are related to energy dissipation during tip-sample interaction. Cleveland et al.³⁹ showed that the sine of the phase angle of the driven vibration is proportional to changes in the tip-sample energy dissipation if the amplitude of the cantilever is held constant. Depending on the operating conditions, different tapping forces might be applied on different samples. Changes in tapping force will often affect the phase image, particularly with regard to whether local tip-sample interactions are attractive or repulsive. The dependence of phase angles in tapping-mode AFM on the magnitude of tip-sample repulsive interactions was investigated by Whangbo et al.⁴⁰. Phase images of several hard and soft samples were recorded as a function of the free amplitude A_0 and the set-point tapping amplitude A_{sp} . The phase angle of probe oscillation increases with decreasing the set-point amplitude ratio A_{sp}/A_0 .

1.1.3 Imaging in liquid

The fluid cell consists of a small glass assembly with a wire clip for holding an AFM probe. The probe is held in a small pocket on the bottom side of the fluid cell by a gold-plated, stainless steel wire clip. A tiny coil spring mounted on the top of the fluid cell holds the wire clip against the probe. The glass

surfaces provide a flat interface so that the AFM laser beam may pass into the fluid without distortion. The volume of liquid in the fluid cell is limited to 30-50 μl .

Usually an O-ring is used to seal the AFM scanner from spilled liquids. It is positioned to form a seal around its periphery. There is minimal lateral movement of the optical head with respect to the sample once the O-ring is installed.

In many conditions, it is possible to image a sample under a drop of fluid without use of a closed fluid cell. This technique is recommended for aqueous buffers, when evaporation is not an issue. Drift can be minimized and air bubbles form in the fluid cell and block laser light can be avoid without O-ring (Figure 1.2).

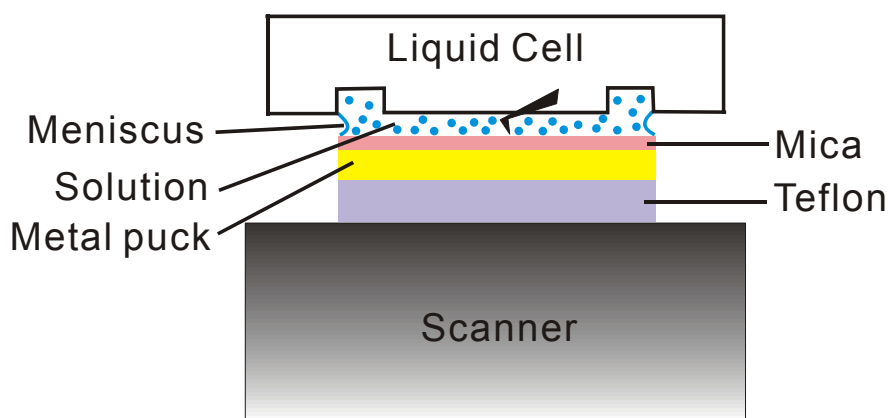


Figure 1.2. Cross section of the set-up for liquid measurement. The cantilever with chip is fixed on the bottom of a quartz glass liquid cell. The meniscus of water solution sealed the area between sample and liquid cell. The mica is glued onto a metal puck that is fixed on a Teflon head.

Operation of TappingMode in fluid provides the same advantages of TappingMode in air, with the additional ability to image samples under native liquid conditions. In the tapping mode, A_0 is the amplitude of the free-oscillating cantilever. A_{sp} is the set-point amplitude. A set-point ratio $r_{sp} = A_{sp}/A_0$ determines the force applied. Light or soft tapping corresponds to a ratio in the 0.95-0.1 range. Hard tapping corresponds to a ratio in the 0.4-0.5 range⁴¹.

As for a reference experiment to check imaging conditions for DNA based experiments, ds circular DNA containing 4361 base pairs (plasmid pBR322) has been imaged by AFM under tapping mode in buffer (Figure 1.3). Both of the height and phase images showed DNA structures in supercoiled or linear shape on mica surface with high resolution. The observed structures is consistent with those from the literatures ^{42,27,28}. The height of them is between 0.6-0.8 nm and the width is around 15 nm. The disagreement of these values with theoretic one (2 nm wide for ds-DNA) is due to the tip radius of curvature. Moreover, the force applied between the tip and sample during imaging process could result in the deformation of the structure ⁴¹.

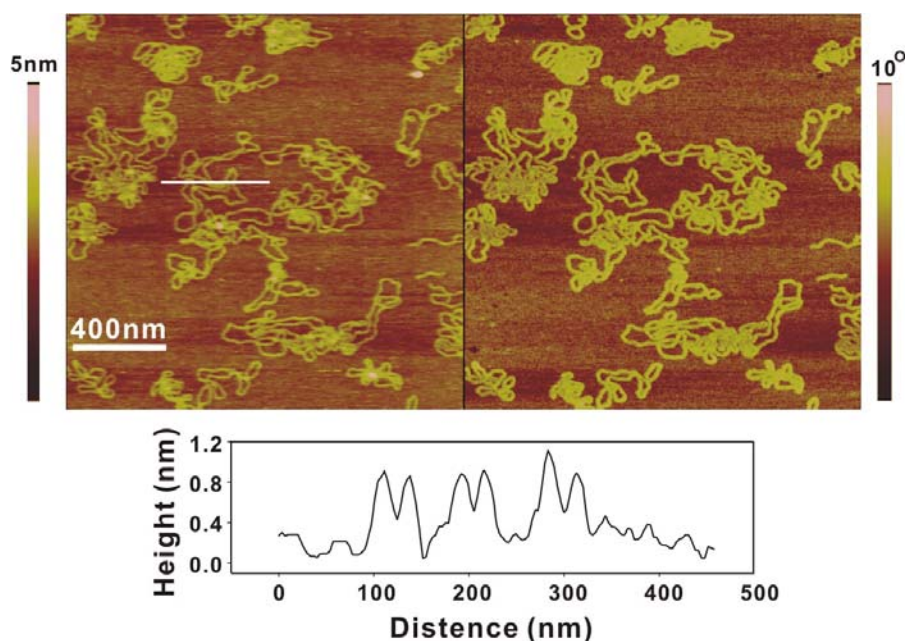


Figure 1.3. *Top:* Tapping mode height (**left**) and phase (**right**) images ($1.7 \times 1.7 \mu\text{m}$; scale bar 400 nm) of a pBR322 layer on mica in buffer solution. The concentration was $2.5 \text{ ng}/\mu\text{L}$ and Z range is 5 nm for height image and 10° for phase image. **Bottom:** Section analysis across the white line in AFM height image indicated by the white bar.

1.1.4 Image interpretation

There are mainly three factors influencing the resolution of an AFM image: the tip shape, the deformability of the object, and the smoothness of the substrate. The image can be determined by the geometry of tip and sample when both are supposed to be infinitely hard. In the real cases, the influence by tip effect

should always be considered. The interpretation is relatively simple when a small tip is imaging a large flat object because the tip is considered as a point like probe and the measured topography is authentic. However, when imaging a relatively small object by a blunt tip, the true surface structure can not completely reconstructed by image processing because the observed image contains no information about the structure of depressions ⁴³. As shown in Figure 1.4, the topographic image contains the shapes of both the surface and the tip on top and contains the shape of the tip on bottom. The surface structures can not be exactly reproduced in both cases.

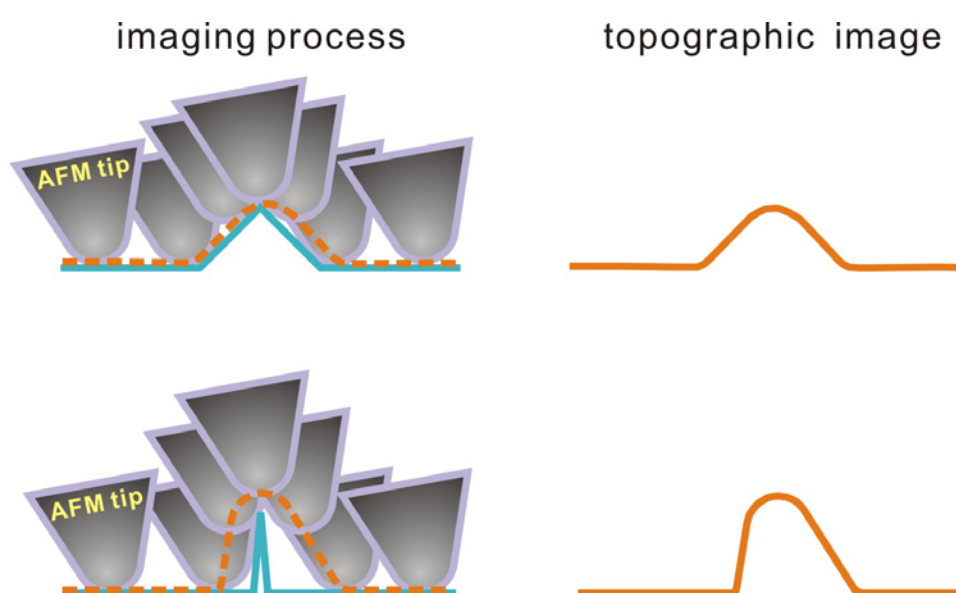


Figure 1.4. Sketch of imaging a surface by an AFM tip. **Top:** the topographic image contains the shapes of both the tip and the surface. **Bottom:** the topographic image shows exactly the shape of the tip by imaging a relatively small object.

1.1.5 Sample preparation

Imaging in liquid

The DNA block copolymers were supposed to adsorb on mica surface due to the positive Ni^{2+} ions in buffer solution and the negative charged DNA and Mica. The Ni^{2+} served as a bridge to bind DNA to mica. The transition metal cations such as Ni^{2+} , Co^{2+} , and Zn^{2+} have been found binding DNA to mica effectively ⁴⁴. Bustamante and co-workers ⁴⁵ have used statistical polymer

chain analysis to study the deposition of DNA from solution onto surfaces such as mica. Kinetic studies indicated that DNA molecules are transported to the surface solely through diffusion, and once on the surface they cannot return to solution. Further, DNA molecules deposited in low salt solutions onto freshly cleaved mica do equilibrate on the surface and short molecules (<20 persistence lengths) behave as ideal worm-like chains in two dimensions. DNA molecules deposited onto glow-discharged mica or H⁺ ion exchanged mica, however, do not equilibrate on the surface.

Typically a drop of 20 μl of sample (concentration ranges between 1-100 ng/ μL) solution in buffer (10 mM Tris PH 7.4, 100 mM NaCl, 1 mM NiCl₂) was deposited onto freshly cleaved mica (Plano GmbH, Germany) and left for incubation for 5 min. The sample was then rinsed with 200 μl buffer solution and mounted onto a piezoelectric E-scanner (Veeco Instruments, California USA). In particular, we paid attention that the sample was always kept wet during the sample handling. Imaging was performed under tapping mode AFM in a liquid cell on a Multimode Nanoscope IIIa (Veeco Instruments, California USA). The NP-S oxide-sharpened silicon nitride cantilevers (Veeco Instruments, California; 115 μm long, 17 μm wide, 0.6 μm thick) with an integrated tip (a spring constant of 0.32 N/m and a resonance frequency of 56 KHz in air) have been used. A driving frequency between 8 – 10 kHz for imaging was selected in existence of buffer solution. The height of the tip is 2.5 to 3.5 μm and the tip radius is inspected by SEM measurement. A piezoelectric E-scanner supplies a maximum x, y-scan of 12.5 μm and a z-extension of 2.5 μm . The scanner was calibrated by imaging a rectangular grid of 10 μm mesh size. AFM images (512 x 512 pixels) were recorded with a scan size of 1x1 μm^2 at a scan rate of 1Hz. The free amplitude to amplitude setpoint ratio was set to be close to 1.0 to adjust soft tapping mode⁴¹. The raw data has been modified by applying the first order “flatten” filter. The maximum height of the aggregates was calculated by means of local roughness analysis.

The tip radii were measured by scanning electron microscopy after having performed the AFM measurements. For the images presented we determined tip radii of curvatures < 20 nm (Figure 1.5 a). In some cases double tips have been found (Figure 1.5 b). These tips can produce imaging artifacts appearing as double structures in the topography (bottom AFM image in Figure 1.5). Therefore all measurements where we found double tips were not considered.

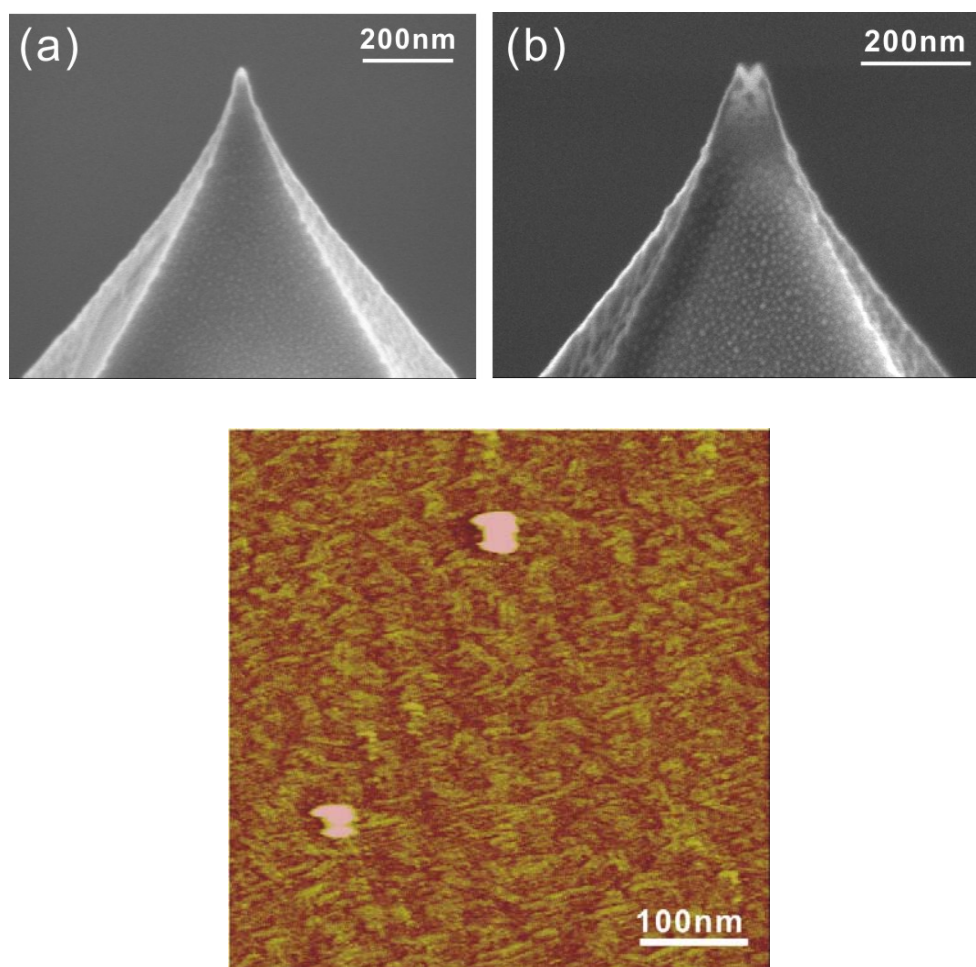


Figure 1.5. *Top: SEM pictures on a normal tip (a) and a double tip (b). Bottom: An AFM height image showing typical double tip artifacts.*

Imaging in air on drop casted films

First of all a drop of 20 μL sample (typical concentration 5 $\text{ng}/\mu\text{L}$) solution in water was deposited onto plasma cleaned silicon (Silicon-Materials, Germany), fresh cleaved mica (Plano GmbH, Germany) or fresh cleaved graphite (HOPG. Co. Adi Hassel) substrate. Then the sample was stored

inside a petridish for at least 24 h for evaporation of water before making AFM investigation.

A commercial AFM (Multimode, Nanoscope IIIa, Veeco Instruments, California USA) has been applied under tapping mode together with a piezoelectric E-scanner (Veeco Instruments, California). Arrow™ NCR cantilevers (Nanoword, Switzerland; 160 μm long, 45 μm wide, and 4.6 μm thick) have been used. The spring constant and the resonance frequency of these cantilevers are 42 N/m and 285 KHz, respectively.

For the measurements involved heating and changing humidity, an EnviroScope AFM (Veeco Instruments, California USA) was applied under tapping mode. The equipped scanner supplies a maximum x, y-scan of 90X90 μm² and a z-extension of 5 μm. Especially for the heating system, the silicon cantilever (DMCL-AC 240TN) which has a resonance frequency of 70 KHz in air and spring constant of 2 N/m has been used.

1.2 Light scattering

Light scattering (LS) is a technique for characterizing macromolecules and a wide range of particles in solution. There are two different light scattering methodologies: static light scattering (SLS) and dynamic light scattering (DLS).

SLS provides a direct measurement of molecular mass by measuring the amount of light scattered at some angle relative to the incident laser beam. Here, the intensity of the scattered light is measured as a function of angle. For the case of macromolecules, this is often called Rayleigh scattering and can yield the molar mass, dimension, shape, and structure of samples.

DLS is a generic term encompassing all of the light scattering methods that provide information about the molecular dynamics⁴⁶. In DLS one measures the time dependence of the light scattered from a very small region of solution, over a time range from tenths of a microsecond to milliseconds. The fluctuations in the intensity of the scattered light are related to the diffusion rate of molecules in and out of the region being studied due to Brownian

motion. DLS can be used to measure molecular motion and diffusion coefficients in polymers and colloids. In DLS, the scattered intensity is mostly due to concentration fluctuations. Intensity and electric field correlation functions are used for quantification and the data can be analyzed to directly give the diffusion coefficients of the particles doing the scattering. When multiple species are present, a distribution of diffusion coefficients is seen. The decay time distribution is equivalent to a diffusion coefficient distribution that corresponds to a distribution of hydrodynamic radii via Stokes-Einstein relationship (1.3). D is the diffusion constant; K_B is the Boltzmann constant; T is the temperature in Kelvin degree; η is the viscosity of the solvent; and the r_H is the hydrodynamic radius.

$$D = \frac{K_B T}{6\pi\eta r_H} \quad (1.3)$$

DLS can be used to study aggregation, adsorption, and structural changes as well as chain dynamics^{47,48}. The experimental set up is illustrated in Figure 1.6. The laser passes through a collimator lens and hits the cell with solution. The light is scattered and detected by a photomultiplier that transform the intensity variation into the voltage variation. There is a second collimator lens before the photomultiplier. The use of first lens is to focus the beam into the cell and of the second one is to collect scattered light. After the photomultiplier, the signal is preamplified and then sent to the computer.

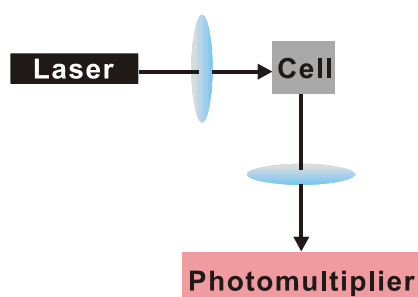


Figure 1.6. Set-up of a DLS system. The laser beam is focus onto the cell with sample

solution through a collimator lens and the light is scattered and detected by a photomultiplier

1.2.1 Sample Preparation

Dynamic light scattering (DLS) at 25°C was done for characterization of micelles using a dynamic light scattering photometer (ALV 5800, Avalanche Photodiode) equipped with He-Ne laser at a wavelength of 632 nm by polymer analysis group of Prof. Dr. Gerhard Wegner in MPIP Mainz. The data were gathered and processed using the ALV 5000/E software. The samples prepared in buffer medium were dialyzed against deionized water before the measurement. The measurements were carried out in triplicate.

1.3 Fluorescence Correlation Spectroscopy

Fluorescence correlation spectroscopy (FCS) is a spectroscopic technique for the study of kinetic processes through the statistical analysis of equilibrium fluctuations⁴⁹. It monitors the random motion of fluorescently labeled molecules inside a defined volume element irradiated by a focused laser beam. The correlation analysis of fluctuation in the fluorescence intensity carries physical parameters under the fluctuation. These fluctuations provide information on the rate of diffusion or diffusion time of a particle. This is directly dependent on the particle's mass. Consequently, any increase in the mass as a result of an interaction with a second molecule is readily detected as an increase in the particle's diffusion time.

The experimental setup is shown in (Figure 1.7). The laser beam is aligned into the back aperture of an objective via a dichroic mirror. The fluorescence light is collected by the same objective. After passing a dichroic mirror and an emission filter the fluorescence light is focused onto a pinhole. Finally the light is focused on a light detector such as an avalanche photo diode (APD).

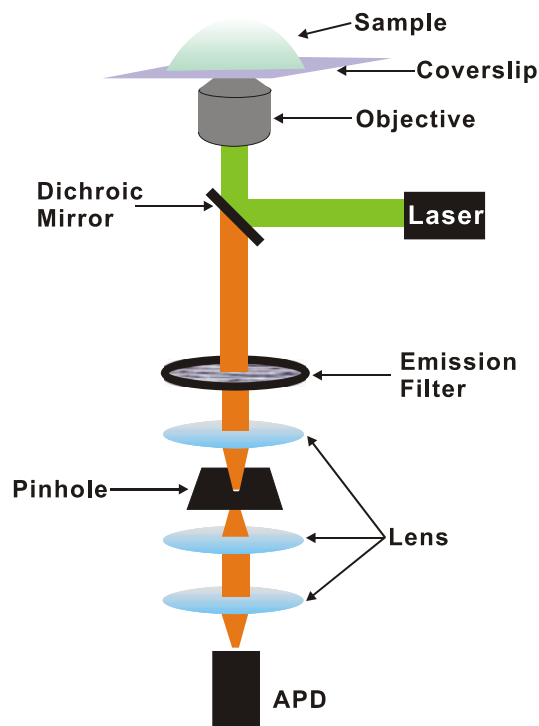


Figure 1.7. Set-up of a FCS system. Sample is positioned on a coverslip above the objective. The laser beam is aligned into the back side of the objective via a dichroic mirror. The fluorescence light is collected by the same objective and is focused onto a pinhole after passing a dichroic mirror and an emission filter. Finally the light is focused onto an avalanche photo diode (APD).

The autocorrelation function $G(t)$ is defined as equation (1.4) where $F(t)$ is the fluorescence detected at time t . In principle, the kinetic coefficients for all of the processes contribute to the decay of $G(t)$, and so all of them can be determined from the autocorrelation function.

$$G(t) = \frac{\langle F(t+\tau)F(t) \rangle_t}{\langle F(t) \rangle^2} \quad (1.4)$$

FCS is an ideal approach for the study of thermodynamic and kinetic features of molecular interactions in solution. For example, it can be applied on analysis of the concentration fluctuations of fluorescent particles in solution. The fluorescence containing small amount of fluorescent particles is emitted from a tiny space in solution. The intensity of fluorescence is fluctuating due to Brownian motion of the particles and the analysis gives the average number of the fluorescent particle and average diffusion time. Consequently both

concentration and size of the particle are determined. Since the method is working on small number of molecules in the tiny spot, it is very important for investigating dynamical processes in the biochemical research, biophysics and chemistry. FCS is focusing on the fluctuation arising from the molecular kinetics and ignores the large scale fluctuation of the system. Therefore the system size is limited in order to observe the fluctuation due to the kinetics. On the other hand, this method can apply to the single molecule detection if the background is sufficiently suppressed.

1.3.1 Sample preparation

FCS measurement has been done by Dr. Michael Börsch in University of Stuttgart, Germany. The ss-DNA-*b*-PPO micelles were hybridized with the complementary sequences functionalized with Alexa488 (Invitrogen, USA) at the 5' end. The ratio of ss-DNA-*b*-PPO to ODN carrying the dye was adjusted to be 1% so that the predominant form of DNA within the corona remains single stranded. Then they were completely hybridized with the complementary sequence to obtain double stranded micelles. For the molecules of DNA-*b*-PPO-T88, DNA-*b*-PPO-T100, and DNA-*b*-PPO-T110, ss-DNA-*b*-PPO was hybridized with equimolar amounts of Cy3 modified T88, T100, and T110 molecules.

FCS measurements were carried out on a confocal setup of local design based on an Olympus IX71 inverted microscope. The 488 nm line of an argon ion laser (model 2020, Spectra Physics) was attenuated to 150 μ W before focusing into the buffer solution by a water immersion objective (40 X, N.A. 1.15, Olympus). The solution was placed on a microscope cover slide as a droplet of 25 to 50 μ L. Scattered laser light was blocked by a dichroic beam splitter (DCXR 488, AHF, Tübingen, Germany), and fluorescence was collected in the spectral range from 532 to 570 nm using interference filters (AHF). Single photons were detected by an avalanche photodiode (SPCM AQR-14, Perkin Elmer) and registered by a TCSPC device (PC card SPC-630, Becker & Hickl, Berlin, Germany) for software calculation of the

autocorrelation functions, or by a real time hardware correlator (PC card ALV-5000 E, ALV, Langen, Germany).

The fluorescence intensity autocorrelation functions, $G(\tau_c)$, were fitted with a single diffusion time, τ_D , for the sample according to equation (1.5) with N_f , average number of fluorescent molecules in the confocal detection volume, τ_c , correlation time, ω/z , the ratio of the $1/e^2$ radii of the detection volume in radial and axial directions, T , average fraction of fluorophores in the triplet state, and τ_T , lifetime of the triplet state of the fluorophore. The ω/z was measured with a R6G solution as the reference and was kept fixed at this value during the subsequent fitting of the autocorrelation functions of the DNA-PPO micelle solutions. The diffusion coefficient, D , is related to the diffusion time by equation (1.6) and to the frictional coefficient f of a sphere with radius R_0 by equation (1.7), which allows for the calculation of the radii of the spherical micelles.

$$G(\tau_c) = \frac{1}{N_f} \left(1 + \frac{\tau_c}{\tau_D}\right)^{-1} \left(1 + \left(\frac{\omega}{z}\right)^2 \left(\frac{\tau_c}{\tau_D}\right)\right)^{-1/2} \left(1 - T + T \exp\left(-\frac{\tau_c}{\tau_T}\right)\right) \quad (1.5)$$

$$\tau_D = \omega^2 / 4D \quad (1.6)$$

$$f_{sphere} = KT / D = 6\pi\eta R_0 \quad (1.7)$$

The rigid, non-spherical molecules can be modeled in terms of some ideal shape. For instance, virus particles can be modeled as rods or ellipsoids of rotation.

1.4 Surface plasmon resonance spectroscopy

Over the past two decades, surface plasmon resonance spectroscopy (SPR) has become a widely accepted optical technique to investigate surface/interfacial phenomenon with high sensitivity. A surface plasmon is based on the collective oscillation of the (nearly) free electron gas at a metal/dielectric interface. It propagates along the x-direction of this interface as a damped oscillatory wave (Figure 1.8). Surface plasmons decay rapidly and exponentially within the metal and the dielectric.

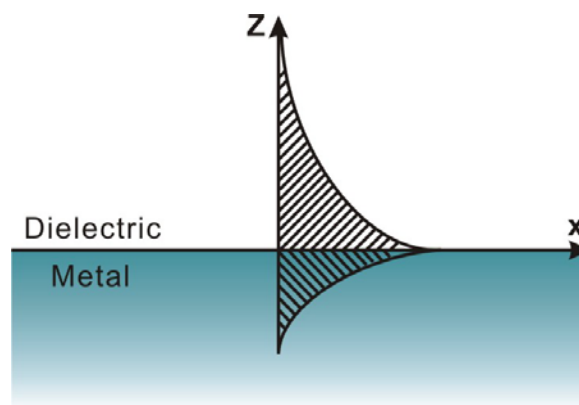


Figure 1.8. Schematic representation of surface plasmon propagation at a metal/dielectric interface.

Surface plasmons can be excited either by electrons passing through a thin metal film or by photons incident on a metal surface. They can not be excited by externally incident light because the wavevector of surface plasmons do not match with that of the incident light regardless of the wavelength. However, the excitation of surface plasmons is possible by a proper coupling of the light. Experimentally, the evanescent wave, characterized by a large momentum, is widely employed to excite surface plasmon resonances. The evanescent wave, associated with total internal reflection, is an optical phenomenon at the interface of two media with different dielectric properties. Total internal reflection occurs above a certain incidence angle (i.e., the critical angle) if the light wave propagates from the dielectric with high refractive index to the dielectric with low refractive index. The critical angle, θ_c , can be derived by Snell's law:

$$\sin \theta_c = n_d / n_p \quad (1.1)$$

Here n_d and n_p are the refractive index of the dielectric and the prism, respectively. When incident angle is smaller than θ_c , most of the incoming light is transmitted and the reflected light is low. Above θ_c , an evanescent wave generates and decays exponentially into the dielectric in z-direction. In such conditions, an evanescent wave can be employed to excite a surface plasmon at the metal/dielectric interface.

Since surface plasmon propagates in the x-direction, only the x-component of the evanescent wave is relevant to the excitation of a surface plasmon. By changing the incident angle, one can adjust wavevector of photons (k_{ph}) from zero at normal incidence to the full wavevector k_{ph} at grazing incidence by $k_{ph}^x = k_{ph} \times \sin \theta$. At a certain angle of incidence, resonant coupling between the evanescent photons and the surface plasmons can be obtained because the energy and the momentum matching conditions are fulfilled.

Surface plasmons can be excited by using the evanescent wave in a prism coupling arrangement (i.e. the Kretschmann configuration). The system is based on the attenuated total internal reflection and is widely applied for practical surface plasmon resonance spectroscopy. In this configuration (Figure 1.9), a thin metal layer is evaporated directly onto the base of the prism or a glass slide which is then index-matched to the base of the prism. The photons in the prism couple through the thin metal layer to the surface plasmons on the other side which is in contact with the dielectric medium. The thickness of the deposited metal film can be controlled easily. The thickness of the metal film should be sufficiently thin in order to enable the evanescent wave penetrate into the opposite surface, and thick enough to avoid undue reradiation back into the prism.

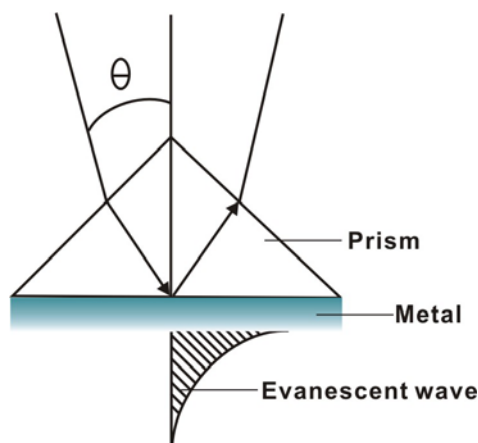


Figure 1.9. Schematic of SPR excitation by prism coupling: the Kretschmann configuration.

Resonance coupling is observed by monitoring the reflected light intensity as a function of the incident angle. If the incident angle is varied, the reflectivity curve shows a relatively narrow dip which indicates the surface plasmon resonance (Figure 1.10). The light energy is coupled to the SPR and hence the reflected light intensity reaches a minimum. Surface electromagnetic modes can only be excited at the interface of two media with opposite dielectric constants. Therefore, metals with negative dielectric constant, such as silver and gold, are used to generate surface plasmons. Ag can provide a good resonance enhancement, but is not stable against oxidation. Hence, Au is widely used because it is relatively stable. The surface charge density associated with a surface plasmon wave can be induced only by an electromagnetic mode which has a component normal to the surface. Surface plasmons can only be excited by transverse magnetic mode, i.e., p-polarized light. Transverse electric mode, i.e., s-polarized light, can not excite surface plasmons because it propagates along x-direction and has an E-field component parallel to the surface. If a thin layer ($n_{\text{layer}} > n_{\text{air}}$) is deposited onto the metal, it is equivalent to an increase of the overall effective refractive index integrated over the evanescent field of a surface plasmon mode (Figure 1.10). The net effect is a slight shift of the dispersion curve corresponding to the increase of wavevector of surface plasmons (k_{sp}) for any given energy. As a consequence, the incident angle that determines the photon wavevector along the surface plasmon propagation direction has to be slightly increased

in order to couple resonantly to the surface plasmon mode again. The critical angle is unaffected by the presence of a thin dielectric layer.

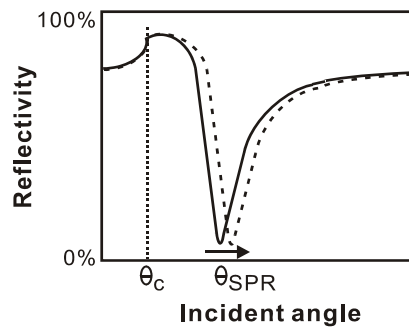


Figure 1.10. Typical SPR curves showing reflectivity versus incident angle. Adding a layer onto the metal results a shift.

Upon increasing the refractive index (n) or the thickness (d) of the dielectric layer, the resonance angle shifts toward higher angles. The angular shift $\Delta\theta$ is a function of d and the optical contrast to the surrounding medium, which is given by:

$$\Delta\theta = f(d(\varepsilon_{Layer} - \varepsilon_d)) \tag{1.2}$$

Here ε_{layer} and ε_d are the dielectric constants of the layer and the dielectric, respectively. Parameters of d and n cannot be determined independently by SPR with one angle shift only. However, if the refractive index of the material is known, the geometrical thickness can be obtained, and vice versa.

SPR measurement is carried out with a setup shown in Figure 1.11. In brief, a HeNe laser beam is mechanically chopped at a frequency of 1150 Hz and then passes through two polarizers. The second polarizer generates a plane wave with the desired polarization, whereas, the first one is used for the attenuation of the laser. The reflected beam is collected and focused onto a photodiode. The incident angle (θ) is varied by rotating the prism sample on a fine goniometer with an angle resolution of 0.001 degree. The collection lens and the detector are rotated by an angle of 2θ in order to catch the reflected light. The output of the photodiode circuit is sent to a lock-in amplifier to

demodulate the signal voltage. In this method, a curve of reflectivity versus incident angle is obtained.

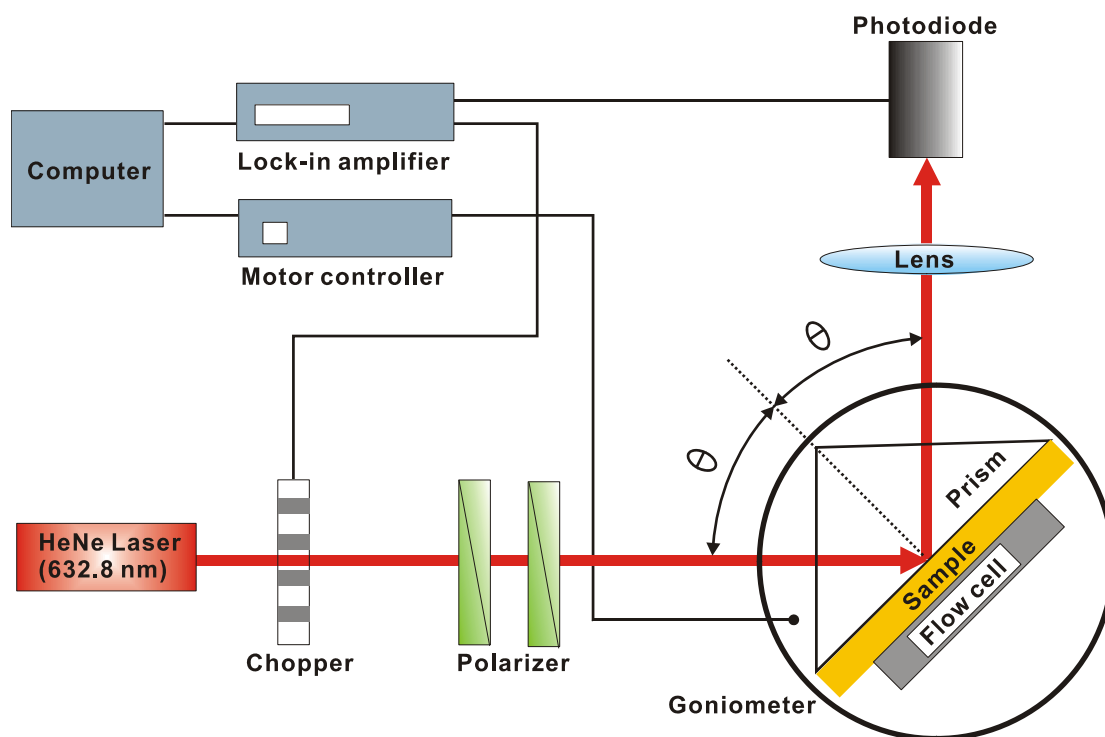


Figure 1.11. Schematic illustration of an optical waveguide spectroscopy setup.

LaSFN9 glass slides ($n = 1.844$) are used as substrates for SPR measurements. On one side Au film is evaporated with certain thickness. The other side of the glass slide is optically matched to the base of a LaSFN9 glass prism ($n = 1.844$ at $\lambda = 633$ nm) by using a refractive index oil ($n = 1.700$). This allows for the excitation of evanescent waves at the metal/dielectric interface, upon the total internal reflection of a laser beam ($\lambda = 633$ nm, power ca. 5 mW) at the prism base. The usual reflectivity scan, R versus θ , is achieved by monitoring the reflected light intensity as a function of the incident angle. If the reflected intensity (at a fixed angle near the SPR angle) is recorded as a function of time, kinetic information about interfacial changes can be monitored. Another approach to obtain kinetic information is to follow the angle shift by tracking the minimum of a reflectivity dip, which is suitable for large angle shifts.

1.4.1 Sample preparation

The samples were prepared by Stefanie, Ahl working in the group of Prof. Dr. Wolfgang, Knoll in MPIP. The whole self-assembled matrix is illustrated in Figure 1.12. Firstly 50 nm gold (99.9999%, Balzers) was deposited onto clean glass (LaSFN9 slide) substrate by thermal evaporation at a rate of 0.1 nm/s under UHV conditions ($p < 10$ mbar) in an evaporation apparatus (Edwards). Then the self-assembled monolayer (SAM) was prepared on the gold surface by incubation for 24 h in a binary mixed thiol solution of a biotinylated thiol (Biotinaminocapronacid-amidodioctyl-mercaptopropionamide) and a spacer thiol (11-Mercapto-1-undecanol, Aldrich) at a molar ratio of 1: 9 and a total concentration of 0.5 mM in absolute ethanol (Aldrich) in order to control the surface density and to minimize non-specific adsorption of target molecules. Subsequently, the streptavidin solution (1 μ M, Kem-En-Tec Diagnostics) was injected into the flow cell system in order to allow for binding to the self-assembled thiol layer at a flow rate of 10 μ L/sec. Finally, biotinylated DNA (1 μ M) were immobilized on the streptavidin layer as probe via the streptavidin/biotin binding. Hence, the target of ss-DNA-*b*-PS (0.04 μ M) with complementary DNA sequences was connected with the biotinylated DNA probe through hybridization.

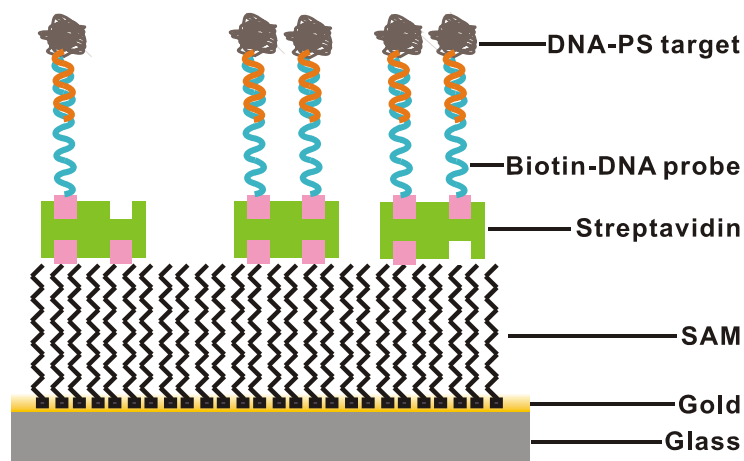


Figure 1.12. Illustration of the self-assembled matrix.

2 SYNTHESIS OF DNA BLOCK COPOLYMERS

DNA block copolymers were synthesized in the group of Andreas Herrmann by Fikri E. Alemdaroglu in MPIP Mainz in a single process using an Oligopilot DNA synthesizer (Amersham biosciences, Sweden). Two polymers, PS and PPO have been used for synthesis of DNA block copolymers. PPO has rather low glass transition temperature (T_g) at -70°C compared with T_g of PS at 100°C . Lower T_g gives polymer the advantage in dissolving in aqueous and helps micelles to reach the equilibrium state^{50 51}.

2.1 DNA-*b*-PPO

The synthesis procedure of DNA-*b*-PPO is illustrated in Figure 2.1. The synthesis starts with hydroxy-group-terminated PPOs (6800 g/mol) dissolving in dry THF. It was reacted with phosphoramidite chloride in the presence of diisopropylethylamine at RT under argon atmosphere for 3 h. Then the crude product was dried and dissolved in ethylacetate and extracted with Na_2CO_3 solution, water and brine. The solution was dried over MgSO_4 . After evaporation of the solvent the phosphoramidite-PPO derivatives were dried under high vacuum. It was then dissolved in dry dichloromethane and attached to the 5' end of an ODN (22mer, 6670 g/mol, sequence: 5'-CCTCGCTCTGCTAATCCTGTTA-3') on a solid support. Finally ss-DNA-*b*-PPO was recycled through the solid support for 25 min to achieve high coupling efficiency. After that, phosphoramidite-PPO derivatives were liberated from the solid support using concentrated ammonia for 16 h accompanied by deprotection of the bases. The solid support was removed by filtering and was then washed with ethanol/water mixture. After evaporation of the solvent the conjugate was purified, filtered and desalted.

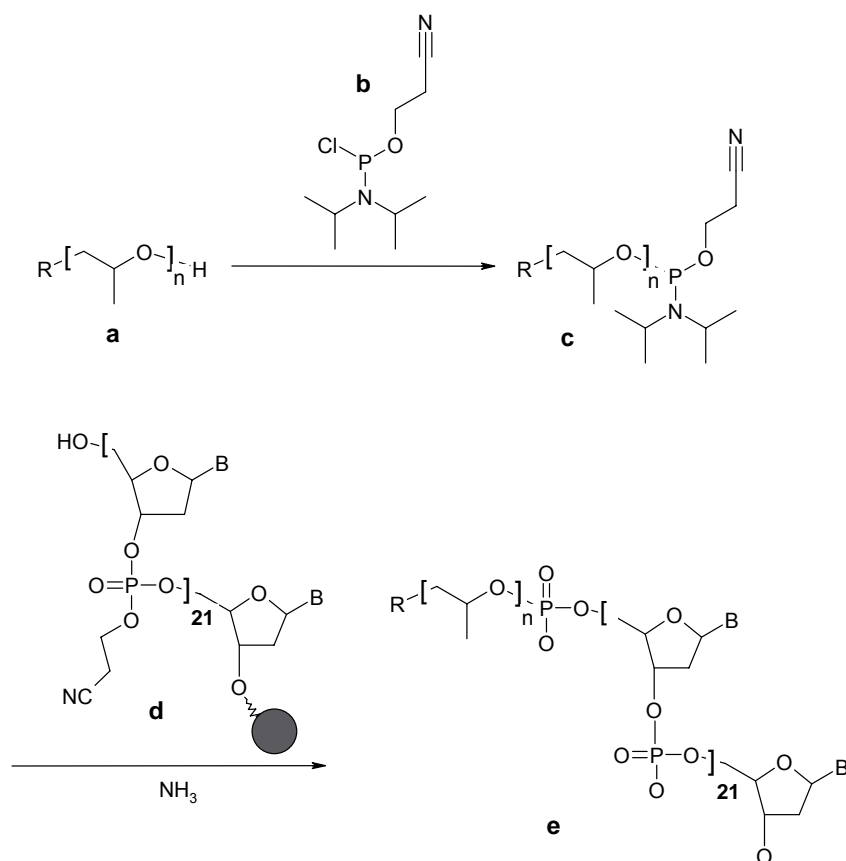


Figure 2.1. Synthesis of ss-DNA-b-PPO. **a:** hydroxy-group-terminated PPO. **b:** phosphoramidite chloride. **c:** phosphoramidite-PPO derivatives. **d:** the solid support and **e:** product of ss-DNA-b-PPO. **B:** protonated nucleobase.

2.2 DNA-b-PS

The synthesis process of the DNA-b-PS is shown in Figure 2.2. It starts from anionically polymerized amino-terminated PS polymers with molecular weights of 5500, 10000, and 56000 g/mol, respectively. They were converted into maleimido-functionalized PS using maleimido butyric acid chloride. Michael addition of functionalized PS with a 16mer ODN (5123 g/mol, sequence: 5'-TAGTTGTGATGTACAT-3') with a sulfhydryl linker at the 5' end yielded the desired amphiphilic block copolymers. The coupling of the hydrophobic PS with the hydrophilic ODN was carried out in a solvent mixture of THF and water. The products were purified by PAGE and subsequent dialysis to remove residual salts from the electrophoresis buffer.

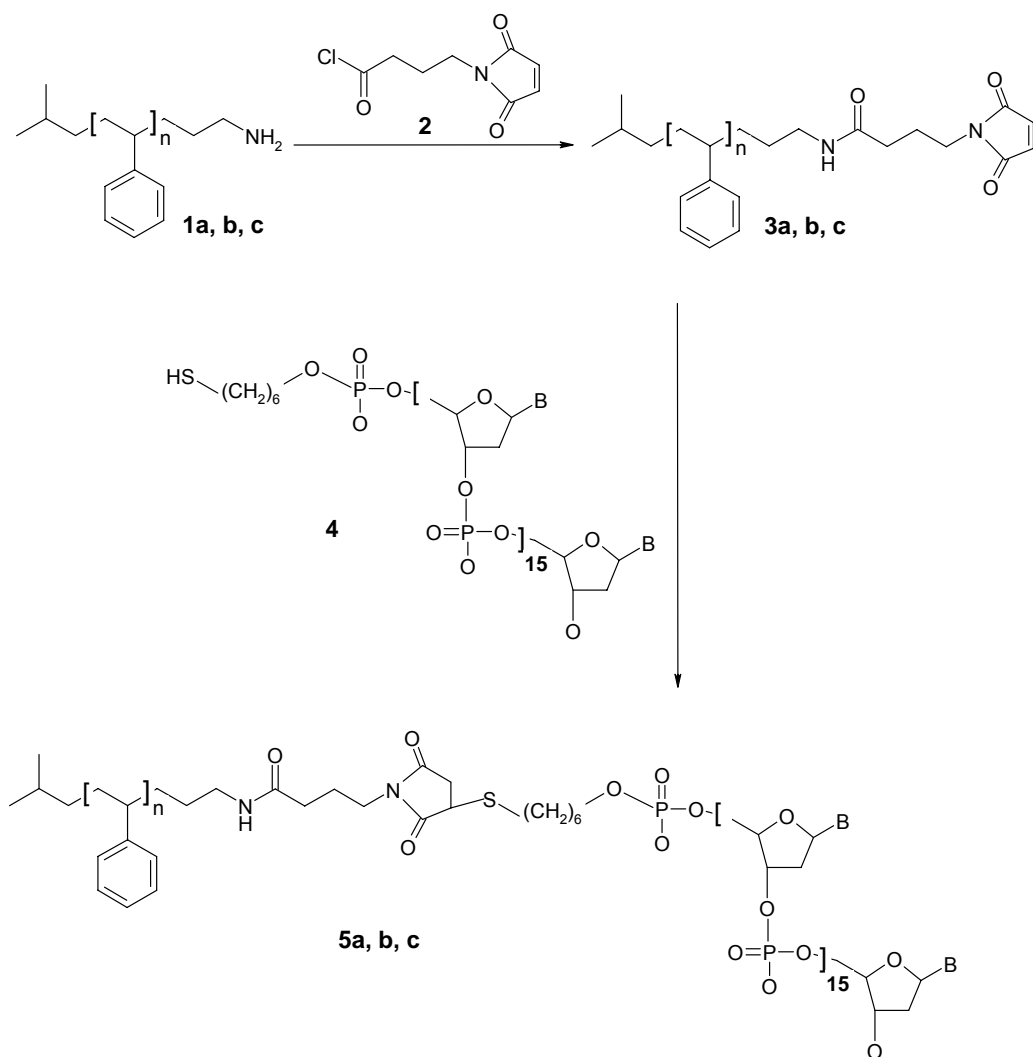


Figure 2.2. Synthesis of DNA-b-PS. **1a, b, c:** amino-terminated PS with different molecular weight (5500, 10000, and 56000 g/mol for a, b, and c, respectively). **2:** maleimido butyric acid chloride. **3a, b, c:** maleimido-functionalized PS. **4:** 16mer ODN with a sulfhydryl linker at the 5' end. **5a, b, c:** DNA-b-PS block copolymers.

3 RESULTS AND DISCUSSIONS

3.1 In-situ AFM studies in solution

The amphiphilic DNA block copolymers are dissolved in buffer. The ss-DNA can be hybridized with complementary sequences to form higher ordered structures in buffer. In order to study the structures of the DNA block copolymers, AFM measurements have been done in buffer solutions.

3.1.1 The critical micelle concentration

The CMC is the concentration of an amphiphilic component in solution at which the formation of aggregates (micelles, round rods, lamellar structures etc.) is initiated. Usually the hydrophilic part of the molecule has an affinity for polar solvents, such as water, and the hydrophobic part of the molecule has an affinity for non-polar solvents, such as CCl_4 . An amphiphilic molecule can arrange itself at the surface of the water such that the hydrophilic part interacts with the water and the hydrophobic part is held above the surface (either in the air or in a non-polar liquid). Below the CMC, they form a single layer on the liquid surface and are dispersed in solution (a in Figure 3.1). At the CMC, they organize into globular micelles (b in Figure 3.1). Micelle is an aggregate of the amphiphilic molecules dispersed in a liquid colloid. The process of forming micelles is known as micellization. Micelles are often globular in shape, but other shapes are possible, including ellipsoids, cylinders, bilayers, and vesicles. The shape of a micelle is determined not only by the molecular geometry, but also on the temperature, pH, and the type and concentration of any added salt.

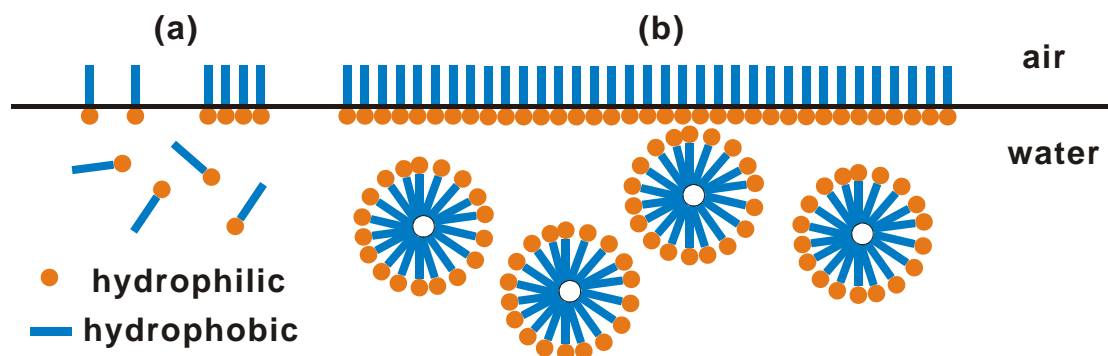


Figure 3.1. Schematic illustration on the micelles formation above CMC value at the air/water interface.

3.1.2 Below the critical micelle concentration

To obtain single molecules of DNA block copolymers on surface, the concentration below the CMC should be applied for AFM studies.

ss-DNA-*b*-PPO

From the AFM imaging, zigzag structures with an average contour length of 18 nm have been observed on mica surface at 1 ng/ μ L which is below the CMC (Figure 3.2). A single molecule of ss-DNA-*b*-PPO consists of DNA block and PPO block. Concerning the length of DNA with 22 bases as 7.48 nm and the radius of gyration for 6800 g/mol PPO in water as 1 nm, such a molecule has roughly 8.48 nm in length. The image on the left side in Figure 3.2 is zoomed from the image on the right side and 7 zigzag structures were labeled with white frames. The black lines indicate the route for estimating the contour length. The width of them has been measured to have a value between 3-5 nm. The average height of the zigzag structures was measured to be 1.02 ± 0.05 nm. The height and width of ss DNA molecules have been measured under AFM to have similar values from literatures^{27, 52, 28, 29}.

Owing to the length of such zigzag structures which is always twice as the length of the single molecules, we assume that they are dimers formed through hydrophobic interaction between PPO blocks. The model in Figure 3.2 shows one example of dimer from ss-DNA-*b*-PPO. In addition to the

dimers, there are also singly separated molecules that did not form dimers. From the AFM images in Figure 3.2, the single molecules exhibit either linear shape shorter than dimers or globular shape due to the pairing of some bases in one molecule.

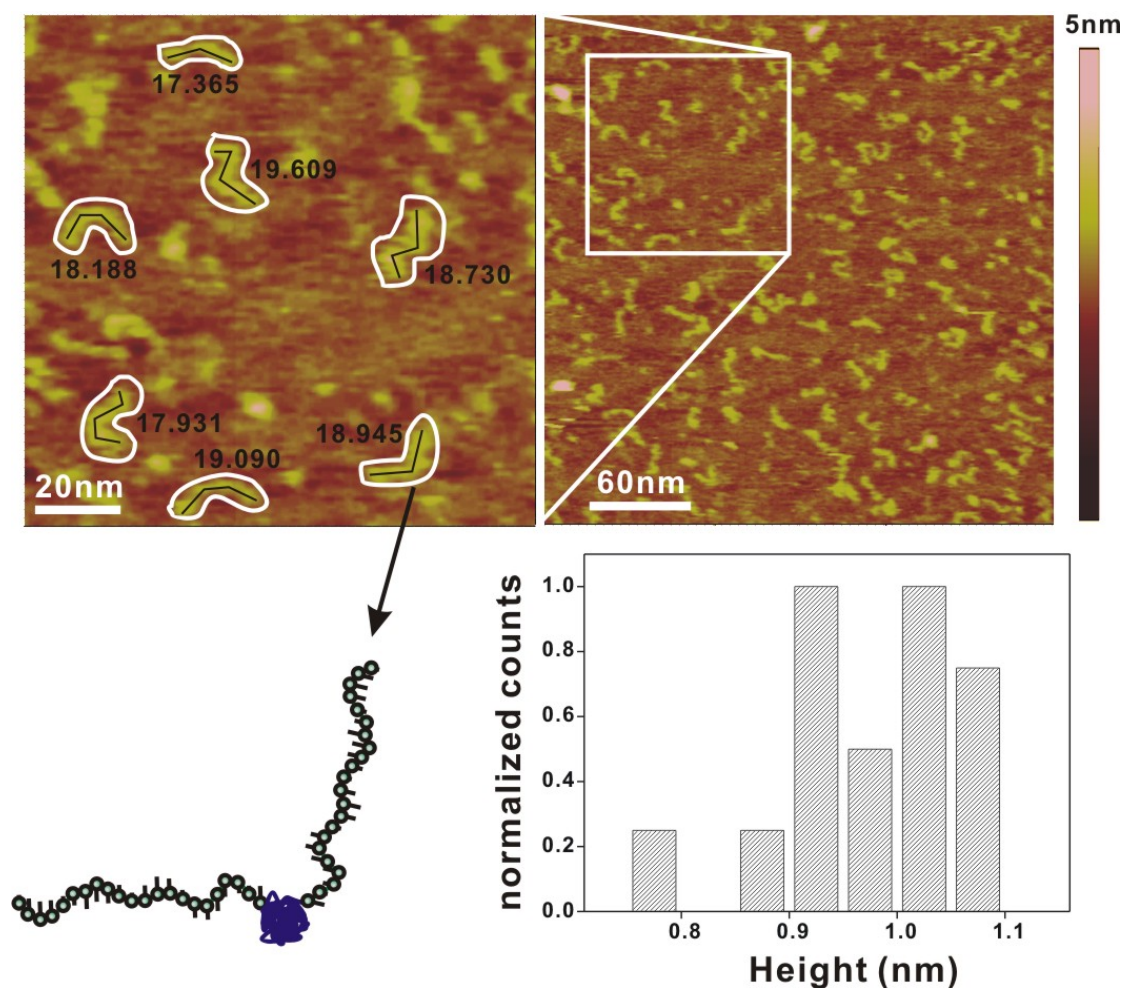


Figure 3.2. **Top:** Tapping mode height images (**left:** 120X120 nm²; **right:** 298X298 nm²) of ss-DNA-b-PPO on mica in buffer solution. The concentration was 1 ng/ μ L and Z range is 5 nm for both images. Left image was zoomed from the white box in right one. White boxes in left image indicate dimers from ss-DNA-b-PPO. Black lines are the route for measuring contour length and the numbers are given for each one. **Bottom:** **Left** is a Model of a ss-DNA-b-PPO dimer with PPO attached together through hydrophobic interaction and **right** is the histogram of height distribution.

ds-DNA-*b*-PPO

ss-DNA-*b*-PPO can be hybridized with complementary sequenced ODNs in order to achieve ds-DNA-*b*-PPO. Will the shape and size of the hybridized DNA block copolymers change? With this question, ds-DNA-*b*-PPO was prepared by attaching 5'-TAACAGGATTAGCAGAGCGAGG-3' to the ss-DNA-*b*-PPO.

Figure 3.3 shows stiffer structure formed on mica surface from ds-DNA-*b*-PPO at 10 ng/ μ L which is below the CMC. The AFM image shows two layers of structures: a top layer with brighter rods and a sub layer with darker structures. The heights of these two layers were measured by section analysis and the histogram shows two peaks at approximately 1 nm and 2 nm, respectively. They are two layers of molecules.

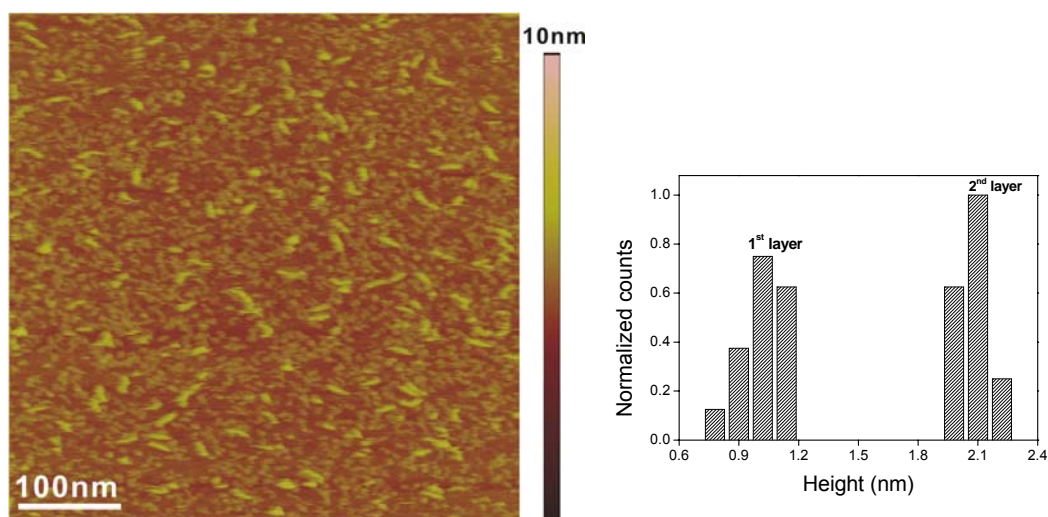


Figure 3.3. *Left:* Tapping mode height image (500X500 nm²; Z range 10 nm) of ds-DNA-*b*-PPO on mica in aqueous. The concentration was 10 ng/ μ L. *Right:* The histogram of the height distribution of the two layers appeared from the top AFM image.

Figure 3.4 shows the smaller scaled AFM images on the same sample. The contour length of the rod like structures has been measured to be around 20 nm, which is also twice as the length for single molecules. This indicates that dimers can form between ds-DNA-*b*-PPOs as well. The dimers exhibited more extended than ss-DNA-*b*-PPO dimers due to the different persistence length

in water (approximate 50 nm for ds-DNA and a few nanometers for ss-DNA). The model below the AFM pictures shows one dimer of ds-DNA-*b*-PPO molecules with polymers stay together. In addition, there are also single molecules that did not form dimers. They are shorter than dimer and are linear or globular. It was reported that dsDNA with 50bp did not show a consistent molecular conformation and both globular and rod-like shapes were seen²⁹. In Hansma's result, homogeneous fields of rod-like structures either straight or slightly bent formed when ds-DNA contains 100bp.

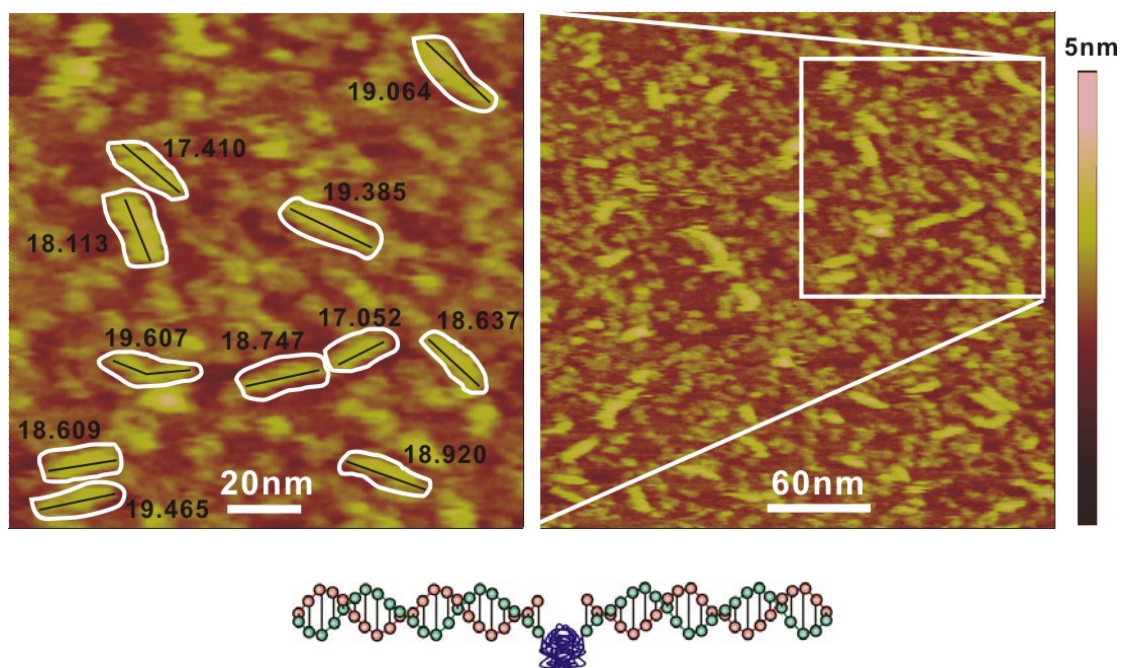


Figure 3.4. Top: Tapping mode height images (**left:** 140X140 nm²; **right:** 300X300 nm²) from same experiment on different position. Left image was zoomed from the white box in right one. White boxes in left image indicate dimers from ds-DNA-*b*-PPO. Black lines are the route for measuring contour length. The concentration was 10 ng/μL and Z range is 5 nm for both images. **Bottom:** Model of a ds-DNA-*b*-PPO dimer with PPO attached together through hydrophobic interaction.

Further increasing the concentration to 25 ng/μL led to a dens rod like structure that is shown in Figure 3.5. There was no micelle observed, which indicates that the CMC value for ds-DNA-*b*-PPO is still not reached. The average height of the rods was measured to be 2.15 ± 0.05 nm. This indicates that there is a sublayer beneath this layer. Due to the density of the toplayer,

the sublayer was not observed. From the histogram on length analysis on these rods, two peaks were observed at ≈ 11 nm and ≈ 20 nm. These two peaks are owing to the formation of single molecule and the dimer of ds-DNA-*b*-PPO.

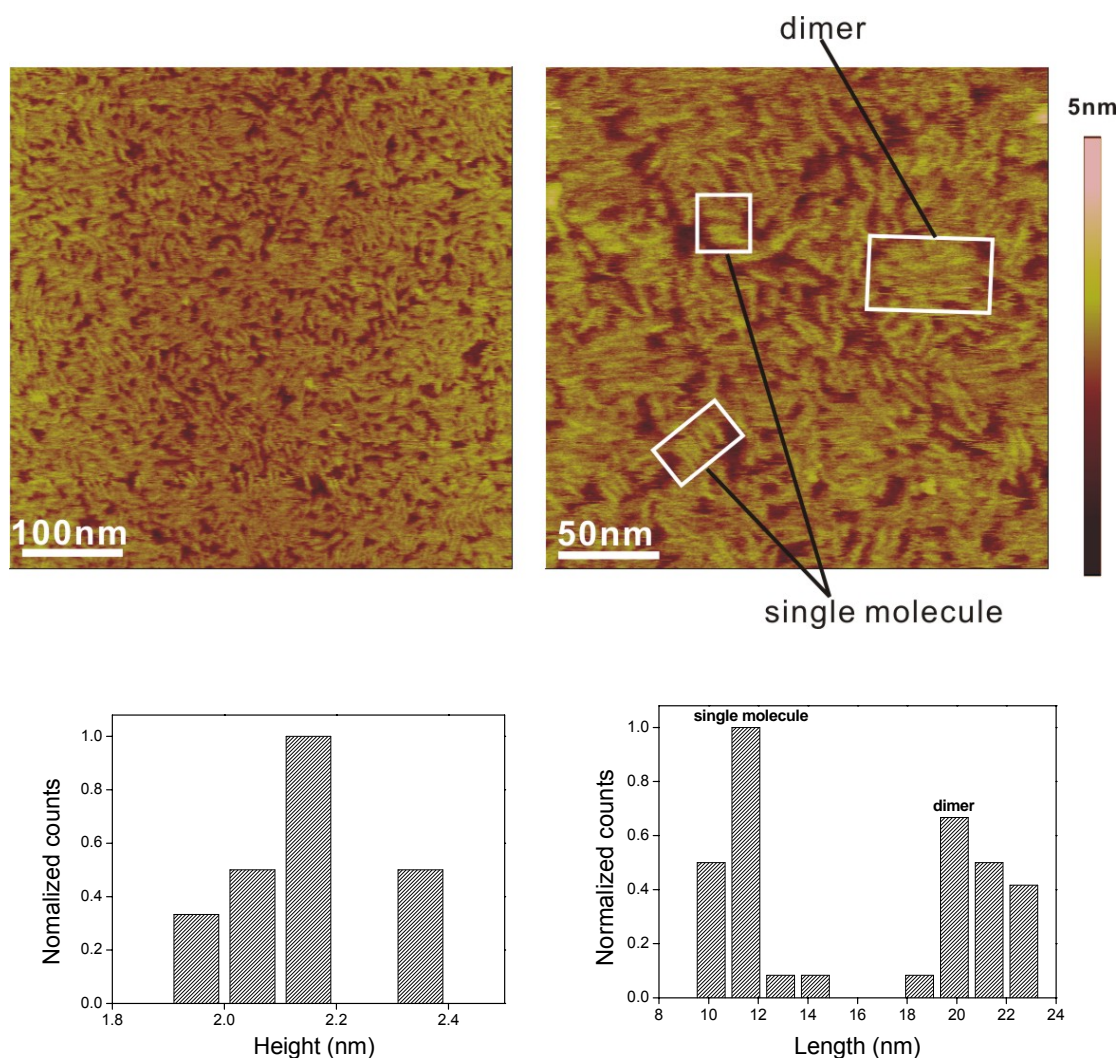


Figure 3.5. *Top:* Tapping mode height images (*left:* 500X500 nm²; *right:* 250X250 nm²) of ds-DNA-*b*-PPO on mica in buffer solution. The concentration was 25 ng/ μ L and Z range is 5 nm for both images. *Bottom:* Histogram on height and length of the rod like structure.

3.1.3 Above the critical micelle concentration

When the concentration reaches CMC, DNA-*b*-PPOs may form micelles in buffer solution. The existence of micelle structures was measured by AFM, DLS and FCS.

ss-DNA-*b*-PPO micelles

The globular micelles were observed (Figure 3.6) when the concentration for ss-DNA-*b*-PPO was increased to 5 ng/μL which is the CMC value. The micelles are not always uniform but aggregate in some cases. For measuring the height of micelles, obvious aggregates were not included into the analysis. The average height of the micelles was measured to be 5.16 ± 1.79 nm which is shown in the histogram. The density of the micelles is $38/\mu\text{m}^2$.

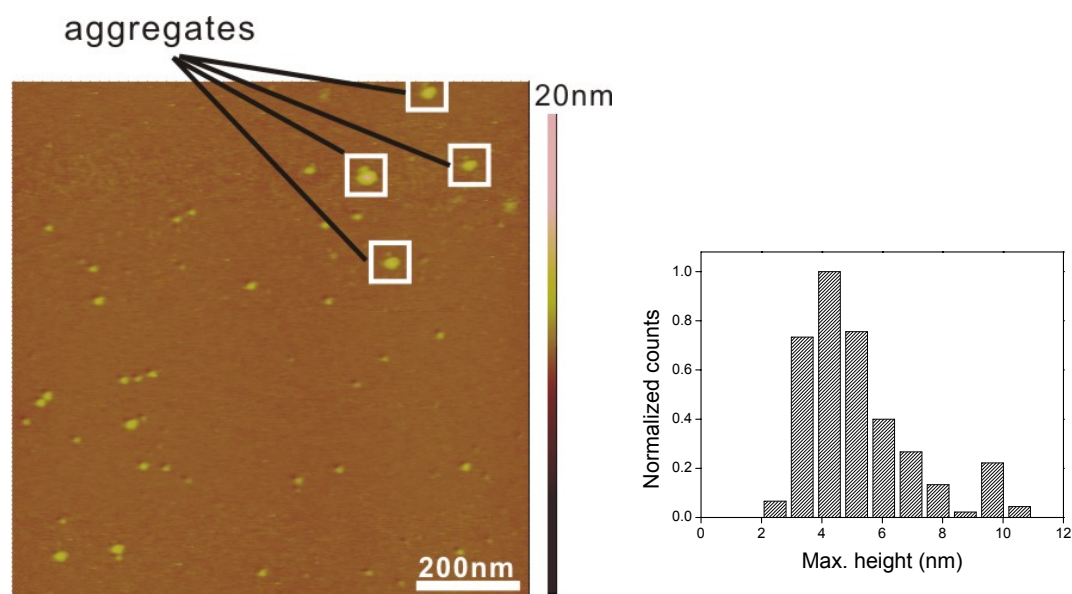


Figure 3.6. *Left:* Tapping mode height image ($1 \times 1 \mu\text{m}^2$) of micelles formed from ss-DNA-*b*-PPO on mica in buffer solution. The concentration was 5 ng/μL and Z range is 20 nm. *Right:* The histogram of the maximum height of micelles.

Further increase of the concentration to 25 ng/μL resulted in a denser micelle structure (Figure 3.7). Larger aggregates were observed as well. From the height analysis, the average value of the maximum height is 4.39 ± 0.15 nm. The density of the micelles is $162.5/\mu\text{m}^2$.

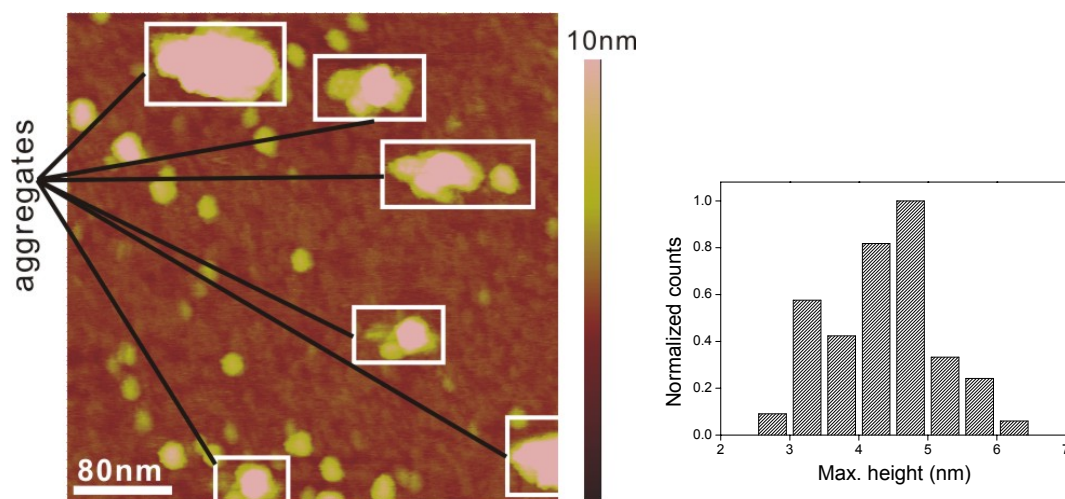


Figure 3.7. Left: Tapping mode height image ($400 \times 400 \text{ nm}^2$) of micelles formed from ss-DNA-b-PPO on mica in buffer solution. The concentration was $25 \text{ ng}/\mu\text{L}$ and Z range is 10 nm . **Right:** The histogram of the maximum height of micelles.

The amphiphilic ss-DNA-b-PPO molecules formed even denser globular micelles at $50 \text{ ng}/\mu\text{L}$ on mica surface. Figure 3.8 shows AFM image and histograms of the maximum height for micelles. In the AFM topography, globular micelles were observed. They were either singly separated or aggregated to larger aggregates. The height distribution in histogram shows an average value at $5.26 \pm 1.63 \text{ nm}$. The density of the micelles is $180.6/\mu\text{m}^2$.

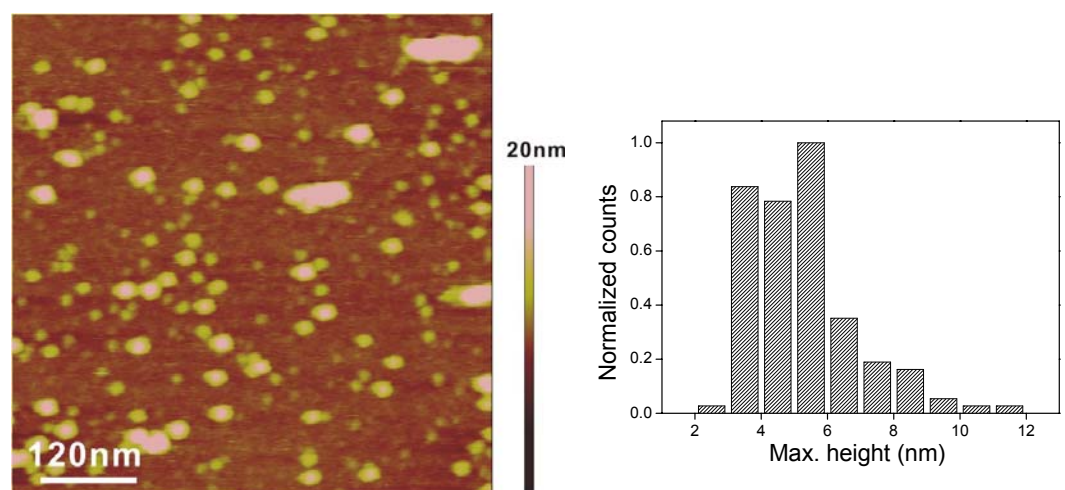


Figure 3.8. Left: Tapping mode height image ($600 \times 600 \text{ nm}^2$) of micelles formed from ss-DNA-b-PPO on mica in buffer solution. The concentration was $50 \text{ ng}/\mu\text{L}$ and Z range is 20 nm . **Right:** The histogram of maximum height of micelles.

On mica surface, the micelles could be deformed by combining with substrate and the pressing of AFM tip during imaging process. In our experiments, soft tapping imaging was applied and therefore the micelles are not deformed by tip. From DLS in solution, the micelles of ss-DNA-*b*-PPO exhibited a diameter of 11.3 ± 2 nm (Figure 3.9), which is almost twice of the diameter observed from AFM measurements. This indicates that the micelles are deformed by adsorptions between mica and DNA during AFM imaging process on mica surface. The model of the micelles from ss-DNA-*b*-PPO on mica surface is shown in Figure 3.10. Hence, the observed maximum height is less than the theoretical diameter of micelles. In addition, single molecules and dimers may exist as shown in the model.

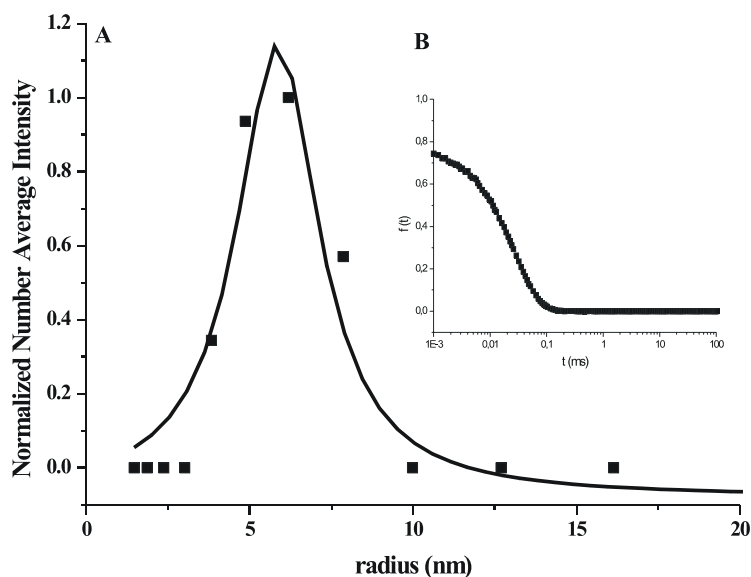


Figure 3.9. Dynamic light scattering data of micelles of ss-DNA-*b*-PPO. **A)** Lorentzian size distribution. **B)** Correlation function.

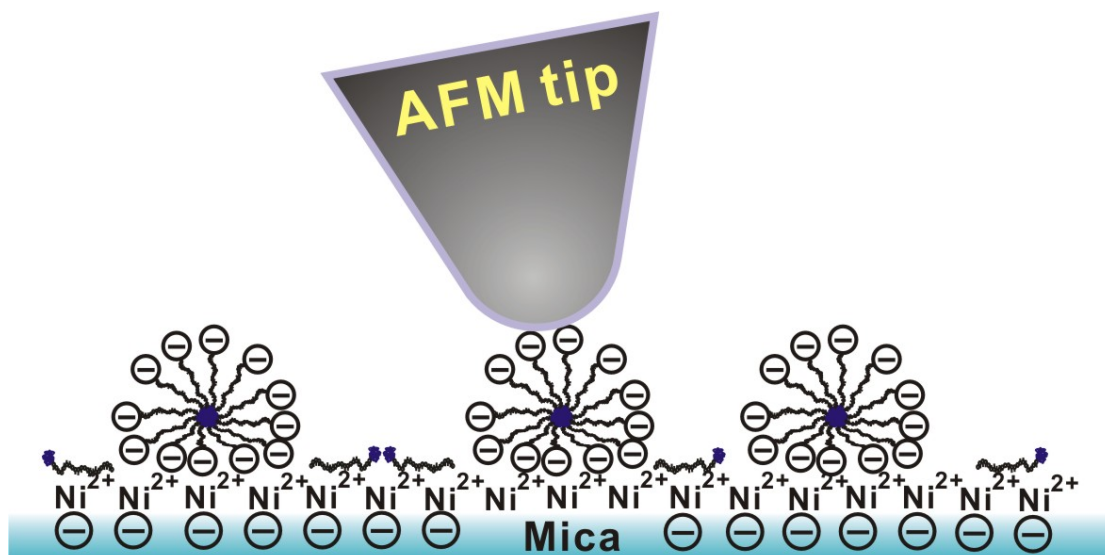


Figure 3.10. Model of ss-DNA-*b*-PPO micelles (polymer in the core and DNA in the shell) adsorbed on mica surface. Ni²⁺ in buffer solution bind negative end of DNA to negative mica surface. The AFM tip is not deforming the micelle under soft tapping imaging.

ds-DNA-*b*-PPO micelles

Micelles of ss-DNA-*b*-PPO formed when reaching the concentration of CMC which is 5 ng/μL. To investigate whether the hybridization from ss-DNA-*b*-PPO to ds-DNA-*b*-PPO will change the size of micelles, AFM investigations on ds-DNA-*b*-PPO was also done on mica surface in buffer.

Globular micelles were also observed for ds-DNA-*b*-PPO at 100 ng/μL on mica surface. Figure 3.11 shows AFM image and histogram of the maximum height for micelles, respectively. The micelles were either singly separated or aggregated. The histogram shows an average value of 5.81 ± 0.26 nm from measured maximum height. The height of the micelles is close to that of ss-DNA-*b*-PPO. This is verified by FCS, which is discussed in detail in the following chapter. The density of the micelles is $10.0/\mu\text{m}^2$.

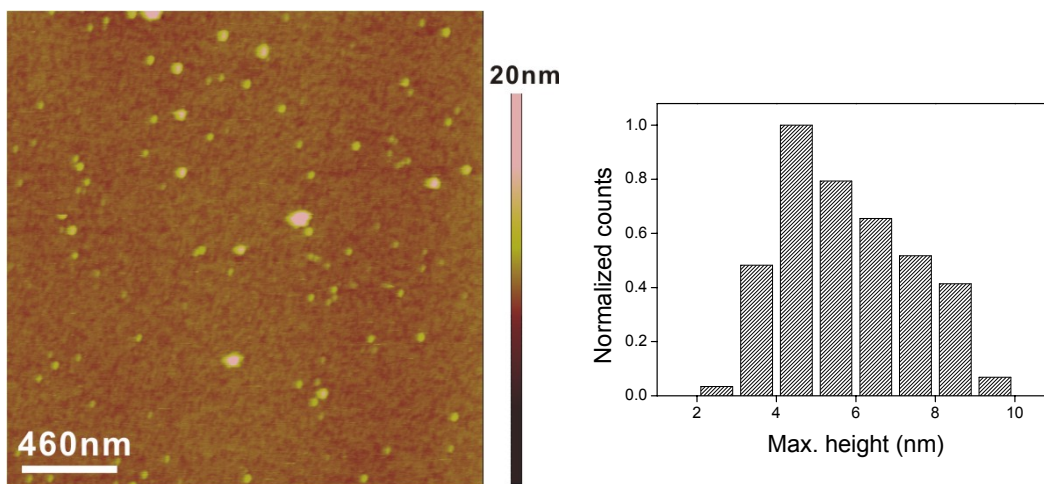


Figure 3.11. *Left:* Tapping mode height image ($2.3 \times 2.3 \mu\text{m}^2$) of micelles formed from ds-DNA-*b*-PPO on mica in buffer solution. The concentration was $100 \text{ ng}/\mu\text{L}$ and Z range is 20 nm. *Right:* The histogram of maximum height of micelles.

Globular micelles were observed from AFM measurement under much higher concentration for ds-DNA-*b*-PPO, which indicates that the CMC value for ds-DNA-*b*-PPO is much higher than the CMC for ss-DNA-*b*-PPO. Figure 3.12 shows the structures of ss- and ds-DNA-*b*-PPO versus concentration of them. For the ss-DNA-*b*-PPO, micelles appeared when the concentration reached 5 ng/mL. Micelles of ds-DNA-*b*-PPO were observed only when the concentration reached $100 \text{ ng}/\mu\text{L}$. Below those values, only single molecules and dimers were observed. Therefore we believe that the CMC for ss-DNA-*b*-PPO is $5 \text{ ng}/\mu\text{L}$ and for ds-DNA-*b*-PPO is $100 \text{ ng}/\mu\text{L}$.

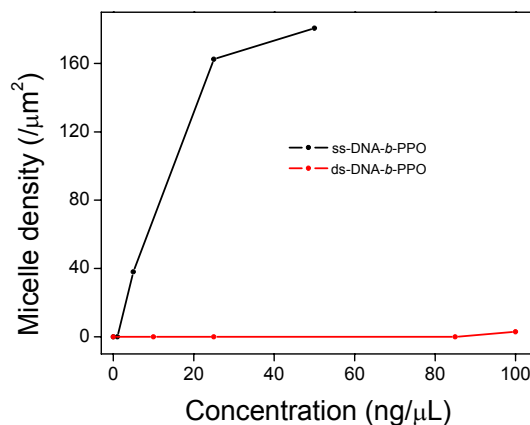


Figure 3.12. Diagram of micelle density versus concentration for both ss- and ds-DNA-*b*-PPO.

The value of CMC can also be determined from breaks in the surface tension, electrical conductivity, and dynamic light scattering curves. Fluorescence based methods have also been used for the CMC. Particularly, using pyrene as fluorescence probe became important because of the high sensitivity^{24, 53}. The fluorescence probes will exist mainly in solution below the CMC and are incorporated into the micelle above the CMC. Hence, the environmentally sensitive fluorescence probes will exhibit a break point when the concentration reaches CMC. The CMC for ss-DNA-*b*-PPO has been determined by this method to be 5 ng/μL which is consistent with AFM result. However, for ds-DNA-*b*-PPO was the CMC invisible due to the lack of materials. It has been reported that pyrene probes are not completely incorporated into the micelle if the volume of micelles is insufficient to solubilize pyrene⁵⁴. Therefore, it was difficult to find the break point for ds-DNA-*b*-PPO at the available highest concentration.

The size of the micelles was not changed by hybridization from ss- to ds-DNA block copolymers. This is good for using the micelles as template for further modification.

FCS on ss- and ds-micelles

The translational diffusion coefficients D were calculated from the mean diffusion times. As the diffusion coefficient D is related to the frictional coefficient f of the hydrated micelles, the shape information of the immobilized DNA block copolymer aggregates could be used to calculate the radius for the spherical micelles from the FCS diffusion data (equation (1.5)-(1.7)). In Figure 3.13 the autocorrelation functions of the ss-DNA-*b*-PPO and the ds-DNA-*b*-PPO are shown with diffusion times for ss-DNA-*b*-PPO micelles $\tau_{D,ss}=1.93$ ms and for ds-DNA-*b*-PPO micelles $\tau_{D,ds}=1.82$ ms respectively with $\eta = 0.01 \text{ g cm}^{-1} \text{ s}^{-1}$,

$$kT = 1.38 \times 10^{-16} \text{ g cm}^2 \text{ s}^{-2} \text{ K}^{-1} 293 \text{ K} ,$$

$$D = 2.8 \times 10^{-6} \text{ cm}^2 \text{ s}^{-1} ,$$

$$\tau_D = 0.262 \times 10^{-3} \text{ s}.$$

A mean radius of 5.6 ± 0.5 nm was found for the ss-DNA-*b*-PPO micelles. The radius of the ds-DNA-*b*-PPO micelles was 5.3 ± 0.5 nm. Both have a diameter around 11 nm which is in good agreement with the DLS (11.3 ± 2 nm). The values from FCS measurement in solution proved that the immobilization of the micelles in AFM investigations resulted in flattened micelles owing to the interaction with the surface (Figure 3.10).

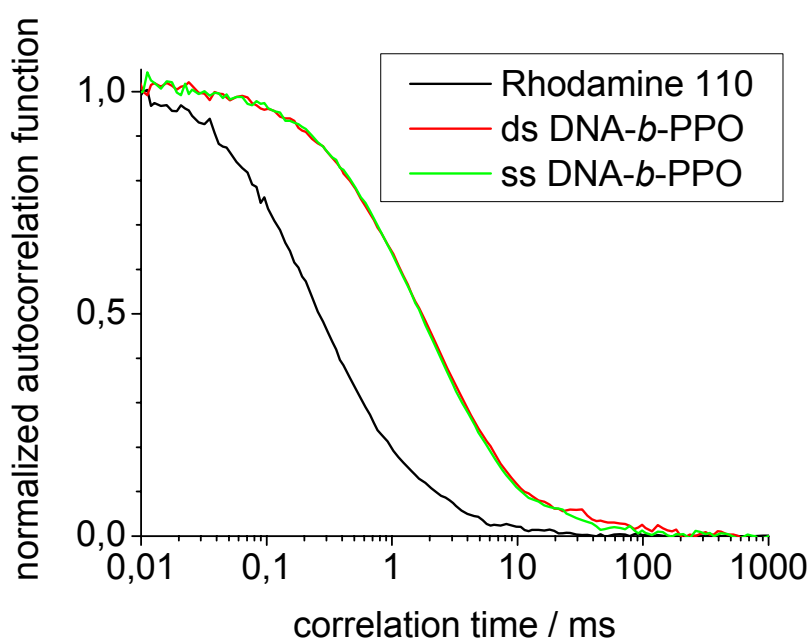


Figure 3.13. Normalized autocorrelation functions of the DNA-*b*-PPO micelles in buffer solutions with an ss DNA corona (green curve), and with a ds DNA shell (red curve). As a reference Rhodamine 110 in water (black curve) was measured.

Micelles on different substrates

Investigation of the adsorption of DNA block-copolymers on different substrates may help for better understanding the role of the interactions between molecules, solvent, and substrate on surface aggregation. Here we have studied the adsorption of ss-DNA-*b*-PPO on two different substrates: hydrophobic graphite and hydrophilic mica.

Using AFM, we find that ss-DNA-*b*-PPO micelles adsorbed on mica exhibits 4-6 nm in diameter which is half of the diameter in solution observed by DLS (11.3 ± 2 nm) and FCS (11 nm). On graphite surface, ss-DNA-*b*-PPO formed globular micelles with similar diameter observed from DLS and FCS. Figure 3.14 shows AFM image and histogram of the maximum height for micelles on graphite surface. The concentration was 25 ng/ μ L. These micelles are relatively uniform and singly separated. The average height of the micelles is 11.14 ± 0.16 nm. The density of the micelles is $93.9/\mu\text{m}^2$.

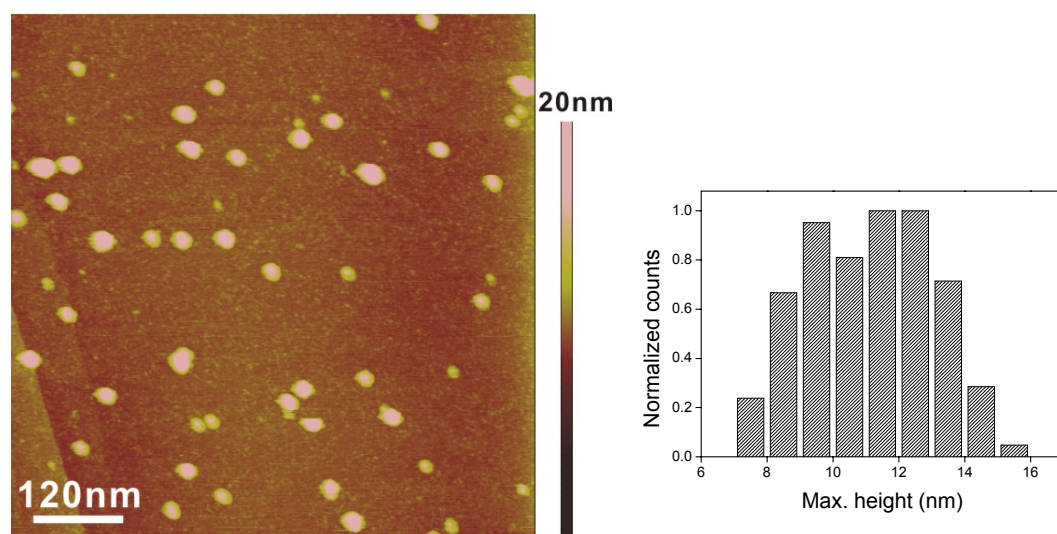


Figure 3.14. *Left:* Tapping mode height image ($700 \times 700 \text{ nm}^2$) of micelles formed from ss-DNA-*b*-PPO on HOPG in buffer solution. The concentration was 25 ng/ μ L and Z range is 20 nm. *Right:* The histogram of maximum height of micelles.

The average maximum height on graphite is roughly twice as for the micelles on mica. Probably there is a sublayer with DNA facing the solution and polymer adsorbed to graphite, which then templates the further adsorption. The micelles were adsorbed to this layer afterwards. The model is shown in Figure 3.15. Due to the sublayer as a template for the micelles sitting on hydrophobic HOPG surface, the micelles are not deformed by the interaction with the substrate as on mica surface. That is the reason why the height of the micelles on HOPG surface by AFM study was at the same range with the height measured from DLS and FCS in solution.

On the other hand, for the same concentration of 25 ng/ μL , the density of the ss-DNA-*b*-PPO micelles is 162.5/ μm^2 on mica surface and 93.9/ μm^2 on HOPG. This indicates that on HOPG surface there are more single molecules than on mica surface. This is probably because the single molecules have the same affinity with micelles to bind onto mica. On HOPG surface, the single molecules have more advantages to bind onto substrate with polymer block, which is then enable the adsorption of micelles onto the single molecules as a sublayer.

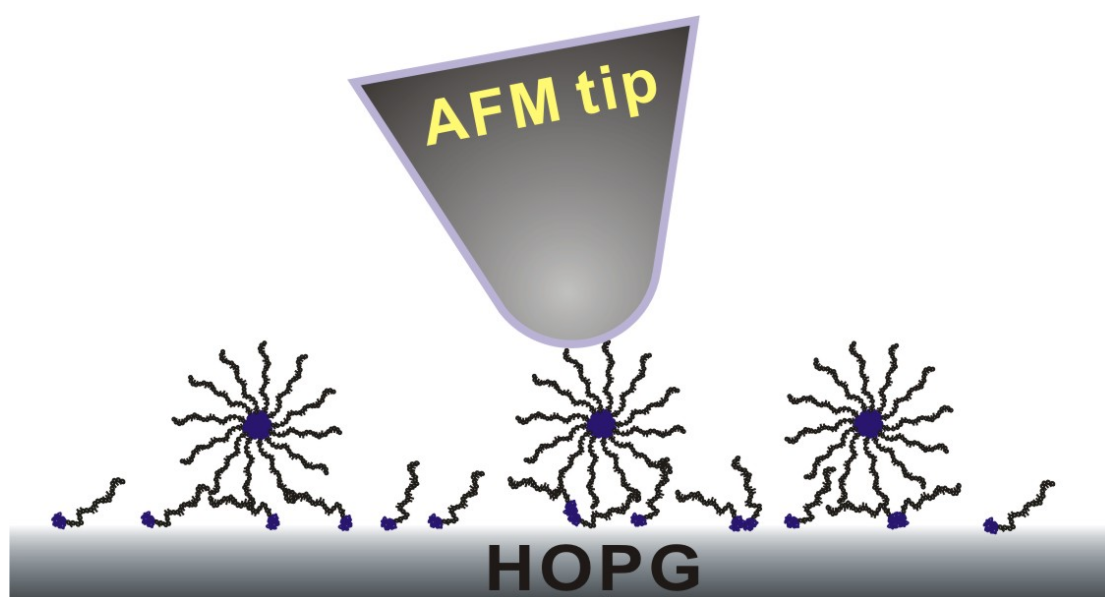


Figure 3.15. Model of ss-DNA-*b*-PPO micelles adsorbed on HOPG surface based on a sublayer of single molecules.

Grant reported their results in 1998 on a variety of ethylene oxide surfactant on graphite, hydrophilic silica, and hydrophobic silica. Globular surface micelles were the main feature observed on hydrophilic silica, and a laterally homogeneous layer was always obtained on hydrophobic silica. Their explanation was that when water has a low affinity for the substrate, the surfactant forms low-curvature aggregates which minimize the contact area between water and substrate. Graphite is hydrophobic, but the aggregation behavior is more complicated than on hydrophobic silica. They found that when the alkyl chain length is 12 or 14 carbon-unit long, the surfactant forms discontinuous hemimicelles, but that when the alkyl chain is 10 carbon-unit

long, the surfactants form a laterally flat layer. Their model was that the first layer of the longer-chain C12 and C14 forms in long ribbons of tail-to-tail structures templated by the graphite surface. Such ribbon then provides a template for the formation of a hemimicelle structure ⁵⁵.

In our experiments, PPO block was adsorbed onto graphite forming a layer with DNA pointing to water phase. The hemimicelles were not observed probably because the volume of PPO is relatively low and the length of DNA block is relatively long so that the molecule could not lie flat on graphite behaving as a template for the following hemimicelles. Our hypothesis is that when increasing the molecular weight of PPO block together with decreasing length of DNA block, hemimicelles may also form on graphite surface as shown in Figure 3.16.



Figure 3.16. Model of ss-DNA-*b*-PPO hemimicelles (polymer in the core and DNA in the shell) adsorbed on HOPG surface. A monolayer with PPO adsorbed to HOPG and DNA facing to water formed firstly to provide template for the following hemimicelles formation.

Micelles at higher salt concentration

The ss-DNA-*b*-PPO and ds-DNA-*b*-PPO micelles formed in buffer solution which contains 100 mM NaCl have been investigated by DLS and FCS to have a diameter around 11 nm in solution and around 4-6 nm on mica surface with AFM investigations. To study micelle diameter dependencies the salt concentration was varied between 100 mM and 150 mM NaCl. When we increased the salt concentration to 150 mM NaCl, however, the diameter of micelles decreased significantly under AFM measurements. Figure 3.17 shows AFM topography of micelles formed from ds-DNA-*b*-PPO with 150 mM NaCl at 100 ng/ μ L. The density of the micelles increased and the size of them decreased significantly. The histogram of the maximum height shows an

average value of 2.60 ± 0.02 nm. This was proved by diffusion NMR experiments which gave the similar result of micelle diameter with 3 nm with 150 mM NaCl.

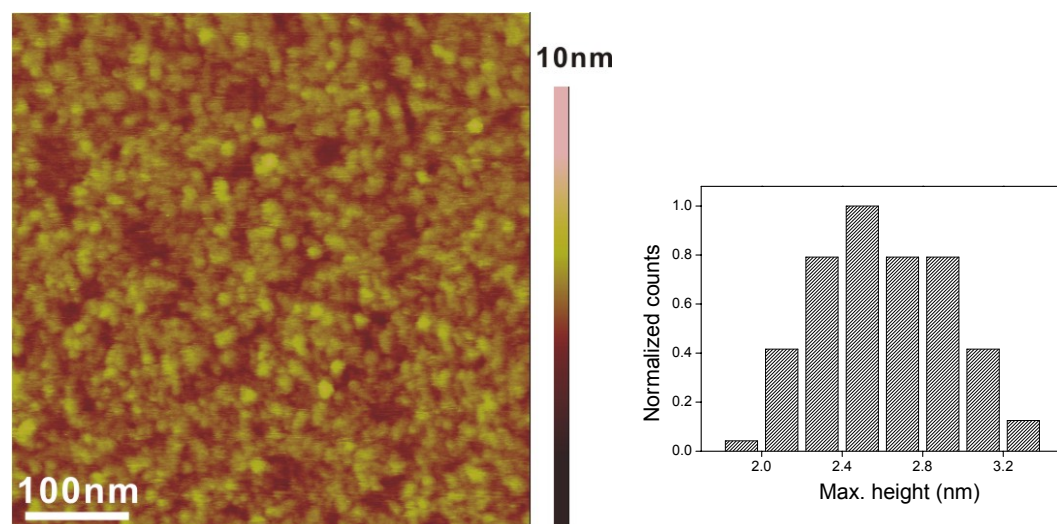


Figure 3.17. *Left:* Tapping mode height image (500×500 nm²) of micelles formed from ds-DNA-*b*-PPO on mica at higher salt concentration (150mM NaCl). The concentration was 100 ng/ μ L and Z range is 10 nm. **Right:** The histogram of maximum height of the micelles.

The influence of ionic strength on the stability of micelles has been reported⁵⁶
⁵⁷⁵⁸. From Dufresne's result, the influence of salt concentration on the stability of polyion complex micelles was studied by measuring the scattering intensity and size of micelles at different NaCl concentrations. The tendency was that the micelle size increased slightly with increasing the ionic strength below a NaCl concentration of 0.1M. However, further increasing the salt concentration led to decreases in both micellar size and light scattering intensity. From Lee's result, when the corona of micelle is weakly charged, the micelle size remains relatively constant if salt is added prior to the formation of micelles; however, the micelle size decreases with addition of salt when salt is added after micelle formation. Increasing the ionic strength causes the increase of micelle aggregation number because the salts screen the electrostatic repulsions between chains. In the case of weakly charged corona, increasing the ionic strength causes the shrink of the corona as the salt screens electrostatic repulsions within the corona. In our studies, negative DNA is the corona of the micelle of ss-DNA-*b*-PPO. Increasing the ionic

strength from 100 mM NaCl to 150 mM NaCl reduced the micelle size from 11.3 nm to 2.6 nm indicates that the negative charges in corona were screened and the “arms” of micelles can be packed closer.

Micelles before and after organic reaction in the shell

The micelles of ss-DNA-*b*-PPO with hydrophobic polymer in the core and DNA in corona may act as a 3-dimensional template in DNA-templated organic reactions. The ss-DNA of the corona can be hybridized with ODNs which are equipped with different reactants. Depending on the functionalization of either the 5' or 3' ends, various organic reactions may be performed specifically on the surface of the micelles (5' end) or at the hydrophobic/hydrophilic interface (3' end).

We have used micelles of ss-DNA-*b*-PPO as template and hybridized the ss-DNA with ODNs which were modified with -COOH and -NH₂ at 3' end. Figure 3.18 shows the schematic illustration of ss-DNA-*b*-PPO micelle templated organic reaction on micelle surface. Upon the organic reaction with EDC and NHS plus complementary DNA, amide bond formed at the corona of ds-DNA-*b*-PPO (Equation 3.1).

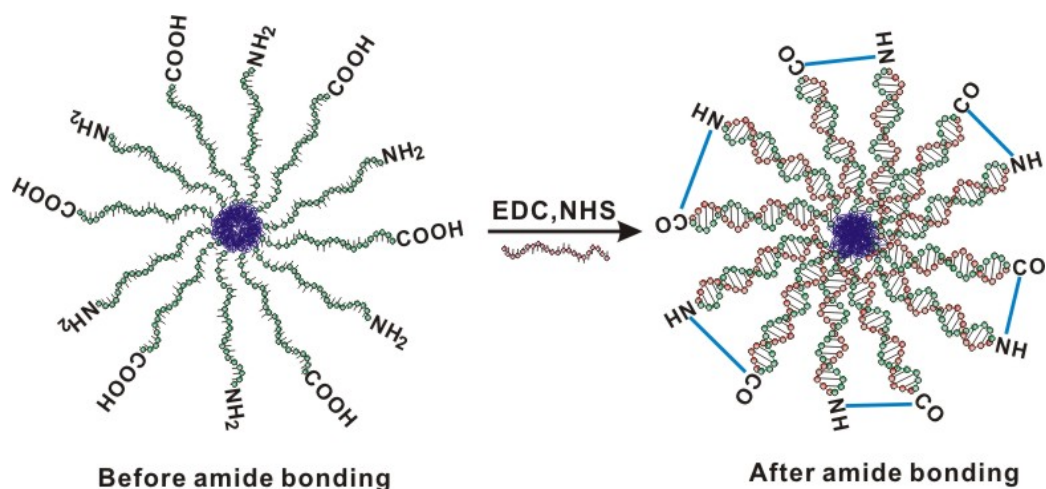
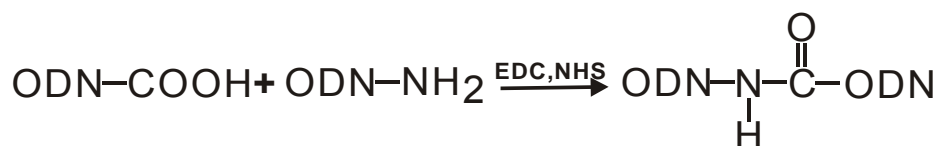


Figure 3.18. Schematic illustration of ss-DNA-*b*-PPO micelle templated organic reaction on the surface of micelle. EDC=1-ethyl-3-(3-dimethylaminopropyl) carbodiimide, NHS=N-hydroxysuccinimide.



Equation 3.1. DNA-templated reaction carried out on the surface of the DNA block-copolymer micelles. EDC=1-ethyl-3-(3-dimethylaminopropyl) carbodiimide, NHS=N-hydroxysuccinimide.

The micelles before and after amide bond formation were visualized by AFM. Figure 3.19 shows the AFM images of the micelles formed before (A) and after (B) amide bond formation, respectively. The concentration for both conditions was 100 ng/ μ L. The average height of the micelles was calculated to be 10.17 ± 0.13 nm before and 10.60 ± 0.17 nm after amide bond formation. C and D in Figure 3.19 show the histogram of height distribution of micelles before and after amide bond formation determined from more than 100 micelles obtained from 5 AFM images, respectively. The diameter of the micelles before and after chemical reaction was different because different AFM tips were used in each measurement. The SEM has been applied to check the tip radius after both AFM measurements. The result shows that the tip radius was 26 nm and 18 nm for the measurement before and after the chemical reaction, respectively. This proves that the tip radius only influence the radius but not the height of the micelle structures.

There are no significant changes in the height distribution of the histogram upon the chemical reaction, which indicates that the amide bond formation does not influence the structural properties of the micelles. The height of the micelles upon chemical reaction (10 -11 nm) is consistent with the diameter investigated from DLS (11 nm) and FCS (11 nm), which is larger than the height of ss-DNA-*b*-PPO micelles on mica surface (4-6 nm). Probably the chemical modification on surface of the micelles reduced the adsorption of the micelles with mica similar to the situation of combining the ss-DNA-*b*-PPO micelles with HOPG surface.

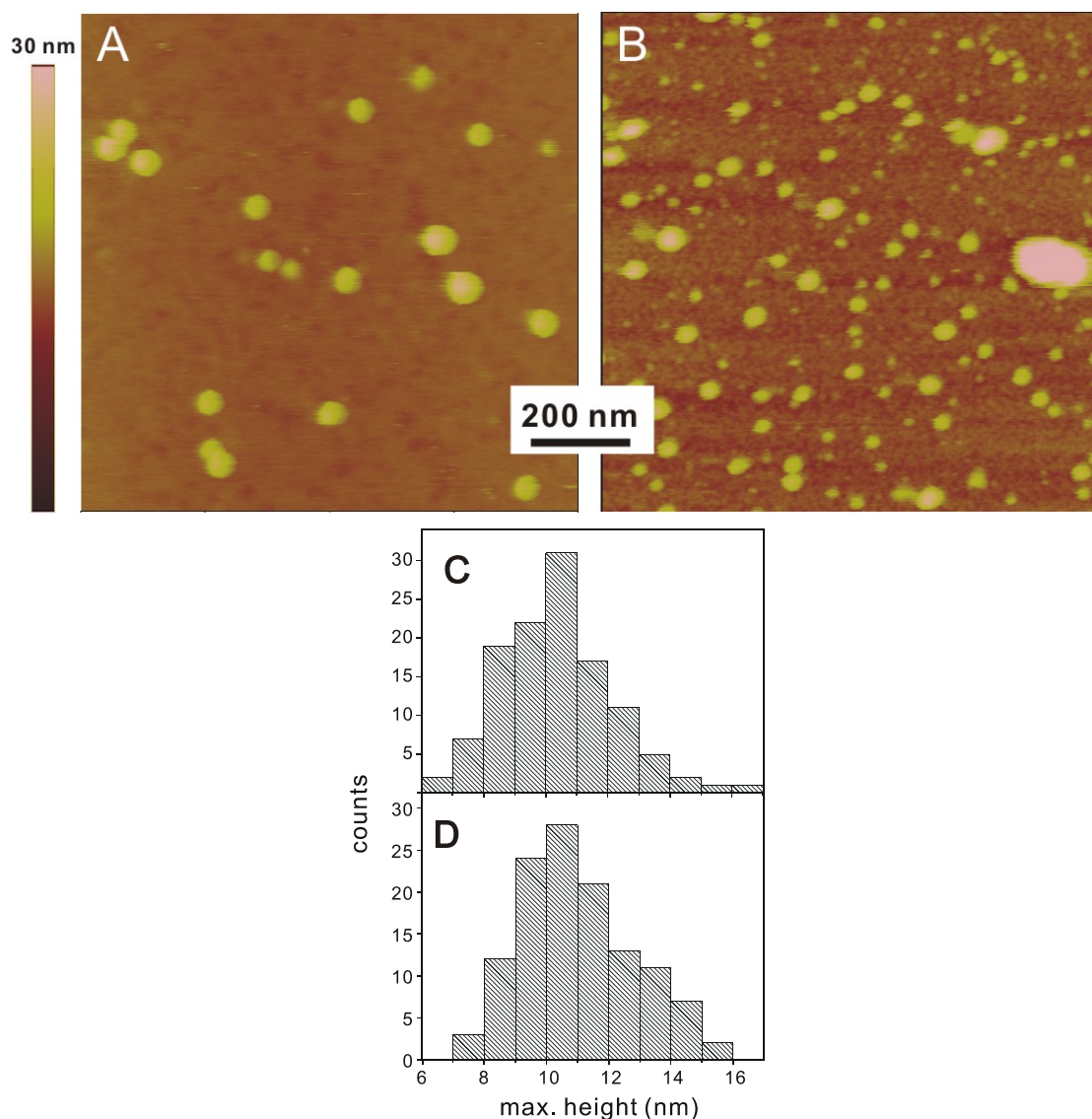


Figure 3.19. Top: Tapping mode height images of micelles before (**A**: $1 \times 1 \mu\text{m}^2$) and after (**B**: $1 \times 1 \mu\text{m}^2$) amide bond formation on mica in buffer solution. The concentration was $100 \text{ ng}/\mu\text{L}$ and Z range is 30 nm for both images. **Bottom:** The histograms of maximum height for micelles before (**C**) and after (**D**) amide bond formation.

3.1.4 ss-DNA-*b*-PS

Similar to ss-DNA-*b*-PPO, the single molecules and the micelles from ss-DNA-*b*-PS (16mer DNA, 5'-TAGTTGTGATGTACAT-3'; 50000 g/mol PS) have also been observed by AFM studies in buffer (Figure 3.20). They formed single molecules at a concentration of $2 \text{ ng}/\mu\text{L}$ (left image). By increasing the concentration slightly to $5 \text{ ng}/\mu\text{L}$, globular micelles with an average height around 11 nm formed on mica substrate (right one). Here the height of the

micelles is larger than those from ss-DNA-*b*-PPO because the Mw of PS (50000 g/mol) is much higher than that of PPO (6800 g/mol).

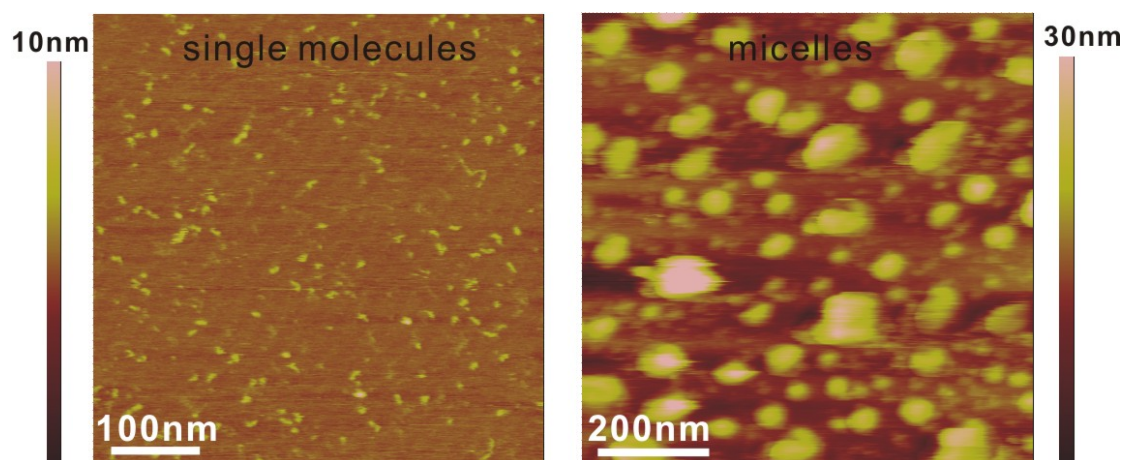


Figure 3.20. Tapping mode height images of single molecule (**left**; $525 \times 525 \mu\text{m}^2$; Z range 10 nm) and micelles (**right**, $815 \times 815 \mu\text{m}^2$; Z range 30 nm) formed from ss-DNA-*b*-PS.

3.1.5 Long templated molecules

In order to achieve highly ordered architecture based on DNA-*b*-PPO molecules, long ss-DNA template back bone have been prepared. For example, when giving a ss-DNA template with 110 bases which are 5 times repeated and each repeat unit is complementary to the ODN in ss-DNA-*b*-PPO, a molecule of DNA-*b*-PPO-T110 can be synthesized by hybridization the template with the DNA-*b*-PPO (Figure 3.21). The hybridization was carried out by dissolving ss-DNA-*b*-PPO diblock copolymer and the long ss-DNA templates in buffer by using a Biometra PCR thermocycler (Biometra GmbH, Germany). The mixture was heated to 95°C and was slowly cooled to room temperature over 3 days (1 degree per hour).

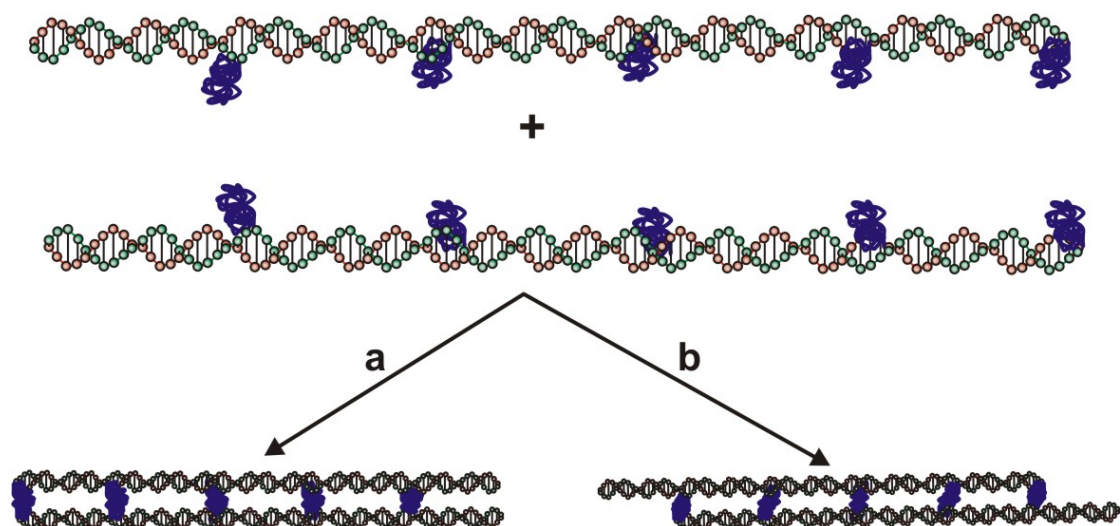


Figure 3.22. Possible structure of pairs formed from 2 molecules of DNA-*b*-PPO-T110 through hydrophobic interaction between PPO groups. Upon different binding positions, partially paired structures (b) and fully paired (a) structures are shown.

From the AFM investigation on DNA-*b*-PPO-T110 with a concentration of 37.5 ng/ μ L, pairs of molecules exist as rods or slightly bent rods were observed. Figure 3.25 shows AFM height images of rod like structure from DNA-*b*-PPO-T110 molecules on mica surface. The two molecules in one pair are sometimes parallel which indicates that the 5 PPOs are completely combined together. In addition to pairs, single molecules were also observed. The average height and length of the rod structures were measured to be 1.94 ± 0.01 nm and 37.15 ± 0.18 nm, respectively. These values are consistent to the theoretical value (37.4 nm in length and 2 nm in height) for one molecule.

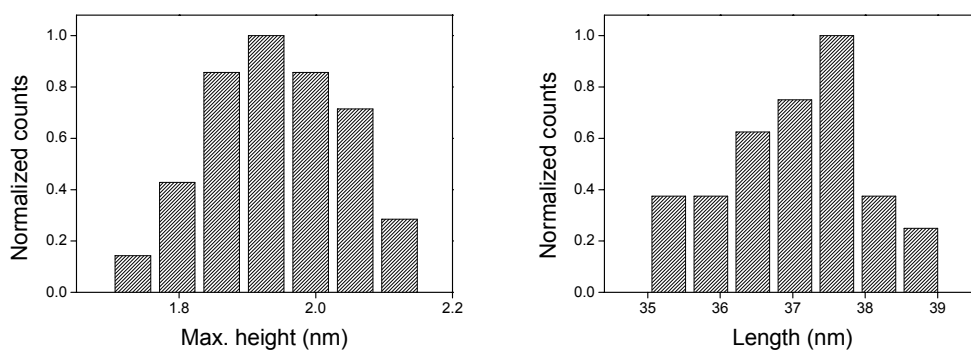
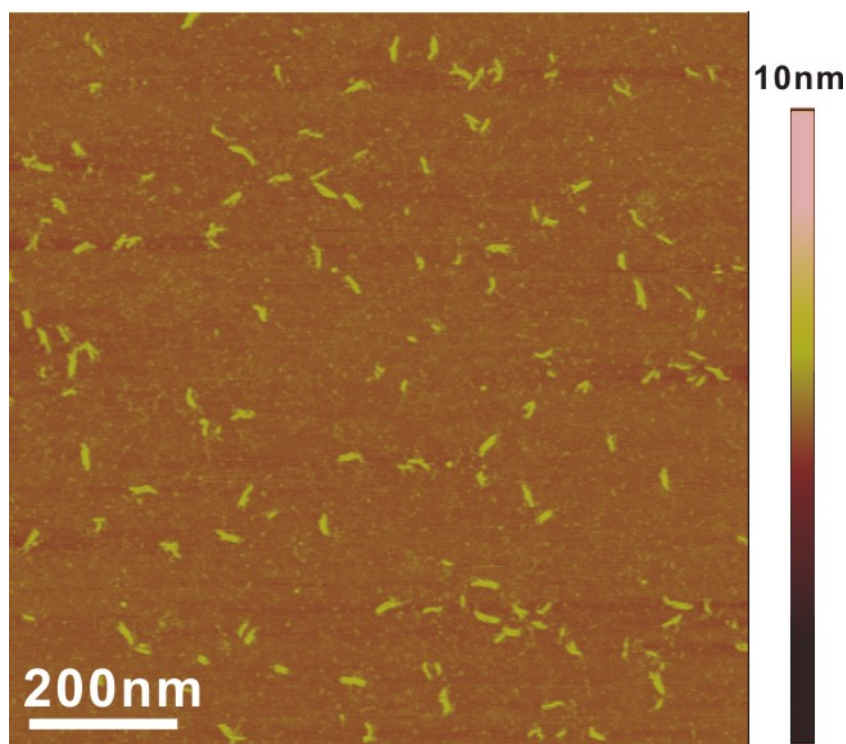


Figure 3.23. Tapping mode height image ($1 \times 1 \mu\text{m}^2$) of DNA-b-PPO-T110 on mica in buffer solution. The concentration was $37.5 \text{ ng}/\mu\text{L}$ and Z range is 10 nm. The histograms are height and length distribution of the rod structures respectively.

In some cases, the pairs consist of two molecules with only part of PPOs joined together. In Figure 3.24, there are 3 pairs of rod structures labeled with white circles. Two of them indicate the pairs that are not perfectly paired but partly combined through PPO. On the right side is the model for one perfectly joined pair.

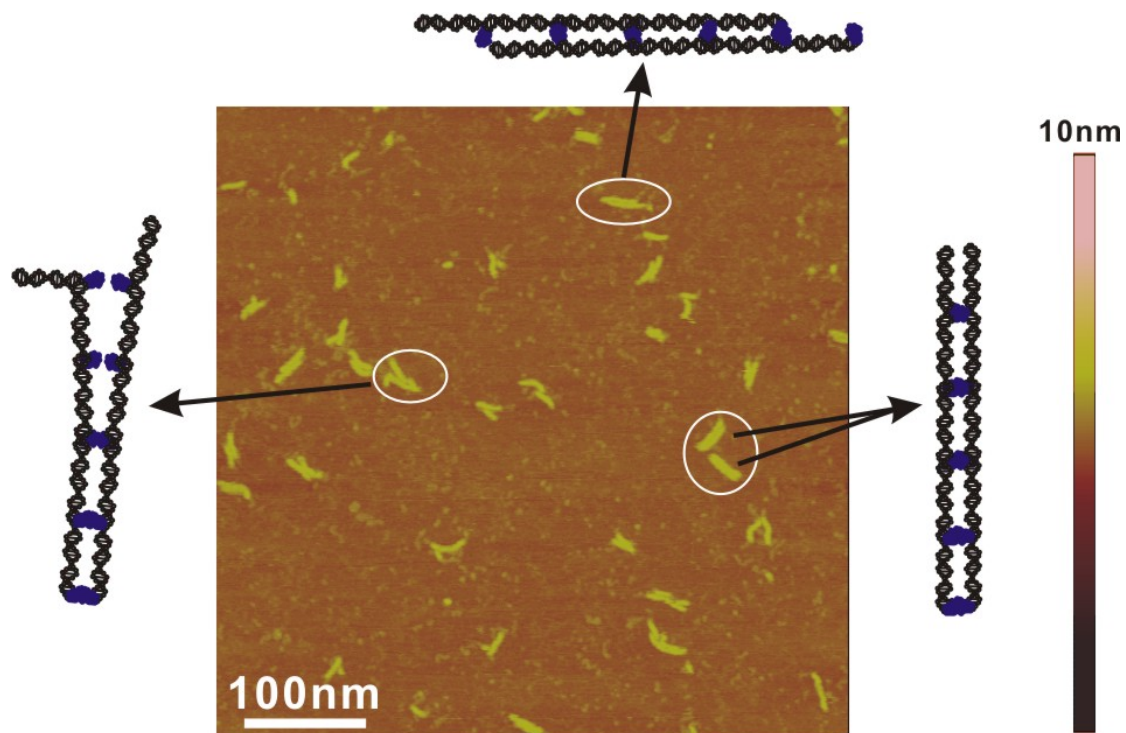


Figure 3.24. Tapping mode height image ($520 \times 520 \text{ nm}^2$) of DNA-*b*-PPO-T110 on mica in buffer solution. The concentration was $37.5 \text{ ng}/\mu\text{L}$ and Z range is 10 nm. Three models illustrating partly paired and totally paired rods are shown.

The single rods and the pairs are observed at higher resolution in Figure 3.25. There are single molecules, perfectly paired rods, and partly paired rods individually. By making a cross section on the pair in left top of the AFM image, the height of them is around 2 nm and the distance between two rods is about 4.5 nm. Sometimes pairs with defected molecule were observed that have shorter length. This is owing to the incomplete hybridization between template and the block copolymers. For example, the labeled pair in consist of one short rod and one twisted rod. The short rod may correspond to the incompletely hybridized molecule. Hence, the two rods are combined through 3 pairs of polymers and the rest part of the DNA-*b*-PPO-T110 molecule becomes more flexible and the kink is formed

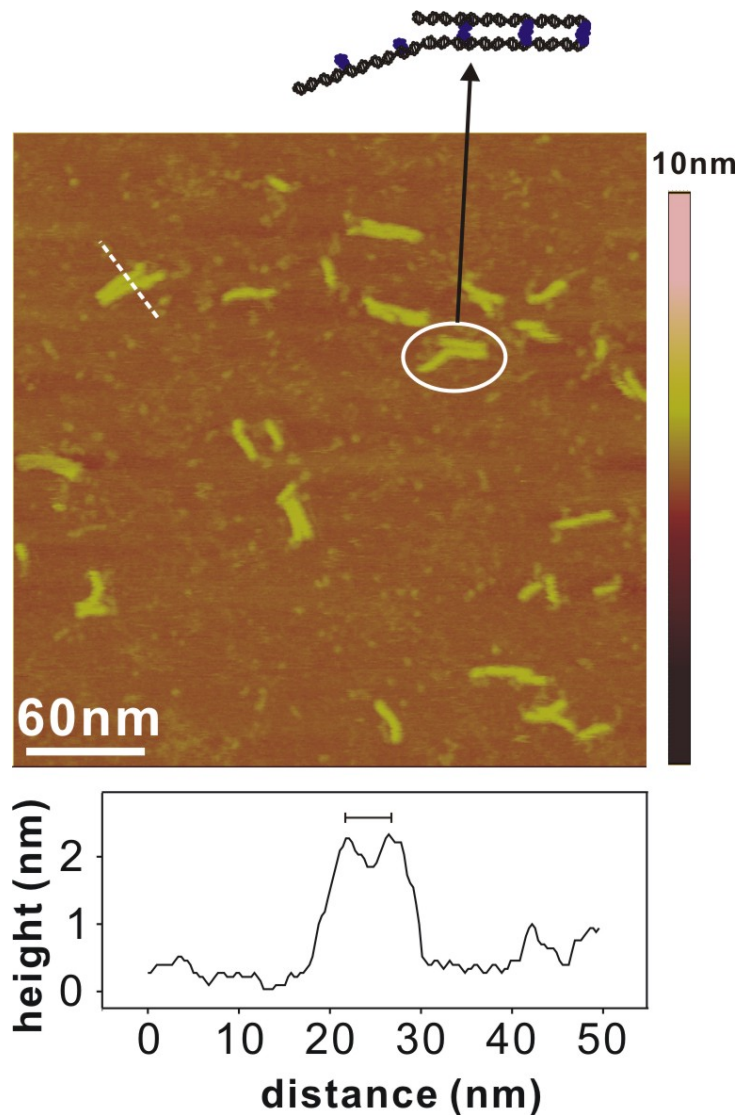


Figure 3.25. Top: Tapping mode height image (**Bottom:** 321X321 nm²) of DNA-*b*-PPO-T110 on mica in buffer solution. There is one example of pair labeled that has defect molecule inside. The concentration was 37.5 ng/μL and Z range is 10 nm. **Bottom:** Cross section analysis across the white dot line in AFM image.

In order to compare the average length from AFM results on similar structured molecules that have different length, DNA-*b*-PPO-T88 molecules have been prepared (Figure 3.26). The only difference between DNA-*b*-PPO-T88 and DNA-*b*-PPO-T110 is the number of repeat ss-DNA-*b*-PPO units. DNA-*b*-PPO-T88 contains 4 repeat units instead of the 5 repeat units in DNA-*b*-PPO-T100. The sequence of the molecule is 5'- (TAACAGGATTAGCAGAGCGAGG)₄-3'.

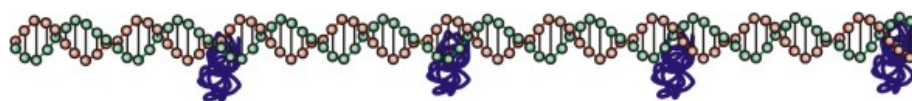


Figure 3.26. Model of one molecule of DNA-b-PPO-T88

They formed also straight or slightly bent pairs of rods together with single rods on mica. Similar to the structures from DNA-b-PPO-T100, the pairs are sometimes fully paired and sometimes partly paired. The average length of the pairs is 30.34 ± 0.22 nm, which is close to the theoretical value ($88 \times 0.34 = 29.92$ nm). The height distribution shows an average value at 1.72 ± 0.03 nm. The model of single rod and pair of rods are shown below the AFM image.

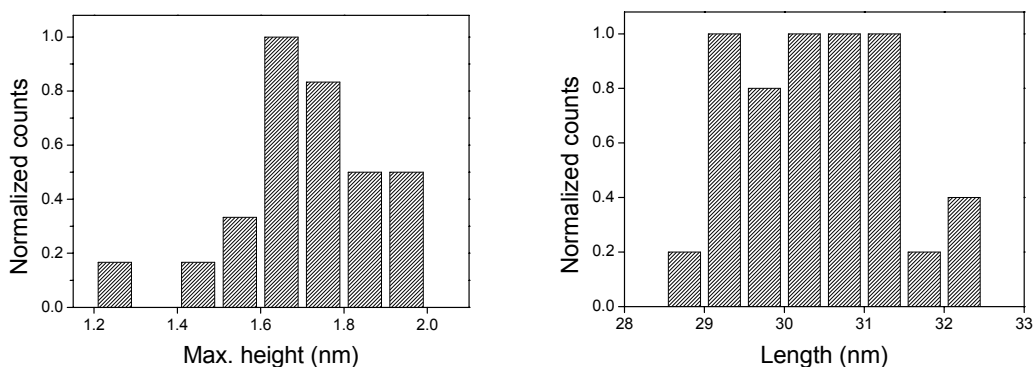
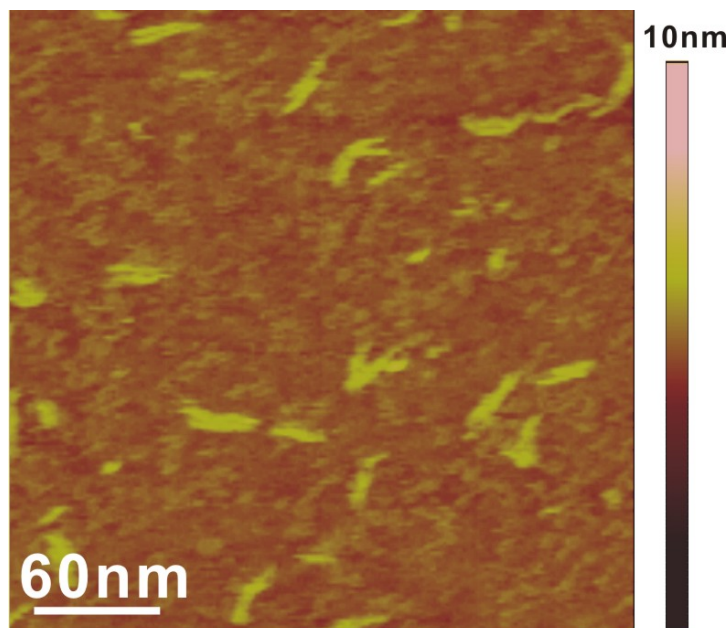


Figure 3.27. Top: Tapping mode height image of DNA-b-PPO-T88 on mica in buffer solution (302×302 nm²). The concentration was 25 ng/ μ L and Z range is 10 nm. **Bottom:** Histograms of length and height distribution of the rod structures.

The single molecules of 100 bp dsDNA haven been imaged to show homogeneous fields of rod like structures²⁹. The rods are either straight or

slightly bent with measured length 33 ± 5 nm. The height was measured to be 0.4 - 0.6 nm and the widths were 11 – 12 nm. For the 200 bp dsDNA, measured lengths are almost twice those of 100 bp DNA. The difference between the measured value and theoretical value is due to the AFM tip radius and the force applied between the tip and the sample.

DNA-*b*-PPO-T100

Both of DNA-*b*-PPO-T110 and DNA-*b*-PPO-T88 contain the same repeat unit of ss-DNA-*b*-PPO which has 22 bases in ODN. Since one turn of DNA consists of 10 to 11 bases, polymer existing in every 20 bases should also be approximately two turns and orient to one direction. Based on the sequences of DNA-*b*-PPO-T110, we leave 2 bases unpaired from each repeat unit of 22mer ss-DNA-*b*-PPO by making them not complementary to the ss-DNA back bone (Figure 3.28). In this way, the flexibility of the PPO that is attached with the rest two bases (5' end) is higher than that of DNA-*b*-PPO-T110. The sequence of this molecule of DNA-*b*-PPO-T100 is 5'-(TAACAGGATTAGCAGAGCGA)₅-3'.

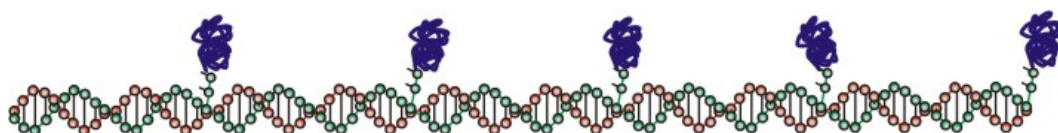


Figure 3.28. Model of DNA-*b*-PPO-T100 molecule. The molecule consists of a single strand DNA with 100 bases and 5 repeating units of ssDNA(22mer)-*b*-PPO with complementary DNA sequences. In each repeat unit 20 bases are complementary with back bone and the rest 2 bases are unpaired.

The AFM imaging on DNA-*b*-PPO-T100 on mica surface showed also straight or slightly bent pairs together with singly separated molecules (Figure 3.29). The average length of the pairs is 33.79 ± 0.23 nm, which is similar to the theoretic length ($100 \times 0.34 = 34$ nm). The height distribution shows an average value at 1.69 ± 0.03 nm. The model of the structures is shown below the AFM image.

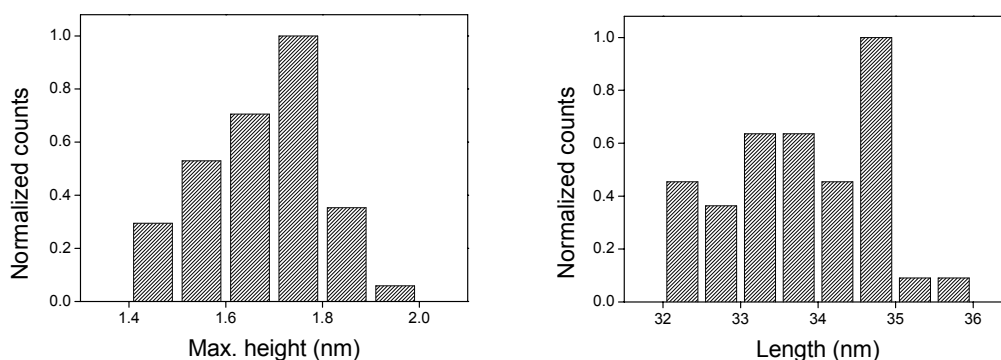
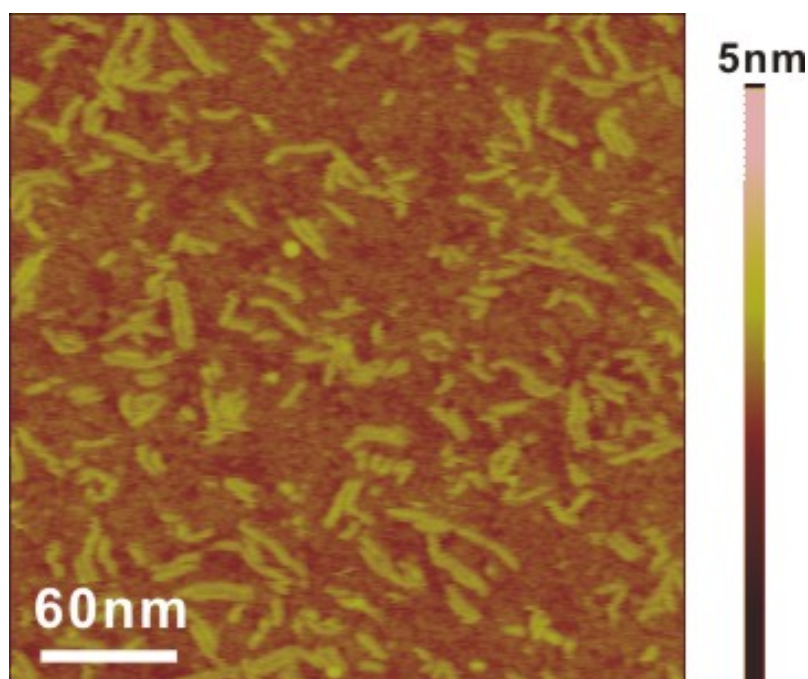


Figure 3.29. Tapping mode height image of DNA-*b*-PPO-T100 on mica in buffer solution (300X300 nm²). The concentration was 50 ng/μL and Z range is 5 nm. Histograms on bottom show the length and height distribution of the rod structures.

In order to investigate whether different cooling times in the synthesis procedure influence the structures of the molecules, the cooling time has been increased from to 3 days in the synthesis process. From the AFM images, the molecules formed pairs of rods in a higher density (Figure 3.30). The cross section analysis across two pairs of rods exhibits a peak to peak distance of 5 nm which is slightly larger than the 4.5 nm for DNA-*b*-PPO-T110. This is reasonable considering the molecular structures for DNA-*b*-PPO-T110

and DNA-*b*-PPO-T100 who has 2 rest bases between polymer and the backbone. Here most of the rods in one pair are parallel with each other. Occasionally, single rods were also observed. The length and height of the rods have no significant changes than those of previous sample. The results from DNA-*b*-PPO-T100 illustrates that increasing the flexibility of the polymers does not prevent the pairs formation. The density of the pairs increased from 25.9% to 57% by calculating 21 pairs with 60 single rods in Figure 3.29 and 80 pairs with 60 single rods in Figure 3.30. This indicates that the polymers on the molecules need enough flexibility to move in order to find other PPO for pair's formation.

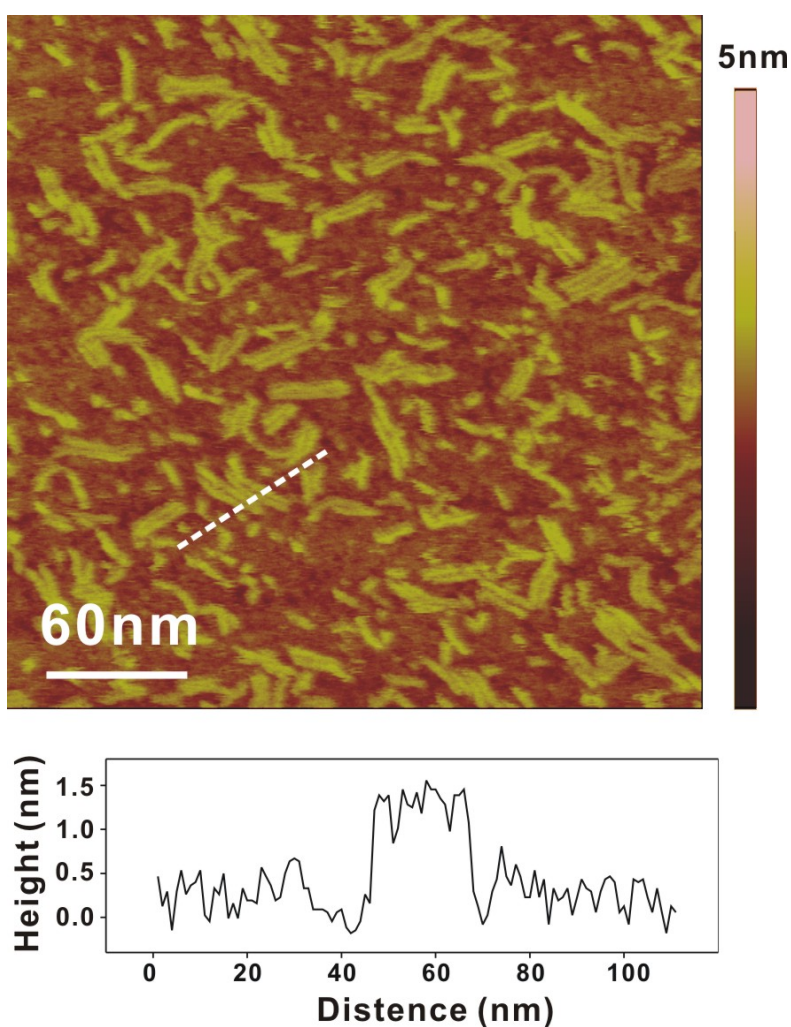


Figure 3.30. Top: Tapping mode height image of DNA-*b*-PPO-T100 on mica in buffer solution ($300 \times 300 \text{ nm}^2$). The concentration was $50 \text{ ng}/\mu\text{L}$ and Z range is 5 nm. **Bottom:** Cross section analysis on two pairs of rods in the top AFM image.

Furthermore, we moved the two rest bases from 5' end of DNA to the 3' end on DNA-*b*-PPO-T100 in order to induce spatial hindrance around polymer block and we call this molecule DNA-*b*-PPO-T100'. It has the sequence of 5'-(ACAGGATTAGCAGAGCGA)₅-3'. From the AFM investigation, most of the molecules exist as single rods and only few pairs were observed on mica (Figure 3.31). There are three pairs labeled by white arrows in the image. This indicates that enough spatial area is necessary for polymers to find each other in order to form pairs.

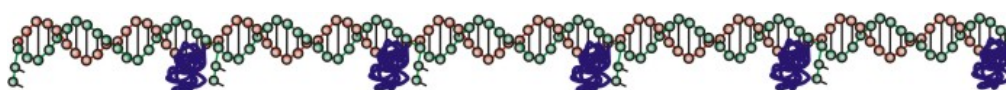
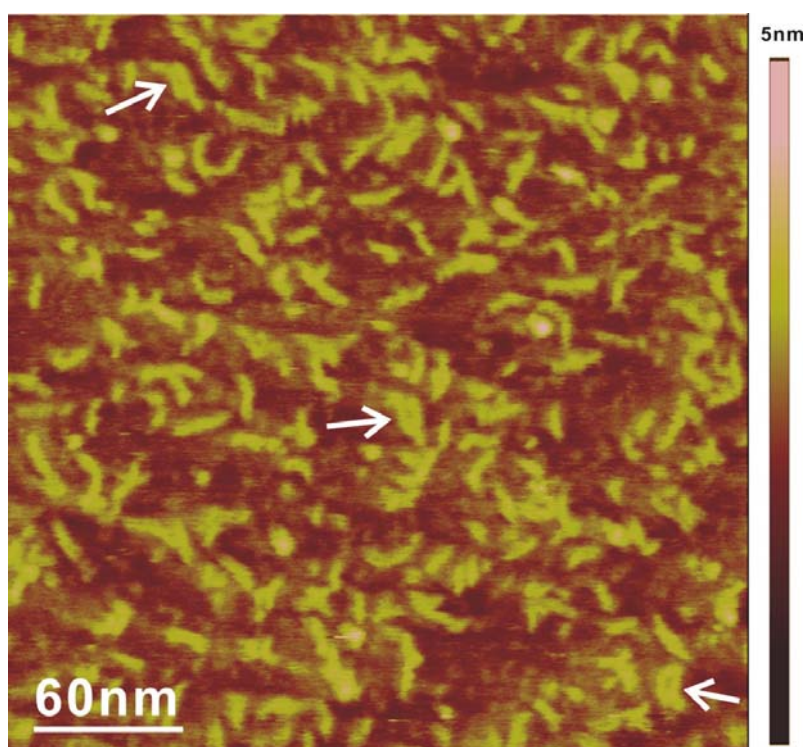


Figure 3.31. Top: Tapping mode height image of DNA-*b*-PPO-T100' on mica in buffer solution (300X300 nm²). The concentration was 22.5 ng/μL and Z range is 5 nm. **Bottom:** Model of one molecule of T100'. The molecule consists of a single strand DNA with 100 bases and 5 repeating units of ss-DNA-*b*-PPO with complementary DNA sequences. In each repeat unit 20 bases are complementary with back bone and the rest 2 bases are unpaired.

Control measurement on DNA-*b*-PPO-T100

In order to prove that the hydrophobic interaction between polymers in DNA-*b*-PPO-T100 is the main parameter for pair's formation, the short DNA sequences without polymers were attached to DNA backbone was studied as a control measurement. Here we do not see any pairs but only singly separated molecules at 50 ng/ μ L (Figure 3.32 top image). By decreasing the concentration to 25 ng/ μ L, the AFM image in the middle of Figure 3.32 does not show any pair structures as well. This proves that the hydrophobic interaction between polymers is necessary for pair's formation.

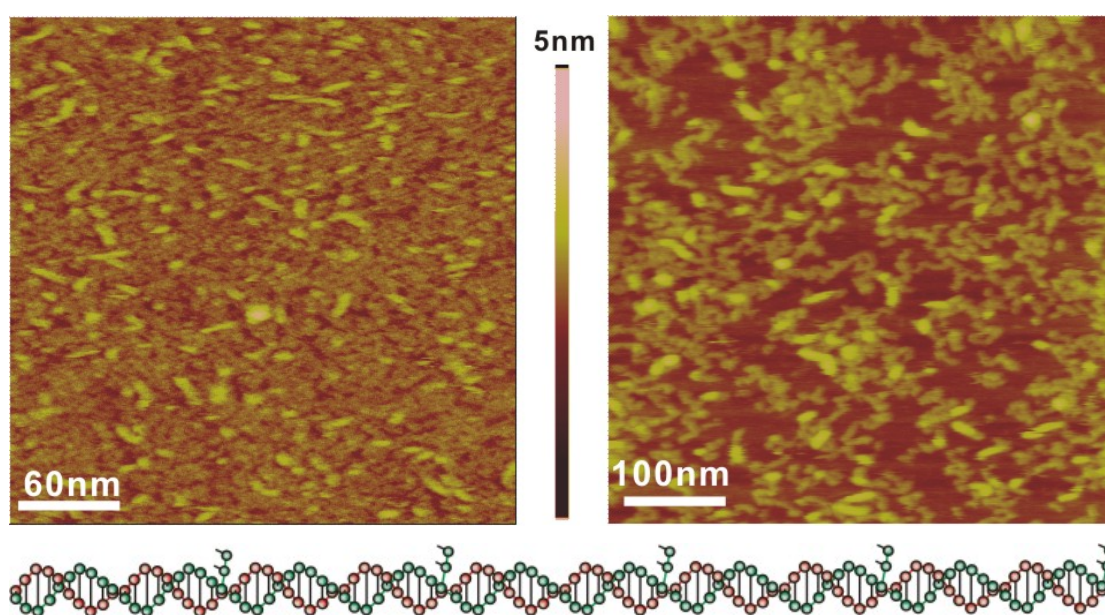


Figure 3.32. **Top:** Tapping mode height images of DNA-*b*-PPO-T100 controller on mica in buffer solution (**Left:** 300X300 nm²; Z range 5 nm. **Right:** 500 X500 nm²; Z range 5 nm). The concentration was 50 ng/ μ L for left image and 25 ng/ μ L for right image. **Bottom:** Model of one molecule of T100 controller. The molecule consists of a ss-DNA template with 100 bases and 5 repeating units of ss-DNA-*b*-PPO with complementary DNA sequences. In each repeat unit 20 bases are complementary with back bone and the rest 2 bases are unpaired. There is no polymer attached to the molecule.

FCS on DNA-*b*-PPO-T100

The frictional coefficient for rod-like particle can be derived by assuming a rod with length of $2a$ and radius of b . The volume is given by $V_{rod} = 2\pi ab^2$. The

axial ratio P is defined as $P = \frac{a}{b}$. The frictional coefficient is defined as $f = f_0 \frac{(2/3)^{1/3} P^{2/3}}{\ln(2P) - 0.30}$ where f_0 is defined as $f_0 = 6\pi\eta R_0$. R_0 is the radius of a sphere which has a volume equal to the volume of the rod. It is determined as: $V_{sphere} = V_{rod} \Rightarrow \frac{4\pi}{3} R_0^3 = 2\pi ab^2 \Rightarrow R_0^3 = \frac{3ab^2}{2} \Rightarrow R_0 = \sqrt[3]{\frac{3ab^2}{2}}$. The diffusion time τ_D and diffusion coefficient D were measured by FCS with laser focus diameter ω : $\tau_D = \omega^2 / 4D$ and $f = kT / D \Rightarrow \tau_D = (\omega^2 / 4kT) \times f$. Accordingly the expected ratio of the diffusion times for the aggregates of the hybridization products DNA-*b*-PPO-T100 to controller (ds-T100) was calculated using the AFM structural information.

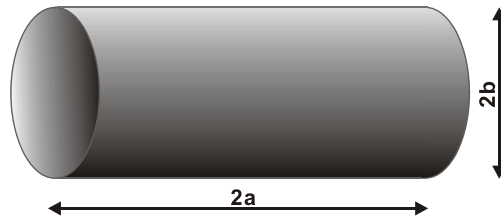


Figure 3.33. Model of rod like structure which has a length of $2a$ and radius of b .

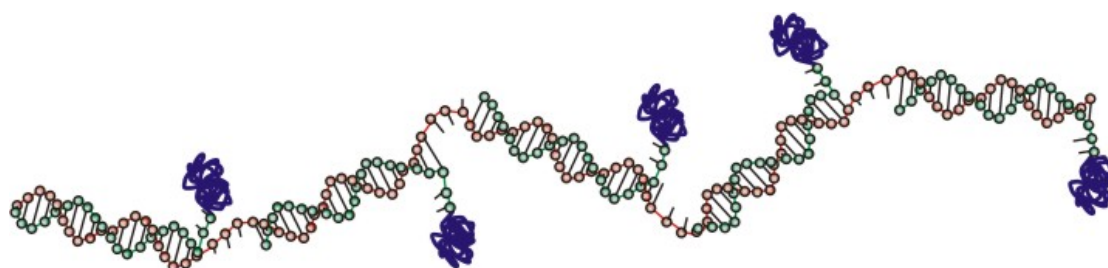
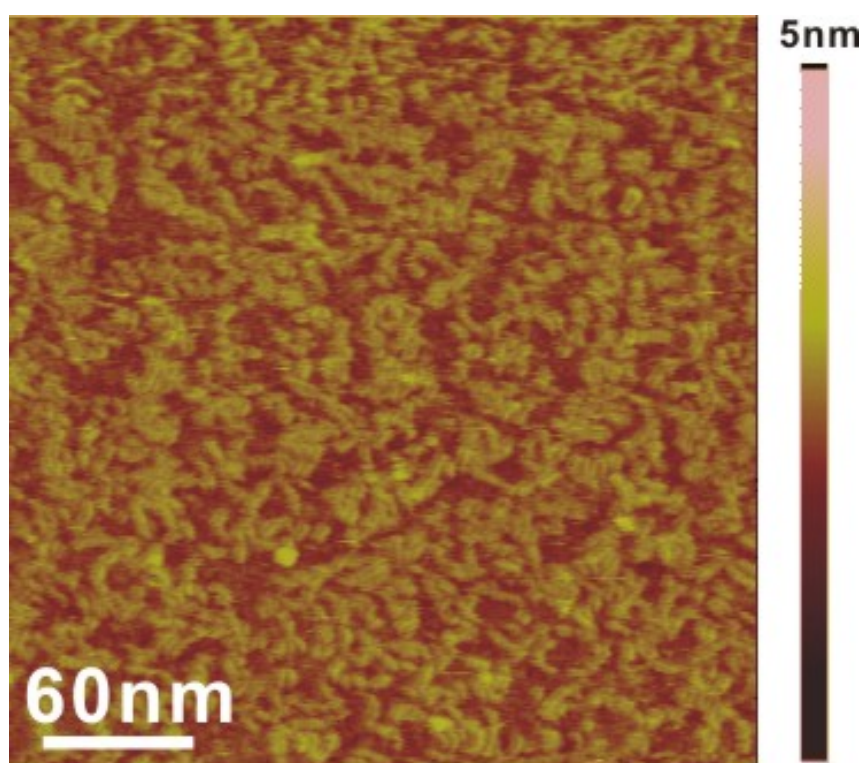
From AFM data on length and height values for pairs and controllers as ds-DNA, P , R_0 , and f can be calculated and the data are shown in Table 3.1. Theoretical diffusion time changes as predicted by AFM data shows $\tau_{D, pairs} / \tau_{D, controllers} = 1.467$. From the FCS measurement, $\tau_{D, pairs} / \tau_{D, controllers} = 1.29$, which is in good agreement with the theoretical data.

	a(nm)	b(nm)	P	R0(nm)	f(nm)
Pair	17	1.75	10	4.274	$6\pi\eta \times 6.429$
Control	17	0.875	20	2.641	$6\pi\eta \times 4.382$

Table 3.1. FCS measurement values of a , b , P , R_0 , and f for DNA-*b*-PPO-T100 pairs and controls.

DNA-*b*-PPO-T115

The flexibility and the spatial hindrance of the polymers have been proved to have influences on structures formed in DNA-*b*-PPO-T88, DNA-*b*-PPO-T100, and DNA-*b*-PPO-T110 molecules. Furthermore, flexibility of the backbone could also be changed by modifying the base sequences. We have synthesized DNA-*b*-PPO-T115 with 15 unpaired bases on template and 2 rest bases on DNA-*b*-PPO unit connecting with PPOs. The sequence is 5'-(TAACAGGATTAGCAGAGCGATTT)₅-3'. The flexibility in backbone and the polymers make the molecule more flexible. From AFM studies on this molecule, it formed flexible network at 50 ng/μL on mica which is shown in Figure 3.34.



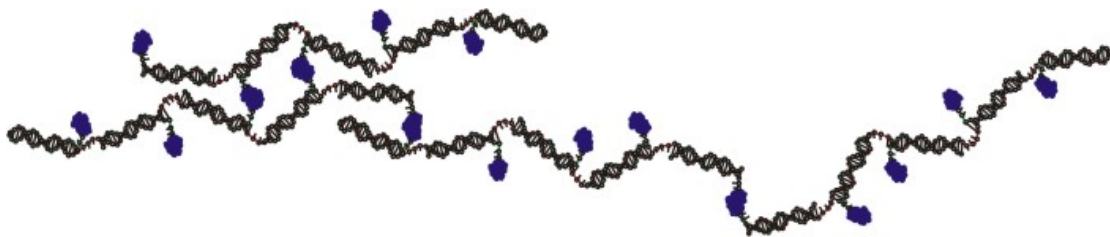


Figure 3.34. *Top:* Tapping mode height image of DNA-b-PPO-T115 on mica in buffer solution ($300 \times 300 \text{ nm}^2$). The concentration was $50 \text{ ng}/\mu\text{L}$ and Z range is 5 nm . **Bottom:** Model of one molecule of DNA-b-PPO-T115 and the network formed from 4 molecules of DNA-b-PPO-T115. The molecule consists of a ss-DNA template with 115 bases and 5 repeating units of ss-DNA-b-PPO with complementary DNA sequences. In each repeat unit 20 bases are complementary with back bone and the rest 2 bases are unpaired. In addition, there are 15 unpaired bases on the back bone, which increases flexibility of the molecule.

DNA-b-PPO-T90

Molecules having repeat unit with 20 – 22 bases that are approximately two turns of DNA enable the polymers orient all in the same direction, which help the polymers to find each other for forming pair structures. It is necessary to study the structures formed from the molecules with PPOs in the opposite position next to each other. The neighboring PPOs have 180° in between if there are 15 or 16 bases (correspond to 1.5 turn) in each repeating unit. For this purpose, molecule of DNA-b-PPO-T90 (Figure 3.35) has been synthesized. The sequence is $5'-(\text{ATTAGCAGAGCGAGG})_6-3'$.

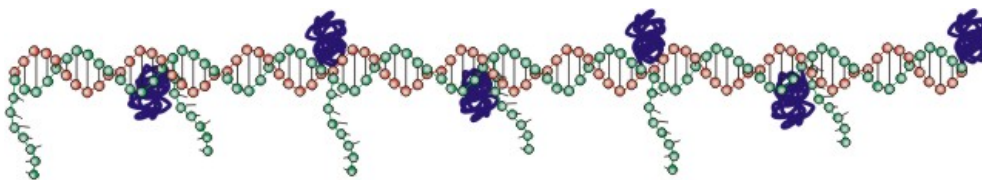


Figure 3.35. Model of molecule DNA-b-PPO-T90. The molecule consists of a ss-DNA with 90 bases and 6 repeating units of ss-DNA-b-PPO with complementary DNA sequences. In each repeat unit 15 bases are complementary with back bone and the rest 7 bases are unpaired.

The AFM image on DNA-*b*-PPO-T90 (Figure 3.36) does not show any ordered structures but single rods. This is probably due to the spatial hindrance of the rest 7 bases that prevent the polymers to find each other.

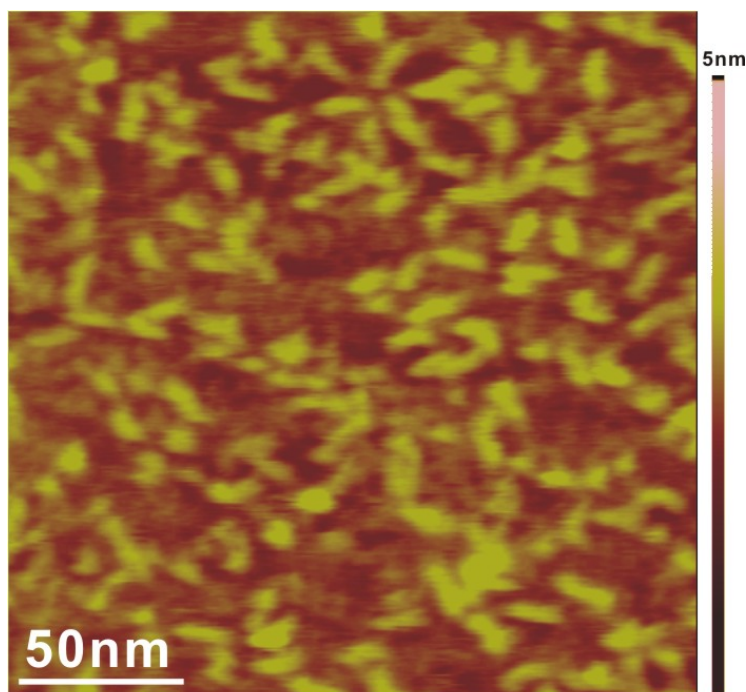


Figure 3.36. Tapping mode height image of DNA-*b*-PPO-T90 on mica in buffer solution (210X210 nm²). The concentration was 11.25 ng/μL and Z range is 5 nm.

3.1.6 Concentration

Concentration is an important element for achieving different kind of structures. Single molecules together with dimers have been observed below the CMC and globular micelles were observed above the CMC for both ss- and ds-DNA-*b*-PPOs. Further increasing the concentration on ss-DNA-*b*-PPO resulted in a higher density of the micelles. For the long templated molecules, e.g. DNA-*b*-PPO-T110, single molecules have been observed as rod like structures on mica surface with a concentration of 37.5 ng/μL (Figure 3.23 - Figure 3.25). Increasing the concentration to 50 ng/μL resulted in a denser network that is shown in Figure 3.37. In such a dense network, there are obvious pairs of rods as well. From the first image with 1 X 1 μm² scan area, homogeneous layer of rods was observed. Zooming into higher resolution

resulted in more clear rods and pairs of rods. Here it is hard to measure the length of the rods because the rods are joined together and the beginning and ending of one rod is hardly to define. The height of the rods is 1-1.3 nm from the cross section analysis along the white dot line in the bottom AFM image. The distance between two neighbor rods is around 3.5 nm.

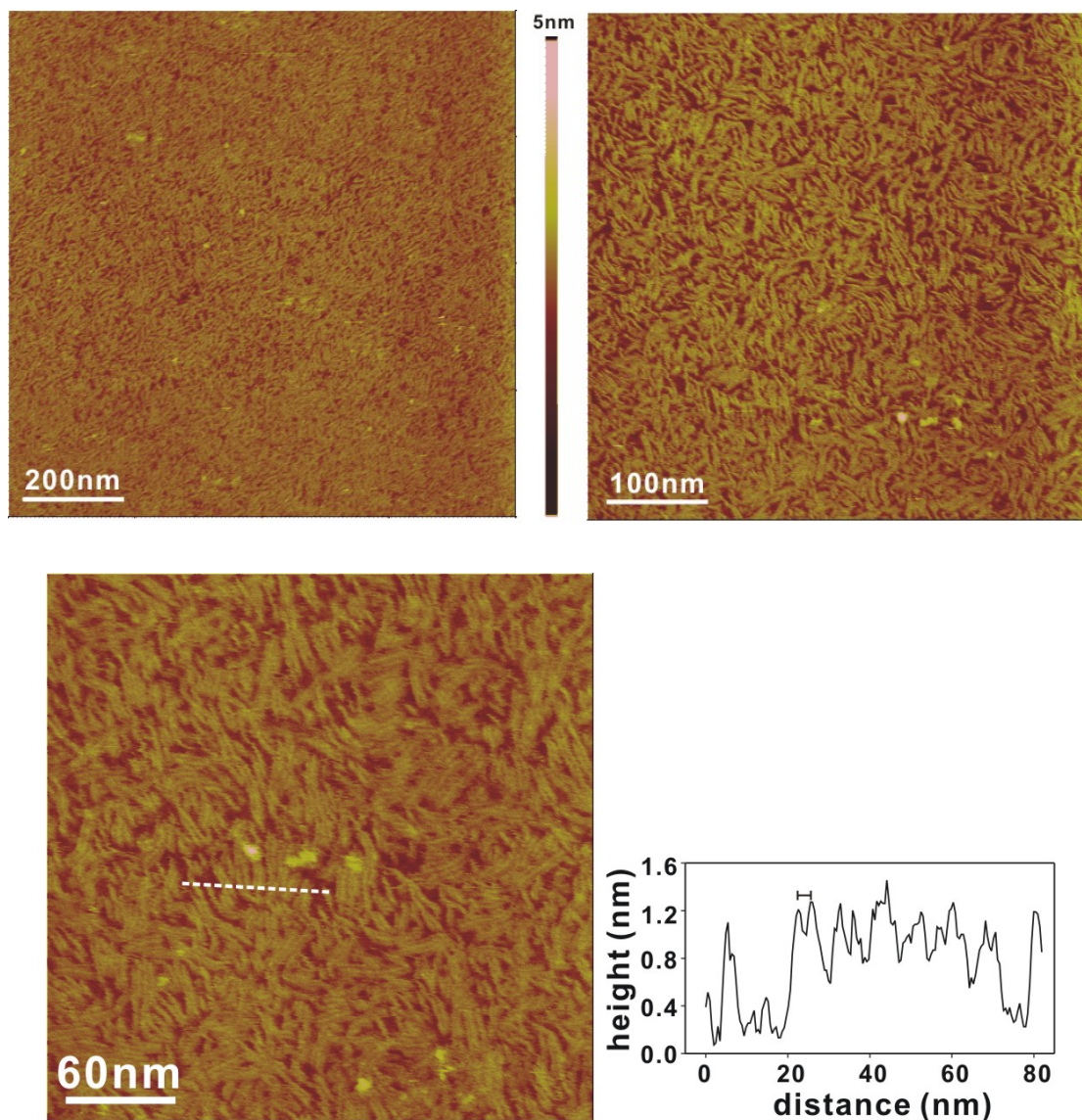


Figure 3.37. Tapping mode height images in different scale on one sample of T110 on mica in buffer solution (**Top left:** $1 \times \mu\text{m}^2$. **Top right:** $500 \times 500 \text{ nm}^2$. **Bottom:** $300 \times 300 \text{ nm}^2$). **Bottom right:** cross section analysis along the white dot line in left AFM image. The concentration was $50 \text{ ng}/\mu\text{L}$ and Z range is 5 nm for all the images.

3.1.7 Equilibrium time

The equilibrium time is the time between taking the sample out of the freeze and starting AFM measurement. All of the measurements above were done on fresh prepared samples meaning only 10 – 20 min equilibrium time. However, if more equilibrium time was given on these molecules for their self-organization, they may form higher ordered structures.

In our experiment, higher ordered structure was observed which is shown in Figure 3.38 by depositing DNA-*b*-PPO-T90 in buffer solution at room temperature for 3 days before imaging. Compared with the structures from the same molecule but less equilibrium time in Figure 3.37, longer equilibrium time resulted in more regular rods. The height of the rod like structure was measured to be 1-1.5 nm by cross section analysis along the white dot line in AFM image.

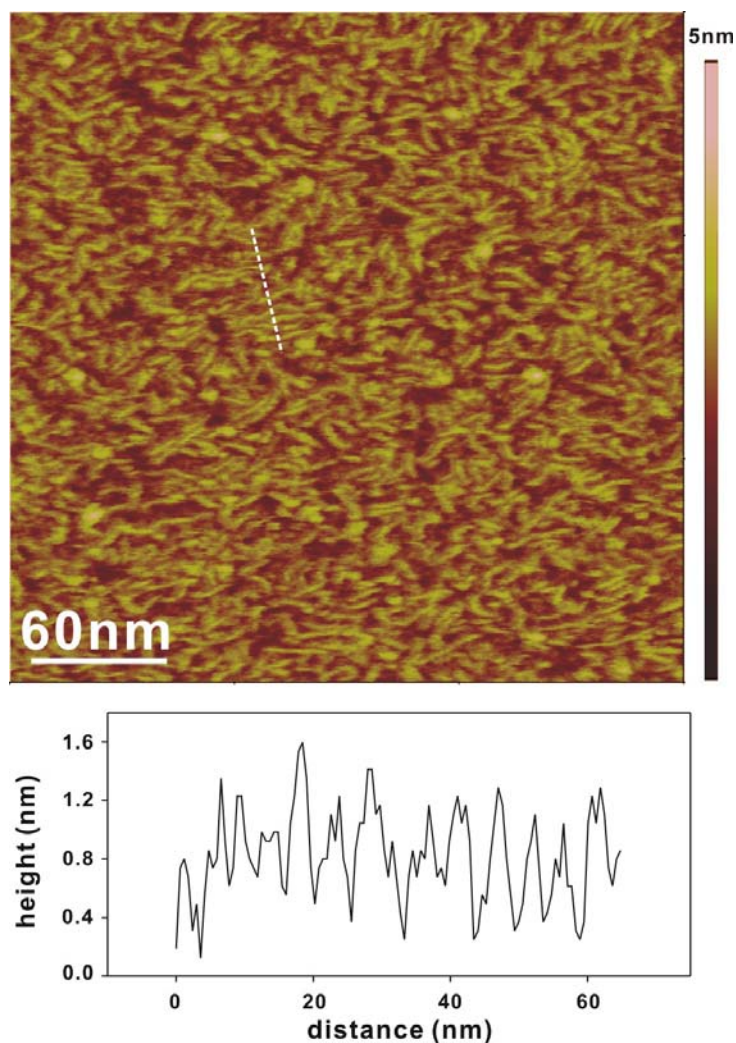


Figure 3.38. **Top:** Tapping mode height image of T90 on mica in buffer solution ($300 \times 300 \text{ nm}^2$). The concentration was $50 \text{ ng}/\mu\text{L}$ and Z range is 5 nm. **Bottom:** Cross section analysis along the white dot line in the top AFM image.

3.1.8 Sublayer

For most of the observed images, there is always a sublayer of amorphous molecules other than rod like structure or globular micelles on mica surface. The height of this sublayer is around 1 nm which is corresponding to one DNA-*b*-PPO molecules. This might be due to the strong affinity of DNA to mica with the help of Ni^{2+} . The subsequent rod like structures or micelles is able to settle down on this layer. Figure 3.39 shows a topographic image of controller of DNA-*b*-PPO-T100 with two layers on mica surface. The section

analysis is across two profiles: bright toplayer and dark sublayer. The height difference between these two layers is around 3 nm.

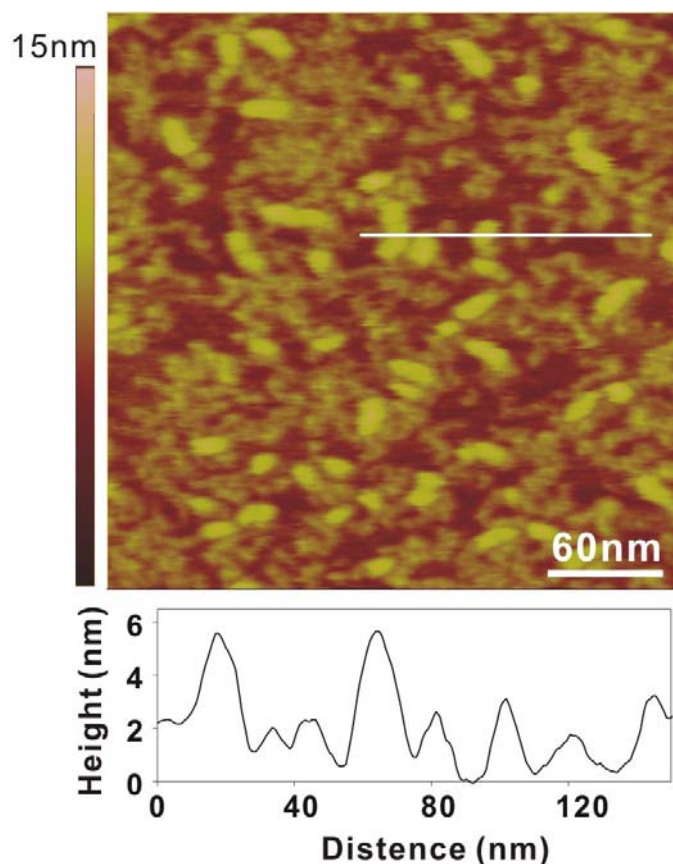


Figure 3.39. *Top:* Tapping mode height image of Control T100 on mica in buffer solution (300X300 nm²). The concentration was 25 ng/ μ L and Z range is 15 nm. *Bottom:* Cross section analysis along the white line in the top AFM image.

3.1.9 Phase contrast

Phase image often provides significantly more contrast than the topographic image and has been shown to be sensitive to material surface properties, such as stiffness, viscoelasticity, and chemical composition. Changes in phase angle during scanning are related to energy dissipation during tip-sample interaction. Figure 1.3 shows strong phase contrast because there is only one layer of the molecules on mica surface. The phase image could have no phase contrast due to a dense sublayer covered on mica. For example, Figure 3.40 shows two pair of height versus phase images. In the top images are there two layers on mica surface. The corresponding phase image shows

no contrast between the molecules and the mica surface since the first layer is so dense that the mica is invisible. However, in the bottom images, the first layer does not fully cover the mica surface and the mica was observed from the height image as the darkest layer. In this case, the phase contrast is visible.

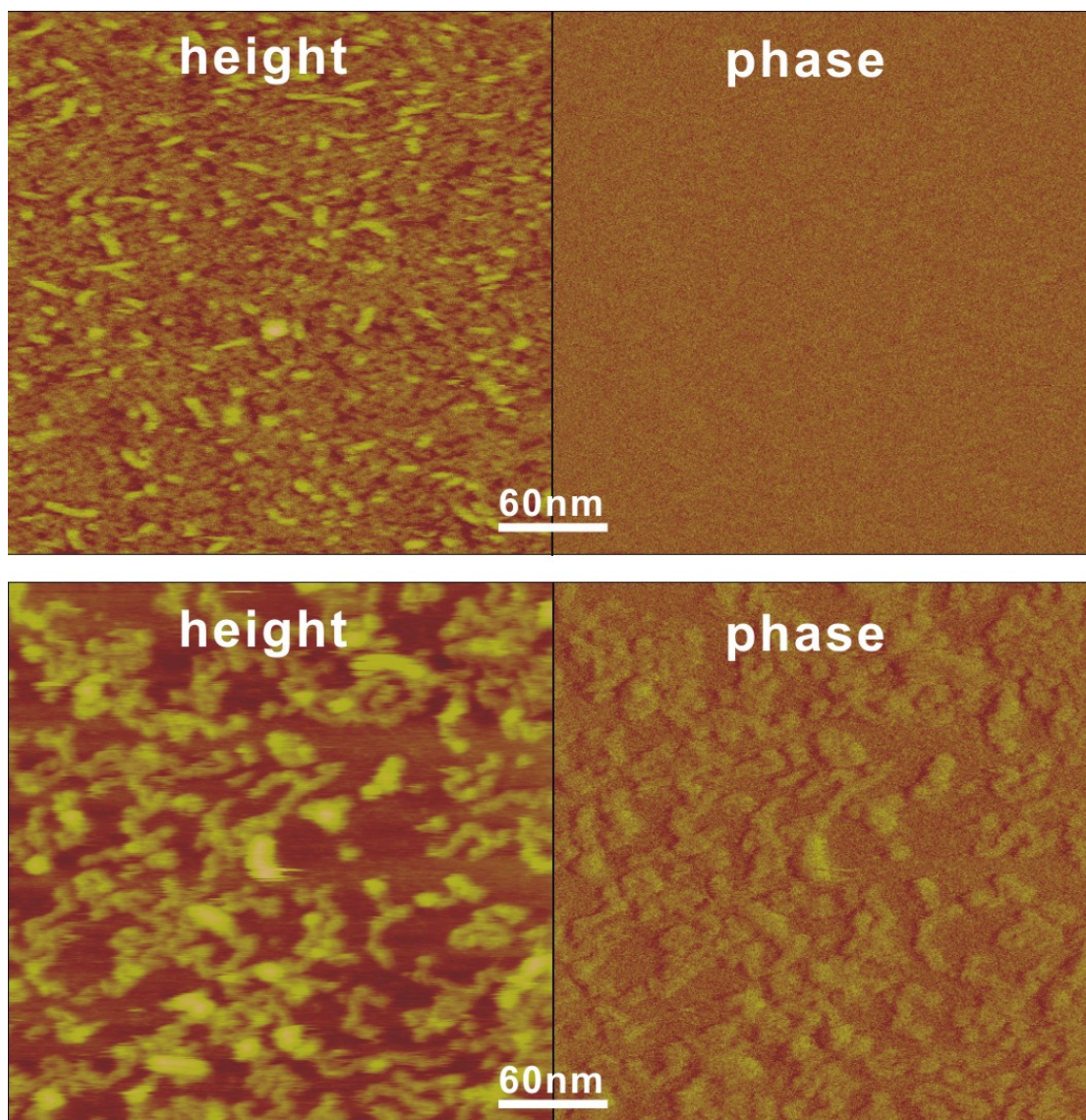


Figure 3.40. Tapping mode height and phase images of control T100 on mica in buffer solution ($300 \times 300 \text{ nm}^2$). The concentration was $50 \text{ ng}/\mu\text{L}$ for the top two images and was $25 \text{ ng}/\mu\text{L}$ for the bottom two images. The Z range is 5 nm for the height images and 5° for the phase images.

3.1.10 Summary of the dimensions of structures by AFM

The analysis on the structures was basically made by measuring height for micelles and the length and height for rods. The obtained value of height is dependent only on the force applied but not the tip radius of curvature, which is the reason for always using the height for comparisons since soft tapping was applied for all the AFM imaging processes. The diameter, length, and width is significantly dependent on the tip radius and the force applied between the tip and the samples. Therefore, our conclusions mostly rely on the average height values by keeping the force minimum in all the measurements. Table 3.3 shows the height and diameter of the micelles and Table 3.3 shows the height and length of the rods. The average heights of the micelles and rods are in the range between 4-6 nm and around 2 nm, respectively. The diameter of the micelles distribute widely, which is not considered as real diameter of the micelles in our experiments. In addition we can exclude artifacts from a double tip since the appearing complexes show different orientation relative to the scanning direction in one image.

micelles	ss-DNA-<i>b</i>-PPO (5ng/μL)	ss-DNA-<i>b</i>-PPO (25ng/μL)	ss-DNA-<i>b</i>-PPO (50ng/μL)	ds-DNA-<i>b</i>-PPO (100ng/μL)
height (nm)	5.16 ± 1.79	4.39 ± 0.15	5.26 ± 1.63	5.81 ± 0.26
diameter (nm)	15 ~ 30	10 ~ 20	20 ~ 30	35 ~ 50

Table 3.2. Height and diameter of the micelles measured from DNA-*b*-PPO at different concentrations.

rods	DNA-<i>b</i>-PPO-T88 (25ng/μL)	DNA-<i>b</i>-PPO-T100 (50 ng/μL)	DNA-<i>b</i>-PPO-T110 (37 ng/μL)
height(nm)	1.72 ± 0.03	1.69 ± 0.03	1.94 ± 0.01
length(nm)	30.34 ± 0.22	33.79 ± 0.23	37.15 ± 0.18

Table 3.3. Height and length of the rods measured from long templated molecules (DNA-*b*-PPO-T88, DNA-*b*-PPO-T100, and DNA-*b*-PPO-T110).

3.2 AFM studies in air on drop casted films

In addition to in-situ AFM investigations in buffer solutions, drop casted thin films have been investigated in air under AFM. The reason why to use drop casting but not spin coating is that the DNA block copolymers are dissolved in water and the evaporation process is relatively slow. Such solution will be thrown away from the substrate during spin coating process. However, it is difficult to obtain a homogeneous film by means of drop casting. In fact, the center of a drop casted film is always thinner than in the rim. For AFM imaging, the tip was always kept to be in the center area of the sample and structures were captured from different positions among this center area.

3.2.1 Micelles

ss-DNA-*b*-PPO

On the drop casted films, ss-DNA-*b*-PPO formed globular micelles (Figure 3.41) on mica surface at 5 ng/ μ L at room temperature. This is probably due to the low T_g of PPO at -70°C. The average height of the micelles was measured to be 4.57 \pm 0.69 nm, which is in the same range to the 4-6 nm from the in-situ AFM studies.

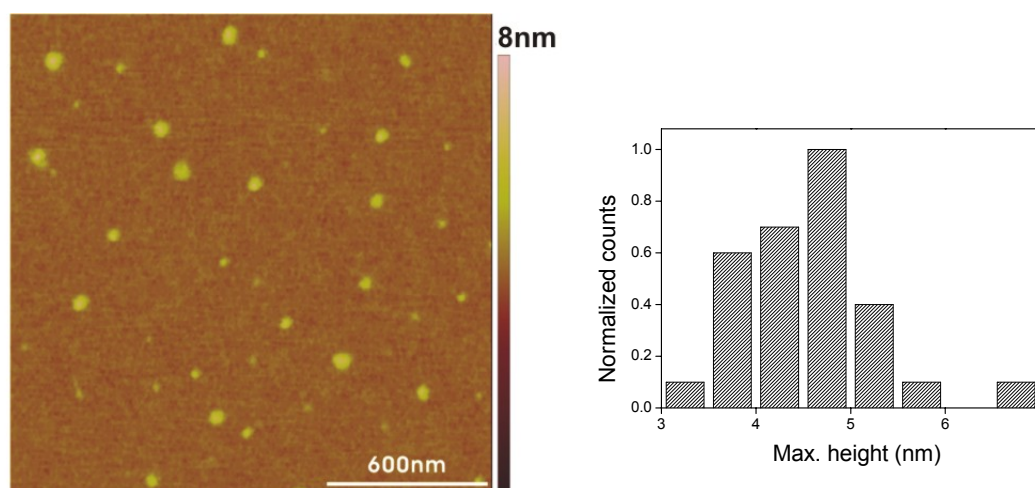


Figure 3.41. AFM height image ($1.8 \times 1.8 \mu\text{m}^2$) of micelles formed from ss-DNA-*b*-PPO on mica surface at RT. The concentration was 5 ng/ μ L and Z range is 8 nm. The histogram shows the height distribution of the micelles.

ss-DNA-*b*-PS

Only after annealing of the drop casted ss-DNA-*b*-PS films at 100°C for 12h, DNA-*b*-PS with 5500 g/mol PS and 16mer ODNs (5a) formed globular micelles on hydrophilic silicon surface (Figure 3.42). The white frame in both images labeled 4 typical globular micelles. In addition, there are larger aggregates in left image. The average height of the micelle is 10.88 ± 1.36 nm.

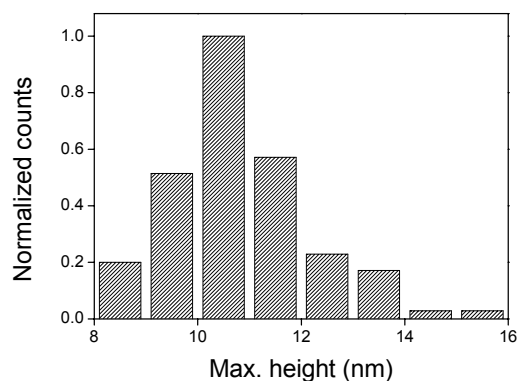
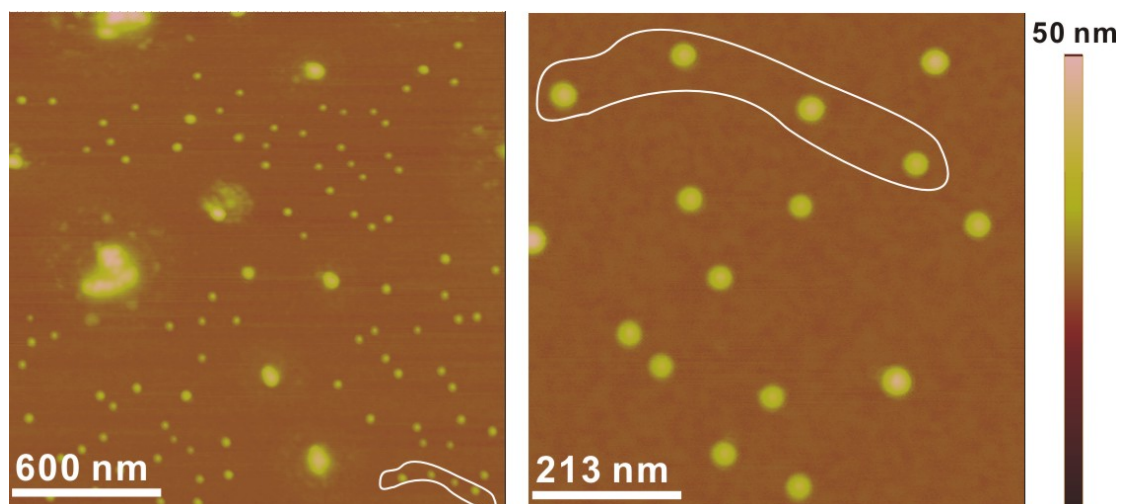


Figure 3.42. AFM height images of 5a (ss-DNA-*b*-PS with 55000 g/mol PS) on silicon surface after annealing at 100°C for 12h. (**Left:** $2 \times 2 \mu\text{m}^2$; **Right:** $710 \times 710 \text{ nm}^2$) The concentration was 5 ng/ μL and Z range is 50 nm for both images. The histogram in bottom shows the distribution of maximum height of the micelles.

3.2.2 Dendritic structures

When preparing the ss-DNA-*b*-PS sample at the concentration $>30 \text{ ng}/\mu\text{L}$, it formed micrometer thick films. Hence, it was difficult using AFM for the investigation on the surface structures. When we reduced the concentration to the value $<3 \text{ ng}/\mu\text{L}$, the sample was so diluted that the surface structure was invisible by AFM. Therefore the concentration for AFM investigations was adjusted between $3 \text{ ng}/\mu\text{L}$ – $30 \text{ ng}/\mu\text{L}$. Figure 3.43 shows typical AFM images at $3 \text{ ng}/\mu\text{L}$ and optical images at $30 \text{ ng}/\mu\text{L}$ of DNA-*b*-PS with 56000 g/mol PS and 16mer ODNs (5c) on silicon surface. Dendritic structures formed in both conditions.

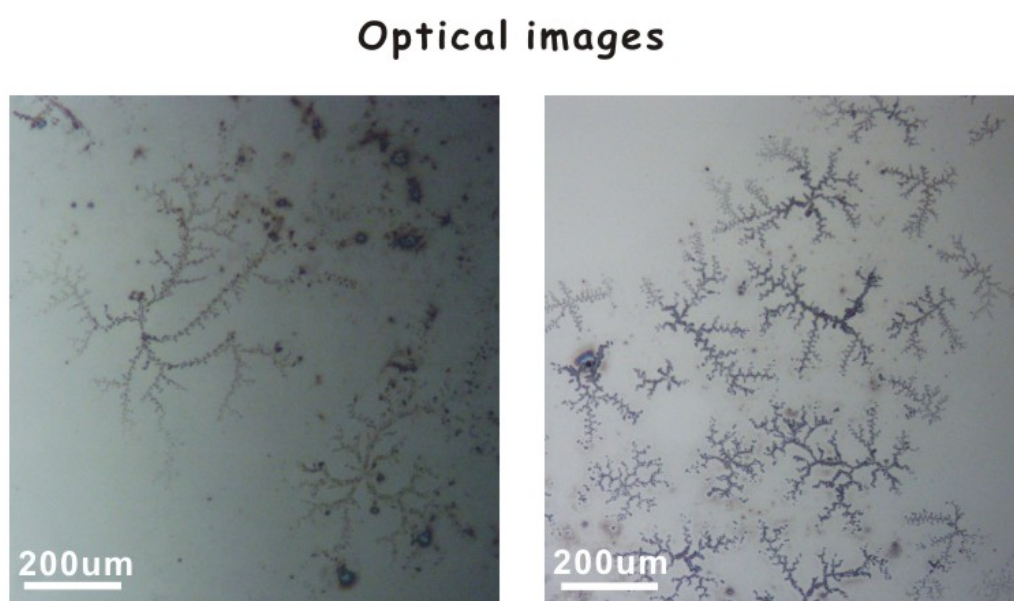
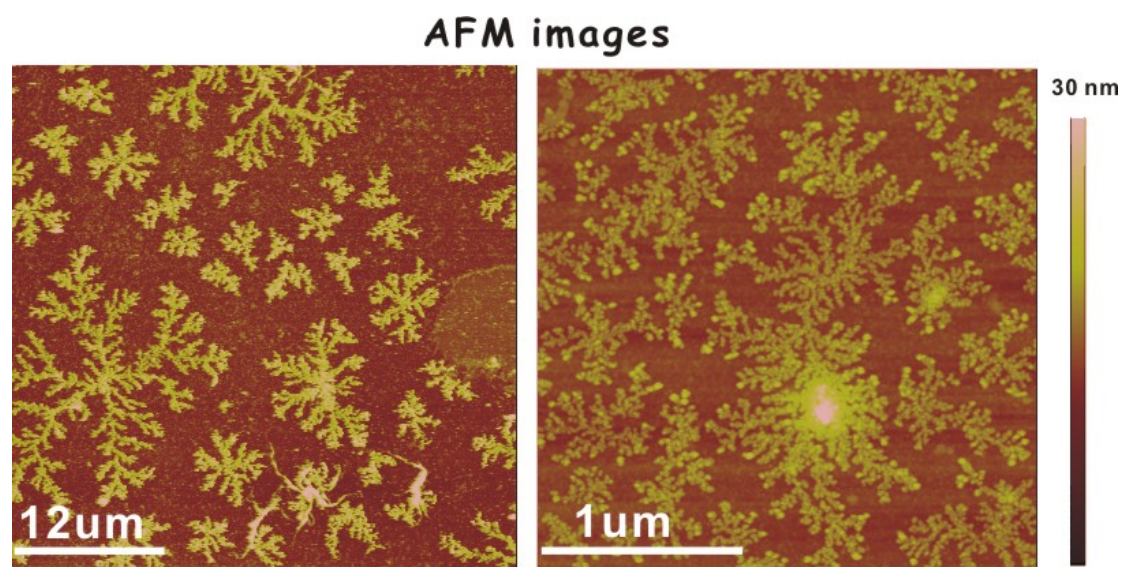


Figure 3.43. Top: Tapping mode height images of 5c (ss-DNA-b-PS with 56000 g/mol PS) on hydrophilic silicon surface in air (**Left:** 40X40 μm^2 ; **Right:** 2.5X2.5 μm^2). The concentration was 3 ng/ μL and Z range is 30nm for both images. **Bottom:** Optical images of 5c on hydrophilic silicon surface in air (**Left:** 985X985 μm^2 ; **Right:** 985X985 μm^2). The concentration was 30 ng/ μL .

Although the drop casted films are not homogeneous, the main feature was still similar in most areas on one sample. By comparing the border area at 5ng/ μL with the center area at 25 ng/ μL , we found quite similar structures. Possibly the structure will be more similar when increasing the concentration to higher than 25 ng/ μL . Figure 3.44 shows similar dendritic structures from different position on two different samples. The first image from left side shows end of dendritic structures in the center area of one 5a sample at 5 ng/ μL . On the same sample, however, denser structures were detected in the border area, which is shown in the middle image. The right image shows similar structures from center area of the same molecule at 25 ng/ μL on silicon surface.

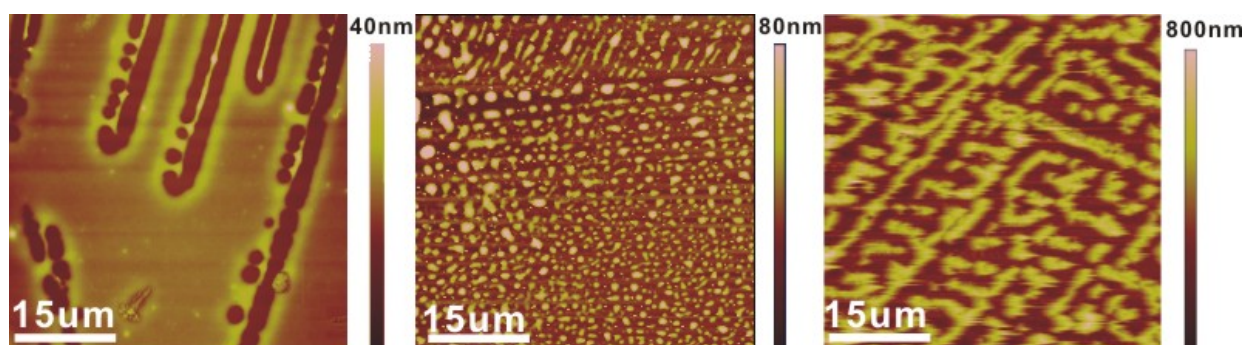


Figure 3.44. Tapping mode height images of 5a (ss-DNA-b-PS with 5500 g/mol PS) on hydrophilic silicon surface in air (40X40 μm^2). **Left:** Center area of one 5a sample prepared at 5 ng/ μL and Z range is 40 nm. **Middle:** Border area of the same sample to left image and Z range is 80 nm. **Right:** Center area of the other 5a sample prepared at 25 ng/ μL and Z range is 800 nm.

We attribute these structures to the formation of cylindrical micelles. The globular micelles aggregated to long fibers upon solvent evaporation which resulted in a deformation of the cylindrical shape. They have a tendency to form dendritic structure, which can be explained with diffusion limited aggregation (DLA) theory.

3.2.3 Diffusion limited aggregation

DLA theory is a typical model (Figure 3.45) for explaining the fractal growth. It was provided by Witten and Sander in 1981^{59 60}. A fractal is a geometric figure in which a single pattern is repeated at a continuously decreasing scale (“self-similarity”). Dimension is a term used to measure the size of a set. Usually, this set will be an image. We are all familiar with objects that are one-dimensional (a line segment), two-dimensional (a square), and three-dimensional (a cube). We can also say that these objects have dimension 1, 2, and 3, respectively. Fractals have dimension, also. But the value of their dimension does not necessarily need to be an integer. Fractal dimension is calculated by $D_f = \ln K / \ln L$ (K is the multiple in shape; L is the multiple in scale). The model for DLA theory is that a particle starts to work randomly from the rim of the lattice. It will adjacent to the seed particle or move to the rim and disappear. Once there is no movable particle in the lattice, new particle will be introduced from the rim again. This process repeats itself. DLA theory has been used to explain the dendritic fractal growth in PEO^{61 62}, in polymer blends as Blends of poly(aryl-ether-ether-ketone) (PEEK) with poly(ether-imide) (PEI)⁶³, in isotactic PS⁶⁴, and also in block copolymers^{65 66}. In these films, crystal structures are thickness dependent in ultrathin films (film thickness < 100 nm). The structures formed from DLA growth consist of dendrites, spherulites, and fibers.



Figure 3.45. Witten-Sander cluster model grown on two dimensional square lattices which consists of 10000 particles.

3.2.4 Structural growth

Sometimes the structural growth was captured by AFM. Figure 3.46 shows an example of 5c with growing dendritic structures on silicon surface. After solvent evaporation, there is no crystal structure on the surface of the chosen area but only seed particles. After 2h, dendritic growing fibers were observed and they were growing with the time. After 4h, the growing in the main area of the dendrons became slower and surface was covered more densely. After 6h, they started to grow only in the end of the branches. After 8h, the ends of the branches were interconnected to each other.

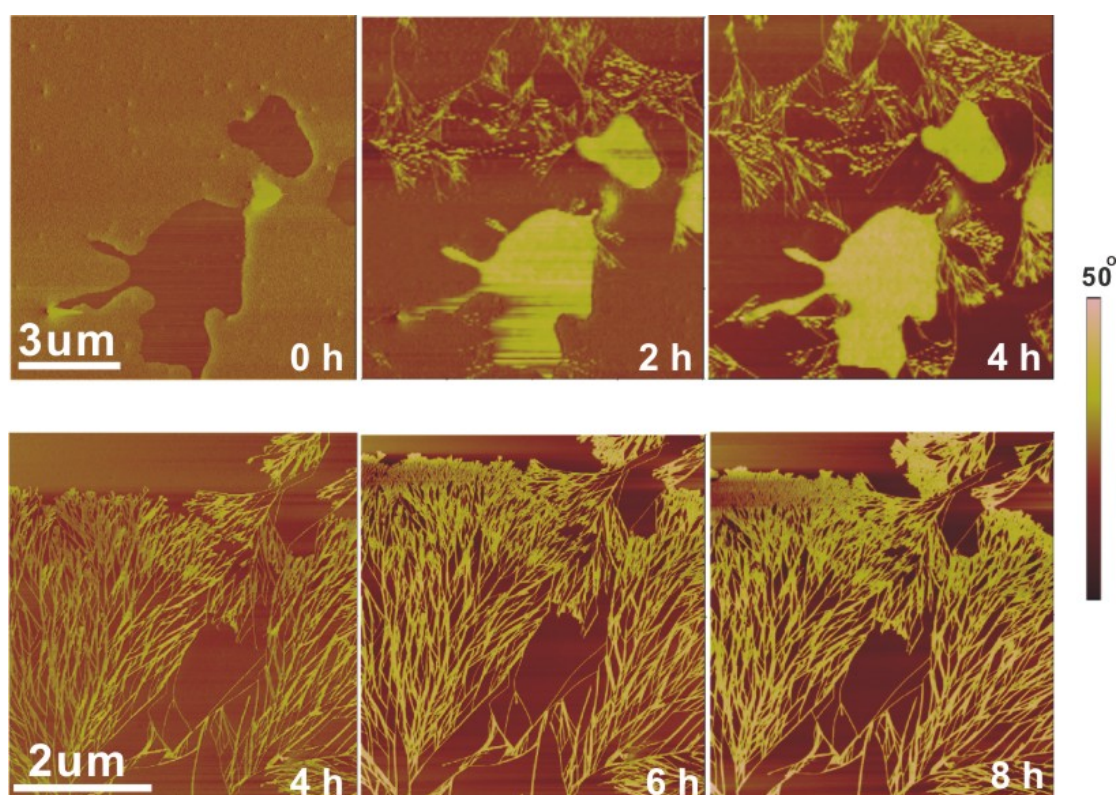


Figure 3.46. AFM phase images of 5c (ss-DNA-b-PS with 56000 g/mol PS) on silicon surface at different time scale within 8 hours. The images were captured at 0h, 2h, 4h, 6h, and 8h, respectively. (**Top:** 10X10 μm^2 **Bottom:** 5X5 μm^2) The concentration was 5 ng/ μL and Z range is 50° for all the images.

3.2.5 Environmental parameters

The experiments done in air with AFM were not always reproducible because the environmental conditions such as humidity, incubation time, and temperature can influence the structures significantly.

Temperature

When sample 5b was heated, the phase contrast started to change at 90°C and the fibers started to be dissolved at 100°C. The T_G for DNA is around 90°C and for PS is around 100°C. Therefore this phase contrast switching may be due to the molten of the DNA in the corona of the cylindrical micelles. Further heating to 100°C resulted in the molten of PS block and the fibers were no more visible (Figure 3.47).

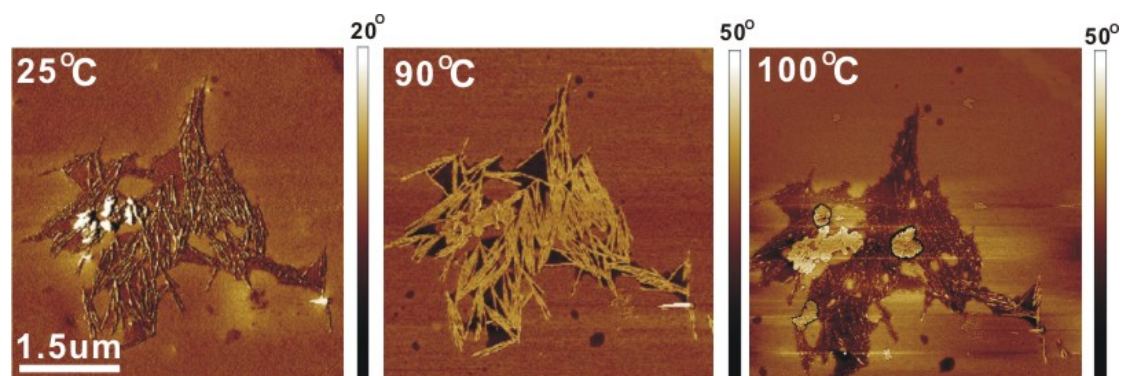


Figure 3.47. Tapping mode phase images of 5b (ss-DNA-b-PS with 10000 g/mol PS) on hydrophilic silicon surface in air ($5 \times 5 \mu\text{m}^2$). The temperature was increased from 25°C to 90°C and 100°C. Sample was prepared at 5 ng/ μL and Z range is 20° for the left image and 50° for the middle and right images.

Humidity

When the sample was exposed to the toluene atmosphere overnight, the structure did not change. However, when the sample was in the atmosphere of pure water, the cylindrical structure changed significantly with 75% humidity (Figure 3.48).

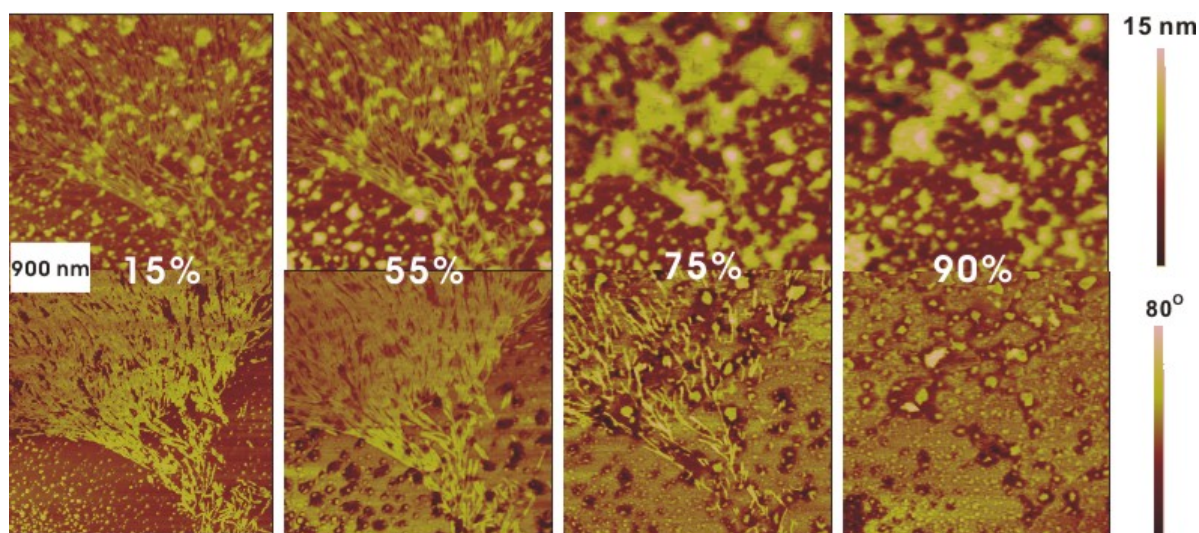


Figure 3.48. AFM height (**top**) and phase (**bottom**) images of 5c (ss-DNA-b-PS with 56000 g/mol PS) on silicon surface at different humidity. The humidity increased from 15% to 55%, 75%, and 90%. All the images have scan size $3 \times 3 \mu\text{m}^2$. The concentration was $5 \text{ ng}/\mu\text{L}$ and Z range is 15nm for height images and 80° for phase images.

Substrate

We used hydrophilic silicon, mica and hydrophobic graphite as substrate to compare the different structures on different substrates. As a result, cylindrical micelles formed on all the three substrates (Figure 3.49). The three images on top show cylindrical micellar structures of 5c in nanometer scale on silicon, mica, and graphite surface, respectively. The images in bottom represent micrometer scaled structures of 5c on silicon, mica, and graphite, respectively.

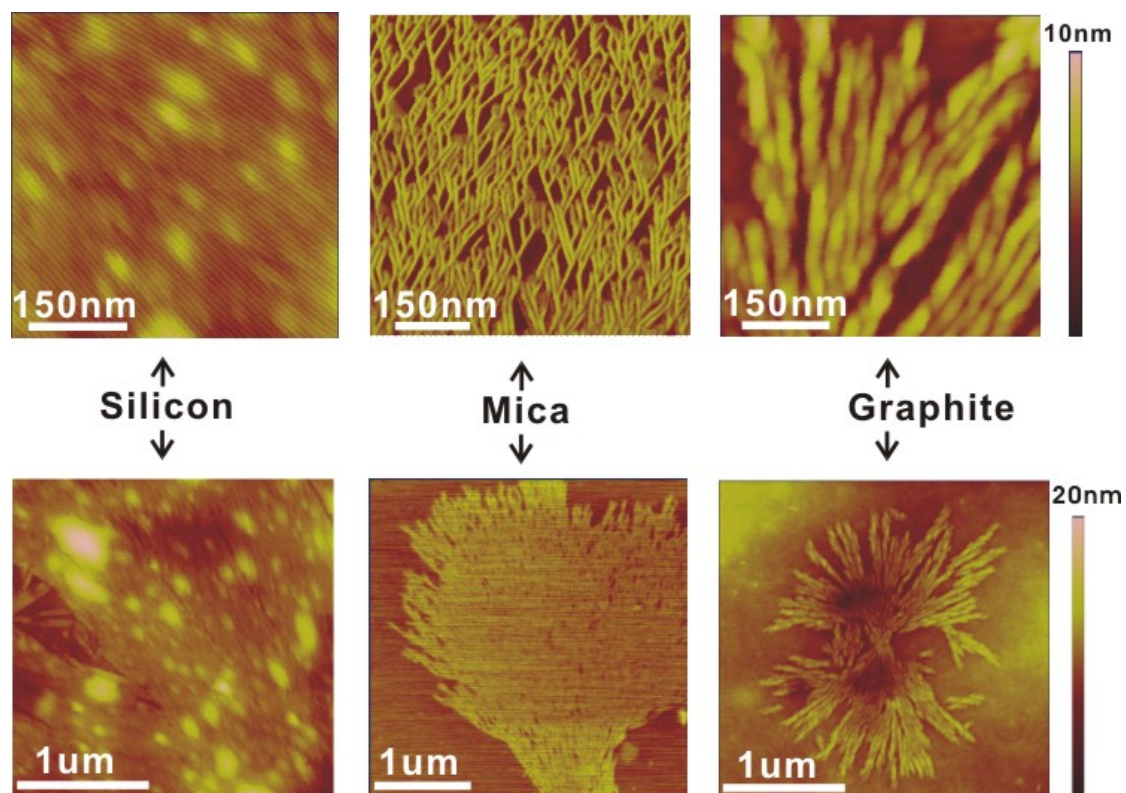


Figure 3.49. Top: Nanometer scaled tapping mode height images of 5c (ss-DNA-b-PS with 56000 g/mol PS) on silicon, mica, and mica in air (**Left:** 500X500 nm². **Middle:** 660X660 nm². **Right:** 550X550 nm²). The concentration was 5 ng/μL and Z range is 10nm for all the images. **Bottom:** Micrometer scaled tapping mode height images of 5c (ss-DNA-b-PS with 56000 g/mol PS) on silicon, mica, and mica in air (**Left:** 2.3X2.3 μm². **Middle:** 3.3X3.3 μm². **Right:** 2.7X2.7 μm²). The concentration was 5 ng/μL and Z range is 20nm for all the images.

3.2.6 Fibers formed with ss-DNA-b-PPO

In stead of globular micelles, fibers have also been observed on ss-DNA-b-PPO films by drop casting at 1 ng/μL on silicon. They formed short or long, singly separated or close packed fibers even in one sample on different positions (Figure 3.50). These fibers are also attributed to the formation of cylindrical micelles from the amphiphilic block copolymer of DNA-b-PPO.

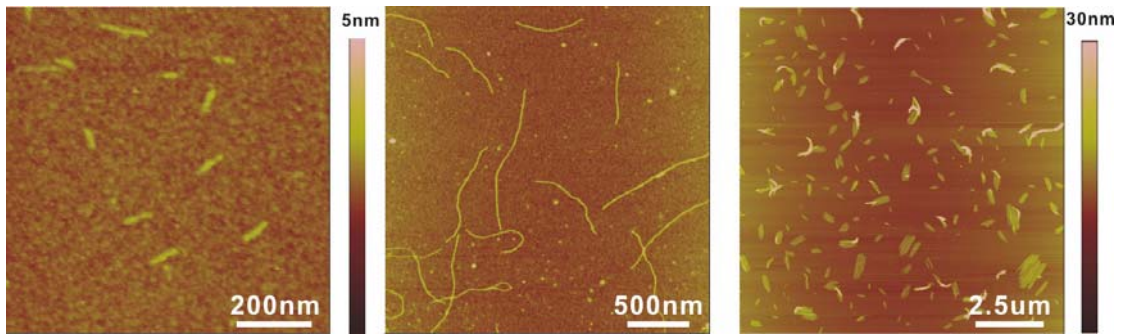


Figure 3.50. Tapping mode height images of ss-DNA-b-PPO on silicon in air (**Left:** 866X866 nm²; Z range 5 nm. **Middle:** 2.63X2.63 μm²; Z range 5 nm. **Right:** 12X12 μm²; Z range 30 nm.). The concentration was 1 ng/μL.

3.3 AFM studies in air on Au-templated films

Other than drop casting, we have also used evaporated gold as template for preparing the films with target of DNA-*b*-PS as well as DNA-*b*-PPO. The adsorption process was detected by SPR layer by layer. The Au-templated film preparation has been introduced in Chapter 1.4. The schematic illustration for the matrix is shown in Figure 3.51. The matrix was prepared on glass by following the sequence of evaporated gold, the SAM of mixed thiol solution, the streptavidin solution, and the biotinylated ss-DNA. If we only add complementary sequenced DNA to the template, however, the hybridization can not be detected by only SPR because SPR is sensitive to refractive index changes and thickness changes. The signal is too weak to be detected by only hybridization. Typically a fluorophore is needed to enhance the signal to combine with SPR, which is called SPR fluorescence spectroscopy (SPFS).

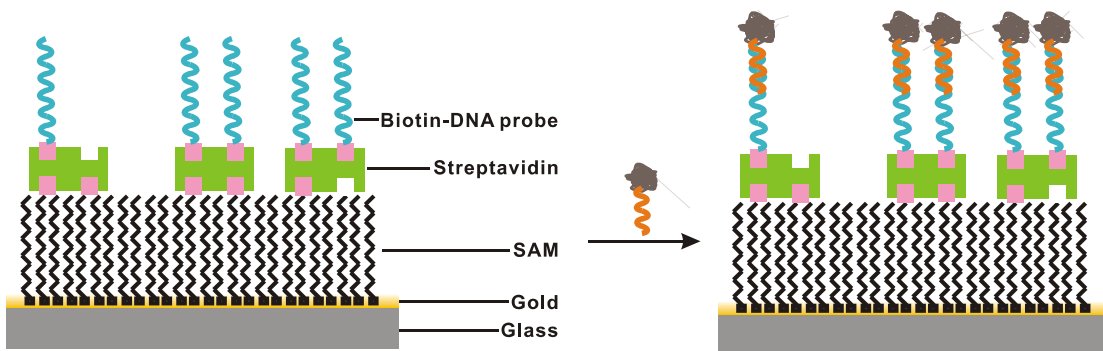


Figure 3.51. Schematics of self-assembled matrix before and after adding target of complementary sequenced DNA-*b*-PS.

In our conditions, the target of DNA-*b*-PS (22mer DNA, 3'-ATTGTCCTAATCGTCTCGCTCC-5'; 50000 g/mol PS) was hybridized with the biotinylated complementary sequenced DNA (5'-(TTT)₅-TAACAGGAT TAGCAGAGCGAGG-3'). The mass increasing by adding the target of DNA-*b*-PS induced the shift from SPR investigations. Figure 3.52 shows the angular scan curves of layer by layer adding of the materials.

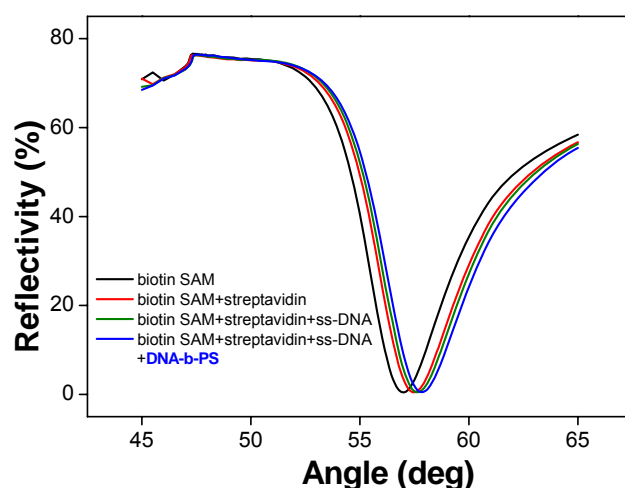


Figure 3.52. The angular SPR curves of the layer by layer adsorption of biotin SAM, streptavidin, ss-DNA, and the DNA-*b*-PS which contains complementary sequences with ss-DNA.

The reference measurement contains 3 layers without target of DNA-*b*-PS. From the AFM height images in Figure 3.53 the reference measurement before adding DNA-*b*-PS and the measurement after adding DNA-*b*-PS show different structures in nanometer scale. The height of the blobs in the right images is around 4.5 nm and the diameter is between 20 and 30 nm. Therefore the structures could be either the single PS molecules or the flattened globular micelles from DNA-*b*-PS.

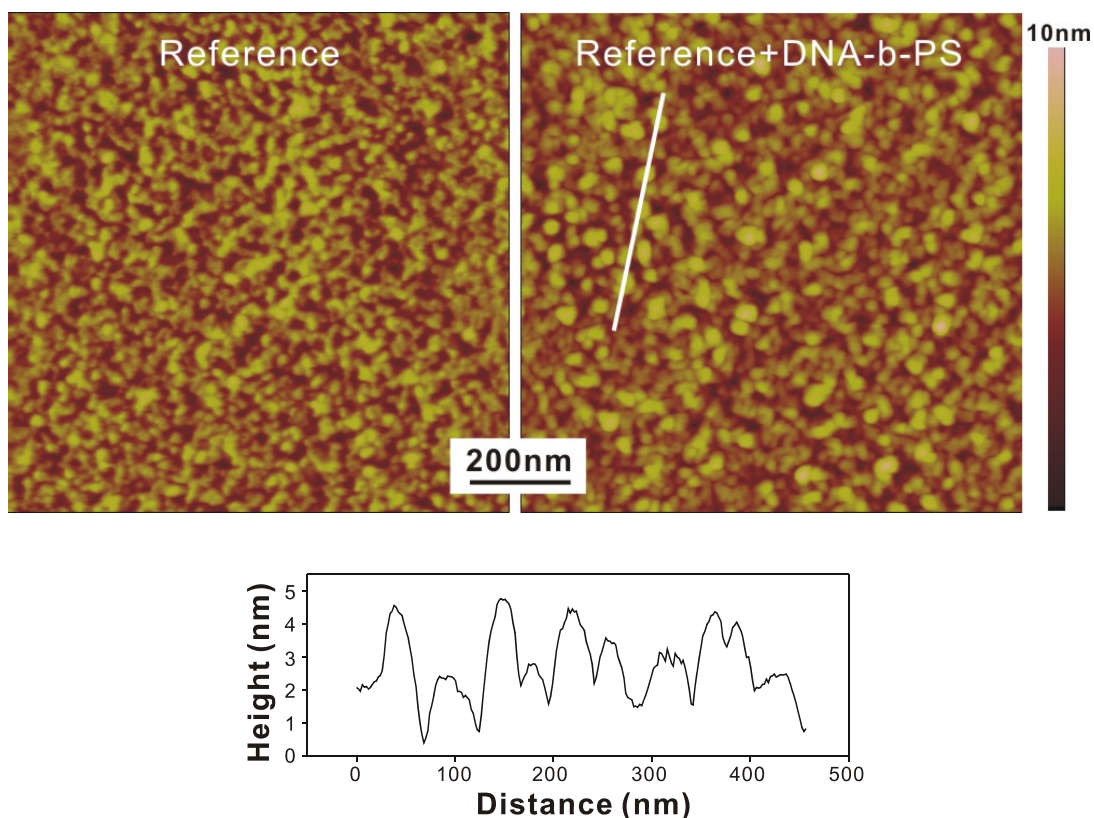


Figure 3.53. AFM height images ($1 \times 1 \mu\text{m}^2$) of Au-templated films before (left) and after (right) adding PS-*b*-DNA in air. Z range is 10 nm for both images. The cross section shows the height versus distance along the white line on the AFM image.

In order to further control the above experiment, mismatched ss-DNA has also been applied when adding the layer of biotinylated DNA with sequences 5'-(TTT)₅TTGTTTCTATACTTTTTCACTA-3'. The SPR curves have no shift by adding the target of same DNA-*b*-PS (22mer DNA, 3'-ATTGTCCTAATCGTCTCGCTCC-5'; 50000 g/mol PS) (Figure 3.54). This proves that the hybridization with complementary sequenced DNA-*b*-PS is necessary for the signal changes in the SPR measurements.

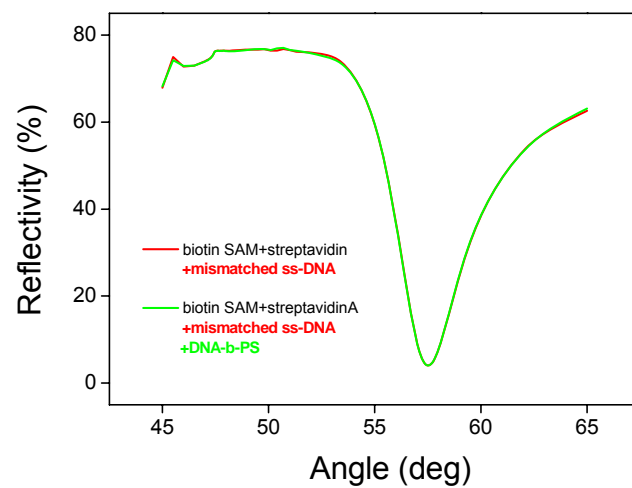


Figure 3.54. The angular SPR curves showing no shift by using mismatched ss-DNA for the target of DNA-b-PS.

SUMMARY AND CONCLUSIONS

AFM studies on surface structures of amphiphilic DNA block copolymers have been done in solution as well as in air. The amphiphilic DNA-*b*-PPOs existed as single molecules or dimers below the CMC on mica substrate in buffer. The length of the dimer is twice as the length of single molecule and the height distributes is around 1 nm. Above CMC the globular micelles with diameter around 11 nm in solution were characterized by DLS and FCS. On mica substrate the micelles flattened due to the interaction between DNA and mica, which resulted in the micelles with height between 4-6 nm by AFM investigations. The AFM tips have not deformed the micelles because of soft tapping. On graphite substrate the micelles were settled on a firstly adsorbed sublayer of DNA-*b*-PPOs, which resulted in a higher height (around 11 nm) observed by AFM imaging. The diameter of the micelles reduced to 2.6 nm by increasing the salt concentration in buffer was investigated by AFM, which was proved by diffusion NMR experiment with a diameter of 3 nm. Chemical modification on the surface of the micelles increased the stiffness so that the adsorption of the micelles to mica did not deform the shape significantly. The height of the micelles was between 10-11 nm by AFM investigations, which is consistent with DLS and FCS results. Amide bonding formation on the surface of the micelles did not change the shape as well as the height of the micelles.

Globular micelles have been transferred into rod like structure through hybridization of DNA-*b*-PPOs with long ss-DNA templates. The length of the rods observed from AFM in buffer solution varies by changing the length of the ss-DNA templates and of the DNA-*b*-PPOs. In addition, the mobility of the PPOs was able to be adjusted by modifying the base sequences. When the PPOs in one molecule are adjusted to be oriented towards one direction, pairs of rods were formed through hydrophobic interaction between polymers on mica substrate in buffer solution by AFM experiments. The rods were not able to form pairs when the spatial hindrance among the PPOs was induced.

AFM investigations in air on DNA-*b*-PSs provided globular micelles upon annealing at 100°C for 12 h. However, the micelles formed from DNA-*b*-PPOs in air without annealing because of the low T_g at -70°C. Dendritic structures were observed on drop casted DNA-*b*-PS films. We attribute the formation of the dendritic structures to the formation of cylindrical micelles with DLA theory. Such structures were not stable and can be affected by concentration, temperature, humidity, incubation time, etc. AFM study on drop casted films in air showed less homogeneity and worse reproducibility than those from the in-situ AFM studies. Hence, gold-templated matrix has been applied as substrate for DNA-*b*-PS to overcome the drawback from drop casting. In fact, the gold-templated film with target of DNA-*b*-PS showed reproducible and stable result by AFM analysis as well as by SPR experiments.

The transition of the molecular structures from single molecules to globular micelles, and further to rod like structures has been detected by AFM as well as FCS studies. Single molecules recognition such as dimers observation helps us better understanding the hydrophobic interaction of the polymers in the DNA block copolymers. Concentration plays an important role in the transition between single molecules and micelles. It is sensitive not only around the value of CMC, but also on the density of the micelles above CMC. The micelles formed from amphiphilic DNA block copolymers can be applied in drug delivery system^{67,68}. These micelles may also be candidates for carrying out chemical reactions in living cells. The needed size of the micelles can be controlled by changing e.g. salt concentrations in buffer. The micelles templated organic reaction was detected by fluorescence spectroscopy allowing easy optimization of reaction conditions for new templated architectures. The shape of globular micelles has been changed into rods upon molecular recognition. Such rods, together with the fibers formed from drop casted films in air, may have the application in nanowire fabrications⁶⁹. For example, they may be metallized on surface by attaching with biomolecules or nanoparticles in order to serve as interconnects in self-assembled arrays⁷⁰⁻⁷². In the near future, we are going to built higher ordered 2- to 3- Dimensional arrays and the longer fibers by modifying base sequence

in the long template and in the block copolymers. The reversed transition from rod like structures to the globular micelles would be possible as well. We are currently working on the reversible experiments by AFM and FCS. SPR measurements on the gold-templated matrix opened a new field on investigating the surface structures of the block copolymers. To follow the layer by layer deposition sequences, in-situ AFM investigations will be done soon to compare directly the surface morphologies after adding each layer.

BIBLIOGRAPHY

- (1) Watson, J. D.; Crick, F. H. C. *Nature* **1953**, *171*, 737.
- (2) Seeman, N. C. *Trends in Biochemical Sciences* **2005**, *30*, 119.
- (3) Rothermund, P. W. K. *Nature* **2006**, *440*, 297.
- (4) Luo, D. *Materials today* **2003**, 38.
- (5) Seeman, N. c. *Nature* **2003**, *421*, 427.
- (6) Fu, T.-J.; Seeman, N. C. *Biochemistry* **1993**, *32*, 3211.
- (7) Li, X. j.; Yang, X.; Qi, J.; Seeman, N. C. *J. Am. Chem. Soc.* **1996**, *118*, 6131.
- (8) Winfree, E.; Liu, F.; Wenzler, L. A.; Seeman, N. C. *Nature* **1998**, *394*, 539.
- (9) Mirkin, C. A.; Letsinger, R. L.; Music, R. C.; Storhoff, J. J. *Nature* **1996**, *382*, 607.
- (10) Alivisatos, A. P.; Johnsson, K. P.; Peng, X.; Wilson, T. E.; Loweth, C. J.; Jr, M. P. B.; Schultz, P. G. *Nature* **1996**, *382*, 609.
- (11) Storhoff, J. J.; Mirkin, C. A. *Chem. Rev.* **1999**, *99*, 1849.
- (12) Keren, K.; Berman, R. S.; Buchstab, E.; Sivan, U.; Braun, E. *Science* **2003**, *302*, 1380.
- (13) Taton, T. A.; Mirkin, C. A.; Letsinger, R. L. *Science* **2000**, *289*, 1757.
- (14) Braun, E.; Eichen, Y.; Sivan, U.; Ben-Yoseph, G. *Nature* **1998**, *391*, 775.
- (15) Mao, C.; Sun, W.; Shen, Z.; Seeman, N. C. *Nature* **1999**, *397*, 144.
- (16) Liu, H.; chen, Y.; He, Y.; Ribbe, A. E.; Mao, C. *Angew. Chem. Int. Ed.* **2006**, *45*, 1.
- (17) Xu, J.; Craig, S. L. *J. Am. Chem. Soc.* **2005**, *127*, 13227.
- (18) Qin, W. J.; Yung, L. Y. L. *Langmuir* **2005**, *21*, 11330.
- (19) Niemeyer, C. M.; Buerger, W.; Peplies, J. *Angew. Chem. Int. Ed. Engl.* **1998**, *37*, 2265.
- (20) Taton, T. A.; Mirkin, C. A.; Letsinger, R. L. *Science* **2000**, *289*, 1757.
- (21) Taton, T. A.; Mucic, R. C.; Mirkin, C. A.; Letsinger, R. L. *J. Am. Chem. Soc.* **2000**, *122*, 6305.

- (22) Watson, K. J.; Park, S.-J.; Im, J.-H.; Nguyen, S. T.; Mirkin, C. A. *J. Am. Chem. Soc.* **2001**, *123*, 5592.
- (23) Korri-Youssoufi, H.; Garnier, F.; Srivastava, P.; Godillot, P.; Yassar, A. *J. Am. Chem. Soc.* **1997**, *119*, 7388.
- (24) Jeong, J. H.; Park, T. G. *Bioconjugate Chem.* **2001**, *12*, 917.
- (25) Li, z.; Zhang, Y.; Fullhart, P.; Mirkin, C. A. *Nano Letters* **2004**, *4*, 1055.
- (26) Alemdaroglu, F. E.; Ding, K.; Berger, R.; Herrmann, A. *Angew. Chem. Int. Ed.* **2006**, *45*, 4206.
- (27) Wittmann, C. *Immobilisation of DNA on chips 1*; Springer-Verlag Berlin Heidelberg: Berlin, 2005.
- (28) Hansma, H. G. *Annu. Rev. Phys. Chem.* **2001**, *52*, 71.
- (29) Hansma, H. G.; Revenko, I.; Kim, K.; Laney, D. E. *Nucleic Acids Research* **1996**, *24*, 713.
- (30) Reishus, D.; Shaw, B.; Brun, Y.; Chelyapov, N.; Adleman, L. *J. Am. Chem. Soc.* **2005**, *127*, 17590.
- (31) Magonov, S. N. *encyclopedia of analytical chemistry* **2000**, 7432.
- (32) Roiter, Y.; Minko, S. *J. Am. Chem. Soc.* **2005**, *127*, 15688.
- (33) Binnig, G.; Quate, C. F.; Gerber, C. *Phys. Rev. Lett.* **1986**, *56*, 930-933.
- (34) Albrecht, T. R.; Dovek, M. M.; Lang, C. A.; Gruetter, P.; Quate, C. F.; Kuan, S. N. J.; Frank, C. W.; Pease, R. F. W. *J. Appl. Phys.* **1988**, *64*, 1178.
- (35) Akamine, S.; Barrett, R. C.; Quate, C. F. *Appl. Phys. Lett.* **1990**, *57*, 316.
- (36) Albrecht, T. R.; Akamine, S.; Carver, T. E.; Quate, C. F. *J. Vac. Sci. Technol. A* **1990**, *8*, 3386.
- (37) Buser, R. A.; Brugger, J.; Rooij, N. F. d. *Microelectronic Engineering* **1991**, *15*, 407.
- (38) Butt, H.-J.; Siedle, P.; Seifert, K.; Fendler, K.; Seeger, T.; Bamberg, E.; Weisenhorn, A. L.; Goldie, K.; Engel, A. *Journal of Microscopy* **1993**, *169*, 75.
- (39) Cleveland, J. P.; Anczykowski, B.; Schmid, A. E.; Elings, V. B. *Appl. Phys. Lett.* **1998**, *72*, 2613.
- (40) Whangbo, M. H.; Magonov, S. N.; Elings, V. *Surface Science* **1997**, *375*, 385.

- (41) Magonov, S. N.; Elings, V.; Whangbo, M. H. *Surface Science Letters* **1997**, *375*, L385-L391.
- (42) Hansma, H. G.; Vesenka, J.; Siegerist, C.; Kelderman, G.; Morrett, H.; Sinsheimer, R. L.; Elings, V.; Bustamante, C.; Hansma, P. K. *Science* **1992**, *256*, 1180.
- (43) Markovic, N. M.; Tidewell, I. M.; ROS, P. N. *Langmuir* **1994**, *10*, 5.
- (44) Colton, R. J.; Baselt, D. R.; Dufkne, Y. F.; Green, J.-B. D.; Lee, G. U. *Curr.Opin.Chem.Biol* **1997**, *1*, 370.
- (45) Rivetti, C.; Guthold, M.; Bustamante, C. *J. Mol. Biol.* **1996**, *264*, 919.
- (46) Schmitz, K. S. *An Introduction to Dynamic Light Scattering by Macromolecules*; Academic Press: New York, 1990.
- (47) Schurr, J. M. *Ann. Rev. Phys. Chem.* **1986**, *37*, 271.
- (48) Cao, a. *ANALYTICAL LETTERS* **2003**, *36*, 3185.
- (49) Krichevsky, O.; Bonnet, G. *Rep. Prog. Phys.* **2002**, *65*, 251.
- (50) Selb, J.; Gallot, Y. *Makromol. Chem.* **1980**, *181*, 809.
- (51) Foerster, S.; Abetz, V.; Mueller, A. H. E. *Adv. Polym. Sci.* **2004**, *166*, 173.
- (52) Sinder, R. R.; Potaman, V. N.; Oussatcheva, e. A.; Pearson, C. E.; Lyubchenko, Y. L.; Shlyakhtenko, L. S. **2002**.
- (53) Wilhelm, M.; Zhao, c.-L.; Wang, Y.; Xu, R.; Winnik, M. A. *Macromolecules* **1991**, *24*, 1033.
- (54) Regev, O.; Zana, R. *J. Colloid Interface Sci.* **1999**, *210*, 8.
- (55) Grant, L. M.; Tiberg, F.; Ducker, W. A. *J. Phys. Chem. B* **1998**, *102*, 4288.
- (56) Huang, Y.-X. *J. Chem. Phys.* **1997**, *107*, 9141.
- (57) Dufresne, M.-H.; Leroux, J.-C. *Pharmaceutical Research* **2004**, *21*, 160.
- (58) Lee, A. S.; Buetuen, V.; Vamvakaki, M.; Armes, S. P.; Pople, J. A.; Gast, A. P. *Macromol.* **2002**, *35*, 8540.
- (59) Witten, T. A.; Sander, L. M. *Phys. Rev. Lett.* **1981**, *47*, 1400.
- (60) Witten, T. A.; Sander, L. M. *Phys. Rev. B* **1983**, *27*, 5686.
- (61) Schoenherr, H.; Frank, C. W. *Macromol.* **2003**, *36*, 1188.
- (62) Reiter, G.; Sommer, J.-U. *J. Chem. Phys* **2000**, *112*, 4376.
- (63) Ivanov, D. A.; Nysten, B.; Jonas, A. M. *Polymer* **1999**, *40*, 5899.

- (64) Taguchi, K.; Miyaji, H.; Izumi, K.; Hoshino, A.; Miyamoto, Y.; Kokawa, R. *J. Macro, Sci. B* **2002**, *41*, 1033.
- (65) Li, L.; Chan, C.-M.; Li, J.-X.; Ng, K.-M.; Yeung, K.-L.; Weng, L.-T. *Macromol.* **1999**, *32*, 8240.
- (66) Leclere, P.; Surin, M.; Jonkheijm, P.; Henze, O.; Schenning, A. P. H. J.; Biscarini, F.; Grimsdale, A. C.; Feast, W. J.; Meijer, E. W.; Muellen, K.; bredas, J. L.; Lazzaroni, R. *European Polymer Journal* **2004**, *40*.
- (67) Adams, M. L.; Lavasanifar, A.; Kwon, G. S. *Journal of Pharmaceutical Sciences* **2003**, *92*, 1343.
- (68) Jones, M.-c.; Leroux, J.-c. *European Journal of Pharmaceutics and Biopharmaceutics* **1999**, *48*, 101.
- (69) Gu, Q.; Cheng, C.; Gonela, R.; Suryanarayanan, S.; Anabathula, S.; Dai, K.; Haynie, D. T. *Nanotechnology* **2006**, *17*, R14.
- (70) Yan, H.; Park, S. H.; Finkelstein, G.; Reif, J. H.; LaBean, T. H. *Science* **2003**, *301*, 1882.
- (71) Liu, Y.; Lin, C.; Li, H.; Yan, H. *Angew. Chem. Int. Ed.* **2005**, *44*, 4333.
- (72) Sharma, J.; Chhabra, R.; Liu, Y.; Ke, Y.; Yan, H. *Angew. Chem. Int. Ed.* **2006**, *45*, 730.

LIST OF PULICATIONS

- K. Ding, D. Grebel-Koehler, R. Berger, K. Müllen, and H.-J. Butt, *Structure of self-assembled n-dodecyl substituted azobezene polyphenylene dendrimers on graphite*, *J. Mater. Chem.*, **2005**, *15*, 3431.
- F. E. Alemdaroglu, K. Ding, R. Berger, and A. Herrmann, *DNA-templated Synthesis in Three Dimensions: Introducing a Micellar Scaffold for Organic Reactions*, *Angew. Chem. Int. Ed.*, **2006**, *45*, 4206.
- K. Ding, F. E. Alemadaroglu, M. Börsch, R. Berger, and A. Herrmann, *Engineering the Structural Properties of DNA Block Copolymer Micelles by Molecular Recognition*, *Angew. Chem. Int. Ed.*, **2006**, submitted.

ABBREVIATIONS

AFM	atomic force microscopy
DNA	deoxyribonucleic acid
PPO	polypropylene oxide
PS	polystyrene
CMC	critical micelle concentration
DLS	dynamic light scattering
FCS	fluorescence correlation spectroscopy
HOPG	highly oriented pyrolytic graphite
ds	double stranded
ss	single stranded
PCR	polymerase chain reaction
PEO	polyethylene oxide
T_g	glass transition temperature
STM	scanning tunneling microscopy
SPM	scanning probe microscopy
SEM	scanning electron microscopy
LS	light scattering
SLS	static light scattering
APD	avalanche photo diode
M_w	molecular weight
SAM	self-assembled monolayer
biotinylated thiol	biotinaminocapronacid-amidodioctyl-mercaptopropionamide
DLA	diffusion limited aggregation
PEEK	poly(aryl-ether-ether-ketone)
PEI	poly(ether-imide)
SPR	surface plasmon resonance spectroscopy
SPFS	SPR fluorescence spectroscopy

